Terahertz Communications: Physical Layer Enablers and Analysis

Konstantinos Dovelos

DOCTORAL THESIS UPF / Year 2021

Thesis Supervisor: Boris Bellalta
Department of Information and Communication Technologies

Luck favors the prepared mind.

– Richard Hamming

Acknowledgments

Pursuing a PhD abroad has been a life-changing experience for me, and it would not have been possible without the support and guidance of several people.

First and foremost, I would like to express my deepest gratitude to my advisor, Prof. Boris Bellalta, for giving me the opportunity to join his research group, as well as for his unwavering support and encouragement throughout the PhD.

I would like to sincerely thank Prof. Leonidas Georgiadis, from Aristotle University of Thessaloniki, for the numerous invaluable discussions on stochastic network optimization and Lyapunov techniques. Working with him was a very stimulating experience, which fuelled my passion for mathematics. I was particularly impressed by his capacity to find elegant solutions to complex optimization problems. I dare to say that he is one of the brightest minds I have ever encountered.

I am especially grateful to my mentor, Prof. Michalis Matthaiou at Queen's University Belfast (QUB), who initiated me into the world of massive MIMO and terahertz communications. My two-year collaboration with him was extremely fruitful. More importantly, it shaped the course of my doctoral studies in various ways, and provided me the means to develop as a researcher. I admire his professional mindset and commitment to high quality research. I believe we share the same attitude toward science and excellence. I would also like to give special thanks to my co-authors from QUB, Dr. Hien Quoc Ngo and Dr. Stylianos Assimonis, for their valuable assistance. They were always willing to answer my technical questions and contribute to the papers with their expertise. They are both great researchers, and I have learnt so many things from them.

Finally, I owe the warmest thank to my family and friends for their constant love and unceasing encouragement throughout my life. This thesis is dedicated to my dear parents, Giannis and Georgia.

Thessaloniki, July 2021

Abstract

Undoubtedly, spectrum scarcity constitutes the main bottleneck of current wireless networks. It is therefore imperative to move beyond the sub-6 GHz band in order to overcome this limitation. Toward this direction, terahertz (THz) communication is deemed a promising solution for future wireless systems owing to the abundant spectrum resources at these frequencies. Despite the prospect of terabit-per-second wireless links, THz signals suffer from severe propagation losses, which can undermine the communication range and performance of THz systems. In this dissertation, we tackle this challenge by putting forward two key physical layer technologies, namely massive multiple-input multiple-output (MIMO) and intelligent reflecting surfaces (IRSs).

More particularly, this dissertation consists of two parts. In the first part, we thoroughly study the spatial-wideband effect in THz massive MIMO. We commence by demonstrating that conventional narrowband beamforming/combining leads to substantial performance degradation for large antenna arrays and high transmission bandwidths. With this in mind, we propose a wideband array architecture based on true-time-delay and virtual subarrays. For the channel estimation problem, we introduce a wideband dictionary along with a novel variant of the orthogonal matching pursuit algorithm. Numerical simulations are provided showcasing that the proposed design enables: i) nearly squint-free beamforming/combining with a small number of true-time-delay elements; and ii) accurate channel acquisition with reduced pilot overhead even in the low signal-to-noise-ratio regime.

In the second part, we focus on the fundamentals of IRSs at THz frequencies. Specifically, we show that an IRS has the potential to improve the energy efficiency of THz MIMO, when it is placed close to one of the link ends. As a result, electrically large IRSs are expected to operate in the radiating near-field zone, where the spherical wavefront of the emitted electromagnetic (EM) waves cannot be neglected. To this end, we introduce a spherical wave channel model by leveraging EM theory, which includes far-field as special case. Furthermore, we discuss the importance of using EM principles to characterize the path loss of IRS-aided links, as simplistic models may wrongly estimate the link budget and actual system performance. Our analysis reveals that: i) conventional far-field beamforming is highly suboptimal in terms of power gain, and hence beamfocusing is the optimal mode of operation for THz IRSs; and ii) frequency-dependent beamfocusing is required in wideband THz transmissions, as beam squint can substantially reduce the achievable data rate.

List of Main Papers

The following papers constitute the backbone of this dissertation. Note that throughout this document, we refer to them as papers I-IV.

I. **Channel Estimation and Hybrid Combining for Wideband Terahertz Massive MIMO Systems**

   Authored by Konstantinos Dovelos, Michail Matthaiou, Hien Quoc Ngo, and Boris Bellalta.

   Published in the IEEE Journal on Selected Areas in Communications (JSAC), 2021.

II. **Intelligent Reflecting Surfaces at Terahertz Bands: Channel Modeling and Analysis**

   Authored by Konstantinos Dovelos, Stylianos Assimonis, Hien Quoc Ngo, Boris Bellalta, and Michail Matthaiou.

   Published in the proceedings of the IEEE International Conference on Communications (ICC), 2021.

III. **Electromagnetic Modeling of Holographic Intelligent Reflecting Surfaces at Terahertz Bands (Invited)**

   Authored by Konstantinos Dovelos, Stylianos Assimonis, Hien Quoc Ngo, Boris Bellalta, and Michail Matthaiou.

   Submitted to the 55^{th} Annual Asilomar Conference on Signals, Systems, and Computers (ACSSC), 2021.

IV. **Intelligent Reflecting Surface-Aided Wideband THz Communications: Modeling and Analysis (Invited)**

   Authored by Konstantinos Dovelos, Stylianos Assimonis, Hien Quoc Ngo, Boris Bellalta, and Michail Matthaiou.

   To appear in the 25^{th} International ITG Workshop on Smart Antennas (WSA), 2021.

List of Other Papers

During my PhD, I worked on a few additional projects that fall outside the scope of this dissertation. Nevertheless, the corresponding papers are listed below as they represent an important part of my early research.

1. **Massive MIMO with Multi-Antenna Users under Jointly Correlated Ricean Fading**

   Authored by Konstantinos Dovelos, Michail Matthaiou, Hien Quoc Ngo, and Boris Bellalta.

   Published in the proceedings of the IEEE International Conference on Communications (ICC), 2020.

2. **A Scheduling Policy for Downlink OFDMA in IEEE 802.11ax with Throughput Constraints**

   Authored by Konstantinos Dovelos and Boris Bellalta.

   Preprint available on the arXiv, 2019.

3. **Breaking the Interference Barrier in Dense Wireless Networks with Interference Alignment**

   Authored by Konstantinos Dovelos and Boris Bellalta.

   Published in the proceedings of the IEEE International Conference on Communications (ICC), 2018.

Mathematical Notation

Notation	Description
$\mathbb{C}$	Set of complex numbers
a	Scalar
$\mathbf{a}$	Vector
$\mathbf{A}$	Matrix (or vector field)
$\mathcal{A}$	Set
$\mathbf{A}^{\dagger}$	Pseudoinverse of $\mathbf{A}$
$\mathbf{A}^{T}$	Transpose of $\mathbf{A}$
$\mathbf{A}^{H}$	Conjugate transpose of $\mathbf{A}$
$\|\mathbf{a}\|$	l_2-norm of $\mathbf{a}$
$\|\mathbf{a}\|_1$	l_1-norm of $\mathbf{a}$
$\mathcal{F}\{\cdot\}$	Continuous-time Fourier transform
$\mathbf{a} \sim \mathcal{CN}(\boldsymbol{\mu}, \boldsymbol{\Sigma})$	Complex Gaussian vector with mean $\boldsymbol{\mu}$ and covariance matrix $\boldsymbol{\Sigma}$
$\mathrm{sinc}(x) = \frac{\sin(x)}{x}$	Sinc function
$D_N(x) = \frac{\sin(Nx/2)}{N\sin(x/2)}$	Dirichlet sinc function
$\mathrm{erf}(x) = \frac{2}{\sqrt{\pi}} \int_0^x e^{-t^2} dt$	Error function

Contents

1 Introduction

1.1 Motivation

Spectrum scarcity is the main bottleneck of current cellular networks operating in the sub-6 GHz band, which limits the peak data rate to a few hundred Megabits per second [1]. To satisfy the ever-increasing demand for massive and broadband wireless connectivity, 5G communication systems will utilize also the millimeter wave (mmWave) band, potentially boosting the peak data rate to 10 Gigabits per second [2]. To overcome future capacity limitations, the Wireless Industry turns to the terahertz (THz) band (0.1-10 THz), which is widely deemed the next frontier for beyond-5G networks due to the enormous bandwidths[1] available at these frequencies [3, 4]. However, extremely high carrier frequencies entail severe propagation losses owing to the short wavelength of the transmitted signals. As a result, advanced physical layer technologies are key to mitigating these losses and extending the communication range of THz systems [6, 7].

One such technology is massive multiple-input multiple-output (MIMO), where a very large number of antennas is deployed at the base station (BS) [8, 9]. In this way, the severe path attenuation at THz frequencies can be effectively mitigated by sharp beamforming [10]. Thus, massive MIMO will constitute an integral part of future THz systems. Nevertheless, deploying a massive number of BS antennas poses many practical challenges, such as efficient hardware implementation with low power consumption. For this reason, THz massive MIMO will be realized by hybrid analog-digital antenna arrays, where the number of radio-frequency (RF) chains is much smaller than the number of BS antennas [11]. Because of the hybrid array structure, beamforming and channel estimation become nontrivial tasks, especially for ultra-wideband transmissions where spatial-frequency wideband effects start to kick in [12]. In short, THz massive MIMO calls for carefully tailored solutions that account for the peculiar characteristics of THz propagation.

Even though hybrid antenna arrays facilitate the energy efficient implementation of massive MIMO, packing an unprecedented number of antennas into an array might yield an untolerable power consumption. This problem is particularly acute in THz MIMO systems as the power expenditure of THz circuits is much larger than their sub-6 GHz counterparts [13]. To alleviate this problem, the novel concept of intelligent reflecting surfaces (IRSs) can be exploited to build transceivers with a relatively small number of antennas, which work along with an IRS to achieve high

[1] In fact, they can exceed those in the mmWave band by an order of magnitude [5].

spectral efficiency with reduced power consumption [14]. Specifically, an IRS[2] is a metasurface consisting of nearly passive reconfigurable elements, which can customize the behavior of the impinging electromagnetic (EM) waves. As such, IRSs are expected to revolutionize future wireless networks by creating smart propagation environments [15]. The prospects of IRSs have sparked great research interest in the topic of EM metasurfaces and wave manipulation. However, the majority of related studies (see [16–18] and references therein) focus on the sub-6 GHz band, where channel modeling substantially differs from that at higher frequencies. For example, pure stochastic channel models, e.g., Rayleigh fading, are not applicable to THz bands because of the extremely limited multipath propagation [19]. More importantly, the popular far-field assumption might be invalid for THz IRSs, which are expected to work very close to the transmitter (Tx) or receiver (Rx) in order to mitigate the path loss of the Tx-IRS-Rx link with a practical number of reflecting elements; hence, near-field phenomena should be taken into consideration. In conclusion, there are still many critical questions about IRS-aided THz communications.

1.2 Overview of Contributions

In light of the prospect of THz communications for future wireless networks, in this thesis, we study the channel modeling, design, and performance of massive MIMO and IRSs at THz frequencies. Specifically, the main contributions of this thesis are summarized as follows:

Massive MIMO

1. We delve into the spatial-wideband effect, and argue that it plays a key role in wideband THz massive MIMO. As such, we introduce a spatially wideband channel model assuming a uniform planar array (UPA) at the BS.

2. Building on the derived channel model, we study the array gain under the practical constraint of a hybrid array architecture at the BS side. In particular, we calculate the normalized array gain for frequency-flat analog combining in closed-form. Based on that, we show that conventional analog combining leads to severe beam squint and, in turn, to a significant performance degradation.

3. To address the beam squint problem, which is inherent in typical narrowband arrays, we propose a novel wideband array architecture based on true-time-delay (TTD) and virtual subarrays. Our design relies mainly on plane phase shifters, which are grouped into virtual subarrays. Then, a small number of TTD elements is deployed between the virtual subarrays with the aim of implementing frequency-dependent combining. We show that this hybrid scheme can eliminate beam squint and perform close to its fully digital counterpart, yet with much lower hardware complexity.

[2]In the literature, IRSs are also known as reconfigurable intelligent surfaces (RISs). In this thesis, we adopt the former term because we focus on metasurfaces that alter only the phase of an incident wave to reflect/focus it toward a desired direction/point.

4. We study channel estimation, which is challenging owing to the hybrid array structure at the BS. To this end, we avail of the angular sparsity of THz channels, and formulate the channel estimation problem as a compressed sensing (CS) problem. Contrary to prior works, we then introduce a wideband dictionary for UPAs that accounts for the spatial-wideband effect. This enable us to apply a novel variant of the orthogonal matching pursuit (OMP) algorithm, which exploits the information of multiple subcarriers to increase the reliability of the channel estimate. Numerical results are provided showcasing the effectiveness of our approach compared to narrowband OMP-like estimators.

Intelligent Reflecting Surfaces

1. For the first time, we delve into the modeling aspects of IRSs at THz frequencies. Unlike their sub-6 GHz and mmWave counterparts, THz IRSs are expected to have a massive number of reflecting elements with a small footprint, and more importantly operate close to the Tx/Rx. Therefore, near-field propagation is of the utmost importance. With this in mind, we propose a spherical wave channel model for discrete IRSs.

2. Capitalizing on the derived channel model, we analyze the power gain under near-field beamfocusing and far-field beamforming. In particular, we demonstrate that the latter one is highly suboptimal in the Fresnel zone, and hence can greatly reduce the power gain. More importantly, we provide a closed-form expression for that reduction. Using the closed-form formula, we show that beamfocusing is the optimal mode of operation for THz IRSs

3. We study the energy efficiency (EE) of IRS-aided MIMO. More particularly, we prove that a nearly-passive IRS can offer huge EE gains compared to a pure MIMO system.

4. We investigate the IRS placement problem, and prove that a THz IRS should be deployed close to one of the link ends, i.e., either the Tx or Rx, in order to mitigate the cascaded path loss with a practical number of reflecting elements.

5. We leverage physical optics from EM theory to determine the near-field response of holographic IRSs; note that a holographic IRS is the ultimate form of IRSs as it incorporates an unprecedented number of elements to realize a nearly continuous reflecting surface. Our analysis reveals the beamfocusing capabilities of electrically large IRSs, and emphasizes the importance of physics-aware channel models.

6. We study IRS-aided wideband THz communications. Unlike prior works, our analysis accounts for the spherical wavefront of the radiated waves and the spatial-wideband effect. We further show that conventional, i.e., frequency-flat, beamfocusing is highly ineffective for very large signal bandwidths. With this in mind, we argue that a broadband IRS design is needed, and identify TTD-based architectures as a promising avenue for future research.

1.3 Document Structure

This thesis constitutes a compendium of four papers, which is the result of intensive research on massive MIMO and IRSs for THz communications. These papers are appended to the end of this document. Furthermore, we provide some background on the topic and succinctly present the main contributions of the papers in two chapters. More specifically, this document is stuctured as follows. Chapter 2 introduces the spatial-wideband effect in THz massive MIMO, details the channel estimation and hybrid combining problems, and present our solution to these problems. Chapter 3 delves into the fundamentals of THz IRSs, with special focus on the near-field modeling and design. Chapter 4 provides concluding remarks and outlines the possible directions for future work.

2 Massive MIMO

2.1 Background

The extremely short wavelength at THz frequencies permits the deployment of thousands of antennas with a small footprint [20]. For example, at carrier frequency $f_c = 300$ GHz, an 80×80-element UPA with half-wavelength spacing incorporates 6400 antennas into an area of 4×4 cm^2. To efficiently implement such a massive MIMO transceiver, a hybrid analog-digital array is therefore adopted, where the number of power-hungry RF chains is much smaller than the number of antennas. However, this limits the beamforming/combining[1] capabilities, because the hybrid antenna array cannot generate arbitrary beampatterns as its fully digital counterpart [21].

This problem becomes quite evident in wideband setups. Specifically, a typical MIMO channel is frequency-selective when the multipath delay spread exceeds the symbol period. Thus, line-of-sight (LoS) channels are frequency-flat in general. In massive MIMO, though, the propagation delay over the array can be multiple times larger than the symbol period. As a result, *spatial-wideband* effects may kick in, making the beampattern of the array vary over the signal bandwidth [22]. Frequency-dependent beamforming is hence indispensable, yet only available in fully digital arrays. In short, novel array architectures and processing techiques are required to reap the full potential of THz massive MIMO.

In the sequel, we present our results on wideband THz systems with a UPA at the BS. It is worth stressing that prior studies (e.g., [23–27] and references therein) on mmWave/THz communication either ignore the spatial-wideband effect or assume linear arrays.[2]

2.2 System Model

Consider the uplink of a THz massive MIMO system, where the BS is equipped with an $N \times M$-element UPA and serves a single-antenna user. The total number of antennas is $N_B = NM$, and the baseband frequency response of the uplink channel is denoted by $\mathbf{h}(f) \in \mathbb{C}^{N_B \times 1}$. In **paper I**, we employed a geometric channel model

[1] Note that beamforming refers to coherent transmission in the downlink, whilst combining corresponds to coherent reception in the uplink. Both techniques rely on the same principle, namely the constructive addition of multiple signals with the aim of increasing the overall signal power.

[2] Linear arrays cannot accommodate a massive number of antennas with a reasonable footprint, and hence are impractical for THz massive MIMO [28].

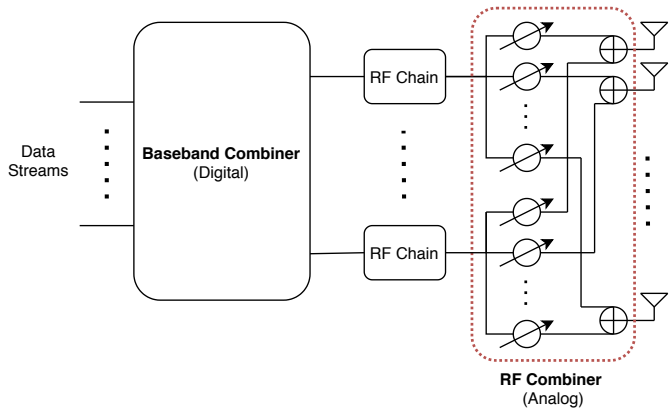

Figure 2.1: Illustration of the hybrid array structure considered in the system model.

consisting of $L+1$ rays; the 0th ray corresponds to the LoS path whereas the other $l = 1, \ldots, L$ rays are non-line-of-sight (NLoS) paths. Then, the frequency response of the uplink channel is expressed as

$$\mathbf{h}(f) = \sum_{l=0}^{L} \beta_l(f)\mathbf{a}(\phi_l, \theta_l, f)e^{-j2\pi f\tau_l} \tag{2.1}$$

where $\beta_l(f)$, τ_l, and (ϕ_l, θ_l) denote the complex gain, time-of-arrival (ToA), and direction-of-arrival (DoA) of the lth propagation path, respectively, whilst

$$\mathbf{a}(\phi, \theta, f) \triangleq \Big[1, \ldots, e^{-j2\pi(f_c+f)\frac{d}{c}(n\sin\theta\cos\phi+m\sin\theta\sin\phi)}, \ldots, e^{-j2\pi(f_c+f)\frac{d}{c}((N-1)\sin\theta\cos\phi+(M-1)\sin\theta\sin\phi)}\Big]^T \tag{2.2}$$

is the *array response vector* of the BS. In (2.2), d is the antenna spacing, f_c is the carrier frequency, and c is the speed of light. We stress that the array response vector reduces to $\mathbf{a}(\phi, \theta, 0)$ in the spatially narrowband case, which holds for a small number of BS antennas and/or signal bandwidth.

Due to the frequency selectivity of the wideband THz channel, orthogonal frequency division multiplexing (OFDM) modulation is employed to combat inter-symbol interference. Specifically, we consider S subcarriers over a signal bandwidth B. Then, the baseband frequency of the sth subcarrier is specified as $f_s = \left(s - \frac{S-1}{2}\right)\frac{B}{S}, s = 0, \ldots, S-1$. A hybrid analog-digital architecture with $N_{\text{RF}} \ll N_B$ RF chains is also considered at the BS, as shown in Fig. 2.1; each RF chain drives the array through N_B analog plain phase shifters. The hybrid combiner for the sth subcarrier is hence expressed as $\mathbf{F}[s] = \mathbf{F}_{\text{RF}}\mathbf{F}_{\text{BB}}[s] \in \mathbb{C}^{N_B \times N_{\text{RF}}}$, where $\mathbf{F}_{\text{RF}} \in \mathbb{C}^{N_B \times N_{\text{RF}}}$ is the frequency-flat RF combiner with elements of constant amplitude, i.e., $\frac{1}{\sqrt{N_B}}$, but variable phase, and $\mathbf{F}_{\text{BB}}[s] \in \mathbb{C}^{N_{\text{RF}} \times N_{\text{RF}}}$ is the baseband combiner. Finally, the post-processed baseband signal, $\mathbf{y}[s] \in \mathbb{C}^{N_{\text{RF}} \times 1}$, for the sth subcarrier is written as

$$\mathbf{y}[s] = \mathbf{F}^H[s]\left(\sqrt{P_d}\mathbf{h}[s]x[s] + \mathbf{n}[s]\right), \tag{2.3}$$

where $\mathbf{h}[s] \triangleq \mathbf{h}(f_s)$ is the correspoding channel, $x[s] \sim \mathcal{CN}(0, 1)$ is the data symbol transmitted at the sth subcarrier, P_d denotes the average power per data symbol

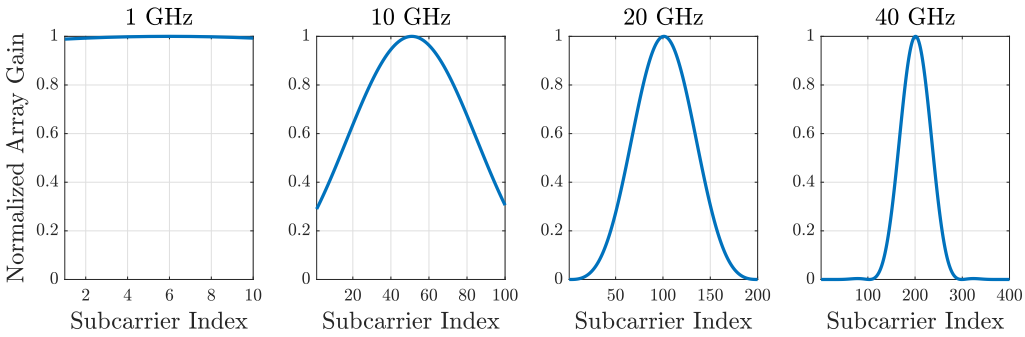

Figure 2.2: Normalized array gain of an 100×100-element UPA for various signal bandwidths; $f_c = 300$ GHz, coherence bandwidth of 100 MHz, and $(\phi, \theta) = (\pi/3, \pi/4)$.

assuming equal power allocation among subcarriers, and $\mathbf{n}[s] \sim \mathcal{CN}(\mathbf{0}, \sigma^2 \mathbf{I}_{N_B})$ is the additive noise vector.

2.3 Hybrid Combining

2.3.1 The Beam Squint Problem

Even for a moderate number of BS antennas, the propagation delay across the array can exceed the symbol period due to the ultra-high bandwidth used in THz communications. This makes the DoA vary over the OFDM subcarriers, causing the so-called *beam squint*. To demonstrate the detrimental effect of beam squint when frequency-flat RF combining is employed, we consider a single ray impinging on the BS array with DoA (ϕ, θ). In the narrowband case, the uplink channel is then given by $\mathbf{h}(0) = \beta \mathbf{a}(\phi, \theta, 0)$. Let $\mathbf{f}_{\text{RF}} = \mathbf{f}/\sqrt{N_B}$ be an arbitrary RF combiner, with $\|\mathbf{f}\|^2 = N_B$. For the combiner $\mathbf{f}_{\text{RF}}$, the power of the received signal is calculated as

$$|\beta|^2 P_d \left| \mathbf{f}^H \mathbf{a}(\phi, \theta, 0) \right|^2 / N_B = |\beta|^2 N_B G(\phi, \theta, 0) P_d, \tag{2.4}$$

where $G(\phi, \theta, f) \triangleq |\mathbf{f}^H \mathbf{a}(\phi, \theta, f)|^2 / N_B^2$ is the *normalized array gain*, which takes values in $[0, 1]$. Choosing $\mathbf{f} = \mathbf{a}(\phi, \theta, 0)$ yields $G(\phi, \theta, 0) = 1$, and hence the maximum gain is obtained. In a wideband setup, though, it holds

$$G(\phi, \theta, f) = \frac{|\mathbf{a}^H(\phi, \theta, 0)\mathbf{a}(\phi, \theta, f)|^2}{N_B^2} = |D_N(2\pi f \Delta_x(\phi, \theta))|^2 \, |D_M(2\pi f \Delta_y(\phi, \theta))|^2 , \tag{2.5}$$

where $\Delta_x(\phi, \theta) \triangleq (d \sin\theta \cos\phi)/c$ and $\Delta_y(\phi, \theta) \triangleq (d \sin\theta \sin\phi)/c$. From (2.5), we have that $G(\phi, \theta, f_s) < 1$, for $f_s > 0$. This behavior is verified in Fig. 2.2. As evinced, the normalized gain significantly decreases over the OFDM subcarriers for very large bandwidths and frequency-flat analog combining. In the following section, we detail our solution to this problem.

2.3.2 Proposed Wideband Combiner

The beam squint problem is inherent in conventional hybrid arrays, as plane phase shifters generate a fixed phase over the whole signal bandwidth [29]. Next, we pro-

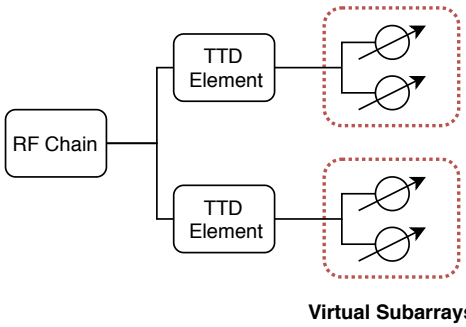

Figure 2.3: Illustration of the TTD-based wideband combiner with virtual subarrays; the circles with arrows represent frequency-flat phase shifters.

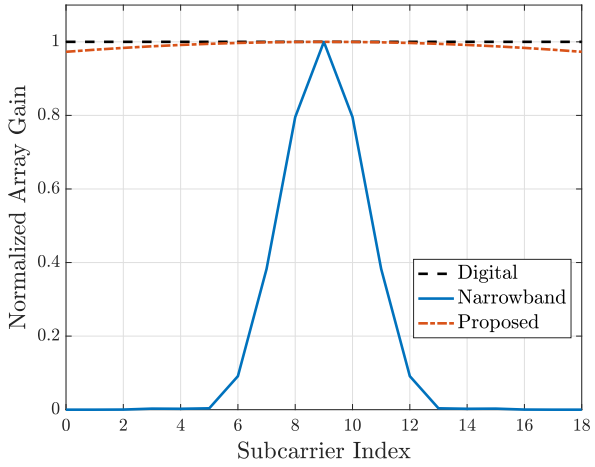

Figure 2.4: Normalized array gain for an 100×100-element UPA. In the proposed scheme, $N_{\mathrm{sb}}M_{\mathrm{sb}} - 1 = 99$ TTD elements are employed. Parameters: LoS channel, single-antenna user, $(\phi_0, \theta_0) = (\pi/4, \pi/3)$, $f_c = 300$ GHz, $B = 40$ GHz, and $S = 18$ subcarriers.

pose a novel TTD-based hybrid array to mitigate beam squint.[3] Since substituting the phase shifters with TTD elements is impractical in terms of hardware cost, complexity, and power consumption, we put forward the idea of *virtual subarrays*. In particular, the antenna array is divided into $N_{\mathrm{sb}} \times M_{\mathrm{sb}}$ virtual subarrays with $\tilde{N}\tilde{M}$ antennas each, where $\tilde{N} \triangleq N/N_{\mathrm{sb}}$ and $\tilde{M} \triangleq M/M_{\mathrm{sb}}$. Each subarray is of small size, and hence its normalized gain is nearly uniform across the OFDM subcarriers for frequency-flat analog combining. To synthesize the beampattern of the whole antenna array, a network of $(N_{\mathrm{sb}}M_{\mathrm{sb}} - 1)$ TTD elements is finally placed between the virtual subarrays, which enable frequency-dependent analog combining; see Fig. 2.3. By doing so, the normalized array gain in (2.5) reduces to

$$G(\phi, \theta, f) = \left|D_{\tilde{N}}(2\pi f \Delta_x)\right|^2 \left|D_{\tilde{M}}(2\pi f \Delta_y)\right|^2 \approx 1, \tag{2.6}$$

where the approximation holds for a properly selected number of TTD elements, as depicted in Fig. 2.4. As evinced, the proposed architecture can effectively combat beam squint with a small number of TTD elements, and hence it is hardware-

[3]In the mmWave literature, beam squint is mainly alleviated by optimizing the hybrid combiner [30–33]. Nevertheless, these approaches are effective only when the beam squint is mild [34]. Consequently, we turn to a hardware-oriented solution in this thesis.

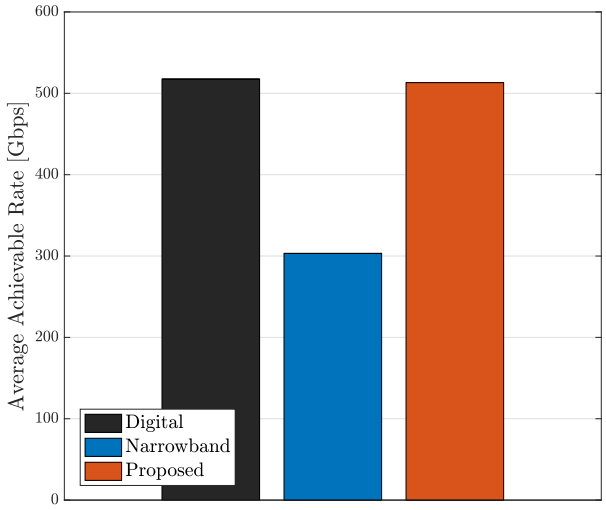

Figure 2.5: Average achievable rate for an 100×100-element UPA. In the proposed scheme, $N_{\mathrm{sb}}M_{\mathrm{sb}} - 1 = 99$ TTD elements are used. The other parameters are: LoS channel, $P_t = 10$ dBm, $\sigma^2 = -174$ dBm/Hz, $f_c = 300$ GHz, $B = 40$ GHz, and $S = 18$ subcarriers.

friendly. We next assess the achievable rate attained by our hybrid combiner. For this purpose, we consider the following baseline schemes:

- A fully-digital array, where the BS employs the frequency-selective combiner $\mathbf{a}(\phi_0, \theta_0, f)/\sqrt{N_B}$.
- A hybrid array, where the BS uses the frequency-flat combiner $\mathbf{a}(\phi_0, \theta_0, 0)/\sqrt{N_B}$.

The average achievable rate is calculated as

$$R = \frac{B}{S} \sum_{s=0}^{S-1} \mathbb{E}\left\{ \log_2 \left(1 + \frac{P_t |\mathbf{f}_{\mathrm{RF}}^H \mathbf{h}[s]|^2}{B\sigma^2} \right) \right\}, \tag{2.7}$$

where the expectation is taken with respect to the DoA, and $\mathbf{f}_{\mathrm{RF}}$ denotes the corresponding combiner. The results are plotted in Fig. 2.5. Specifically, the achievable rates are 517 Gbps, 514 Gbps, and 303 Gbps for the digital, proposed, and narrowband schemes, respectively. Thus, the proposed combiner performs very close to the fully-digital scheme, whilst offering a 40% gain with respect to the narrowband combiner. More importantly, this is accomplished by employing only $N_{\mathrm{sb}}M_{\mathrm{sb}} - 1 = 99$ TTD elements for an 100×100-element UPA, which yields an excellent trade-off between hardware complexity and performance. Lastly, we stress that transmission rates at least 0.5 Tbps can be achieved at a distance of 15 meters through an 100×100-element UPA, which would not be feasible with an equivalent linear array under a footprint constraint.

Remark 2.3.1 (Near-Field Considerations)**.** *In the far-field region, the spherical wavefront of the emitted EM waves degenerates to a plane wavefront, which allows the use of the parallel-ray approximation to derive the array response vector* (2.2)*. Due to the large array aperture of THz massive MIMO, though, near-field considerations are of particular interest. Recall that near-field refers to distances smaller than the Fraunhofer distance* $\mathtt{D}_F \triangleq 2\mathtt{D}_{\max}^2/\lambda$*, where* $\mathtt{D}_{\max}$ *is the maximum dimension*

*of the antenna array, and λ is the carrier wavelength. For a UPA with $N = M$, we have that $\mathtt{D}_{\max}^2 = 2(N-1)^2 d^2$, i.e., length of its diagonal dimension, which yields $\mathtt{D}_F = (N-1)^2\lambda$ for a half-wavelength spacing. For an 100×100-element UPA at $f_c = 300$ GHz, $\mathtt{D}_F \approx 9.8$ meters. As a result, the plane wave assumption may not hold anymore even for distances of multiple meters from the BS. In the Appendix, we extend the proposed TTD-based combiner (Proposition 1 from **paper I**) to the spherical wavefront case.*

2.4 Channel Estimation

So far, we have assumed perfect channel state information (CSI) a the BS. In this section, we investigate the channel estimation problem under the spatial-wideband effect. Specifically, we first formulate a CS problem [35] to estimate the channel at each OFDM subcarrier independently with reduced training overhead. We then propose a wideband dictionary and employ an estimation algorithm that leverages information from multiple subcarriers to increase the reliability of the channel estimates in the low and moderate SNR regimes.

2.4.1 Problem Formulation

Due to the hybrid array structure, the BS can generate up to N_{RF} pilot beams simultaneously, where N_{RF} denotes the number of RF chains. After N_{slot} pilots, the BS hence obtains $N_{\mathrm{beam}} = N_{\mathrm{slot}} N_{\mathrm{RF}}$ measurements collected into the vector $\bar{\mathbf{y}}[s] \in \mathbb{C}^{N_{\mathrm{beam}} \times 1}$ for each OFDM subcarrier. In particular, the measurement vector at the sth subcarrier is written as

$$\bar{\mathbf{y}}[s] = \sqrt{P_p}\, \overline{\mathbf{W}}^H[s]\mathbf{h}[s] + \bar{\mathbf{n}}[s], \tag{2.8}$$

where P_p is the power per pilot, $\overline{\mathbf{W}}[s] \in \mathbb{C}^{N_B \times N_{\mathrm{beam}}}$ is the matrix whose columns correspond to the pilot RF beams during the training period, and $\bar{\mathbf{n}}[s] \in \mathbb{C}^{N_{\mathrm{beam}} \times 1}$ denotes the effective noise. From (2.8), we have N_{beam} variables, whilst $\mathbf{h}[s]$ includes N_B variables. Thus, we need $N_{\mathrm{beam}} \geq N_B$ in order to obtain a good estimate of $\mathbf{h}[s]$. With this condition, the standard least squares (LS) estimate of $\mathbf{h}[s]$ is[4]

$$\hat{\mathbf{h}}^{\mathrm{LS}}[s] = \mathbf{Q}_s^{\dagger} \bar{\mathbf{y}}[s], \tag{2.9}$$

where $\mathbf{Q}_s \triangleq \sqrt{P_p}\, \overline{\mathbf{W}}^H[s] \in \mathbb{C}^{N_{\mathrm{beam}} \times N_B}$ is the sensing matrix. However, the LS estimator (2.9) exhibits the following handicaps: i) it requires $N_{\mathrm{beam}} \geq N_B$, hence yielding a prohibitively high training overhead when the number of RF chains is much smaller than the number of BS antennas; and ii) its mean-square error is $J_s^{\mathrm{LS}} = \sigma^2 N_B / P_p$, which can result in erroneous estimates for a massive number of BS antennas. In conclusion, we have to resort to more sophisticated techniques, which is the theme of the subsequent section.

[4]We consider the LS instead of the minimum mean-square error (MMSE) method because we focus on estimators that exploit only instantaneous CSI.

Algorithm 1 GSOMP-Based Estimator

Input: set $\mathcal{S}$ of pilot subcarriers, sensing matrices $\mathbf{\Phi}_s$ and measurement vectors $\bar{\mathbf{y}}[s], \forall s \in \mathcal{S}$, and a threshold ϵ.

$\mathcal{I}_{-1} = \emptyset$, $\mathcal{G} = \{1, \ldots, G\}$, $\mathbf{r}_{-1}[s] = \bar{\mathbf{y}}[s]$, $\mathsf{MSE} = \sum_{s\in\mathcal{S}} \|\bar{\mathbf{y}}[s]\|^2$, and $l = 0$.
while $\mathsf{MSE} > \epsilon$ **do**
  $g^\star = \arg\max_{g\in\mathcal{G}\setminus\mathcal{I}_{l-1}} \sum_{s\in\mathcal{S}} \left|\mathbf{\Phi}_s^H(g)\mathbf{r}_{l-1}[s]\right|$
  $\mathcal{I}_l = \mathcal{I}_{l-1} \cup \{g^\star\}$
  $\mathbf{r}_l[s] = \left(\mathbf{I}_{N_{\text{beam}}} - \mathbf{\Phi}_s(\mathcal{I}_l)\mathbf{\Phi}_s^\dagger(\mathcal{I}_l)\right)\bar{\mathbf{y}}[s],\ \forall s \in \mathcal{S}$
  $\mathsf{MSE} = \frac{1}{|\mathcal{S}|}\sum_{s\in\mathcal{S}} \|\mathbf{r}_l[s] - \mathbf{r}_{l-1}[s]\|^2$
  $l = l + 1$
end while
$\hat{\bar{\boldsymbol{\beta}}}[s] = \mathbf{\Phi}_s^\dagger(\mathcal{I}_{l-1})\bar{\mathbf{y}}[s], \forall s \in \mathcal{S}$
return $\hat{\mathbf{h}}^{\text{CS}}[s] = \bar{\mathbf{A}}[s]\hat{\bar{\boldsymbol{\beta}}}[s], \forall s \in \mathcal{S}$.

2.4.2 Proposed Wideband Estimator

Sparse Formulation

By availing of the angular sparsity of THz channels, we can have a sparse formulation of the channel estimation problem as follows. The physical channel in (2.1) is recast as

$$\mathbf{h}[s] = \mathbf{A}[s]\boldsymbol{\beta}[s], \tag{2.10}$$

where $\mathbf{A}[s] \triangleq [\mathbf{a}(\phi_0, \theta_0, f_s), \ldots, \mathbf{a}(\phi_L, \theta_L, f_s)] \in \mathbb{C}^{N_B\times(L+1)}$, with $\mathbf{a}(\phi_l, \theta_l, f_s)$ being specified by (2.2) for $f = f_s$, is the so-called wideband array response matrix, and $\boldsymbol{\beta}[s] \triangleq [\beta_0(f_s)e^{-j2\pi f_s\tau_0}, \ldots, \beta_L(f_s)e^{-j2\pi f_s\tau_L}]^T \in \mathbb{C}^{(L+1)\times 1}$ is the vector of channel gains. Next, consider a dictionary $\bar{\mathbf{A}}[s] \in \mathbb{C}^{N_B\times G}$ whose G columns are the array response vectors associated with a predefined set of DoA. Then, the uplink channel can be approximated as

$$\mathbf{h}[s] \approx \bar{\mathbf{A}}[s]\bar{\boldsymbol{\beta}}[s], \tag{2.11}$$

where $\bar{\boldsymbol{\beta}}[s] \in \mathbb{C}^{G\times 1}$ has $L+1$ nonzero entries whose positions and values correspond to their DoA and path gains [**ref**]. Therefore, (2.8) is recast as

$$\bar{\mathbf{y}}[s] = \mathbf{\Phi}_s\bar{\boldsymbol{\beta}}[s] + \bar{\mathbf{n}}[s], \tag{2.12}$$

where $\mathbf{\Phi}_s \triangleq \sqrt{P_p}\ \overline{\mathbf{W}}^H[s]\bar{\mathbf{A}}[s] \in \mathbb{C}^{N_{\text{beam}}\times G}$ is the *equivalent* sensing matrix. Since $(L+1) \ll G$, the channel gain vector $\bar{\boldsymbol{\beta}}[s]$ is $(L+1)$-sparse, and the estimation problem can be formulated as the sparse recovery problem [36]

$$\begin{aligned}\hat{\bar{\boldsymbol{\beta}}}[s] = \arg\min_{\bar{\boldsymbol{\beta}}[s]}\ & \|\bar{\boldsymbol{\beta}}[s]\|_1 \\ \text{s.t.}\quad & \left\|\bar{\mathbf{y}}[s] - \mathbf{\Phi}_s\bar{\boldsymbol{\beta}}[s]\right\|_2 \le \epsilon,\end{aligned} \tag{2.13}$$

where $\epsilon \le \mathbb{E}\{\|\bar{\mathbf{n}}[s]\|_2\}$ is an appropriately chosen bound on the mean magnitude of the effective noise. The above optimization problem can be solved for each subcarrier independently, i.e., single measurement vector formulation. Lastly, the estimate of

$\mathbf{h}[s]$ is obtained as $\hat{\mathbf{h}}^{\mathrm{CS}}[s] = \bar{\mathbf{A}}[s]\hat{\bar{\boldsymbol{\beta}}}[s]$. Several greedy algorithms have been proposed to find approximate solutions of the l_1-norm optimization problem. In this thesis, we choose the OMP algorithm [37] as the basis for our estimator, as it is one of the most common and simple greedy CS methods that can solve (2.13).

Dictionary and Generalized Multiple Measurement Vector Problem

We now introduce a wideband dictionary for UPAs. For half-wavelength antenna separation, the array response vector (2.2) is recast as

$$\mathbf{a}(\omega_x, \omega_y, f) = \Big[1, \ldots, e^{-j2\pi\left(1+\frac{f}{f_c}\right)(n\omega_x + m\omega_y)}, \ldots, e^{-j2\pi\left(1+\frac{f}{f_c}\right)((N-1)\omega_x + (M-1)\omega_y)}\Big]^T, \quad (2.14)$$

where $\omega_x = 1/2 \sin\theta\cos\phi$ and $\omega_y = 1/2 \sin\theta\sin\phi$ are the *spatial frequencies* [38]. Since both ω_x and ω_y lie in $[-1/2, 1/2]$, we consider the grids of discrete spatial frequencies

$$\mathcal{G}_x = \{\bar{\omega}_x(q) = q/G_x,\ q = -(G_x-1)/2, \ldots, (G_x-1)/2\}, \quad (2.15)$$

$$\mathcal{G}_y = \{\bar{\omega}_y(p) = p/G_y,\ p = -(G_y-1)/2, \ldots, (G_y-1)/2\}, \quad (2.16)$$

where $G_x G_y = G$ is the overall dictionary size. By doing so, we can form a frequency-dependent dictionary $\bar{\mathbf{A}}[s] \in \mathbb{C}^{N_B \times G}$, which is used to approximate the uplink channel $\mathbf{h}[s]$ at the sth OFDM subcarrier.

Thanks to the frequency-dependent dictionary, the channel gain vectors $\{\bar{\boldsymbol{\beta}}[s]\}_{s=0}^{S-1}$ share the same support. Therefore, we exploit the common support property and consider the problem in (2.13) as a generalized multiple measurement vector problem, where multiple sensing matrices are employed [39]. To solve the generalized multiple measurement vector problem, we resort to the simultaneous OMP algorithm [40]. The proposed channel estimator, coined as generalized simultaneous OMP (GSOMP), is described in Algorithm 1.

Selected Results

Our performance metric is the normalized mean-square error (NMSE) defined as

$$\mathrm{NMSE} \triangleq \frac{1}{S}\sum_{s=0}^{S-1} \mathbb{E}\left\{\left\|\mathbf{h}[s] - \hat{\mathbf{h}}[s]\right\|^2 / \|\mathbf{h}[s]\|^2\right\}, \quad (2.17)$$

where $\hat{\mathbf{h}}[s]$ denotes the estimate of the corresponding estimator. The NMSE is computed numerically over 100 channel realizations. The complex path gains $\{\beta_l(f_s)\}_{l=1}^{L}$ are generated as $\mathcal{CN}(0, \sigma_\beta^2)$, with $\sigma_\beta^2 = 10^{-9}$, i.e., -90 dB.[5] The average receive SNR is then calculated as $\mathrm{SNR} = \sigma_\beta^2 P_p / P_n$, where $P_p = P_t/S$ is the power per pilot subcarrier, and $P_n = \Delta B \sigma^2$ is the noise power at each subcarrier, with $\Delta B \approx B/S$

[5]The path gains are generated in this way so that we have a single average SNR over the OFDM subcarriers.

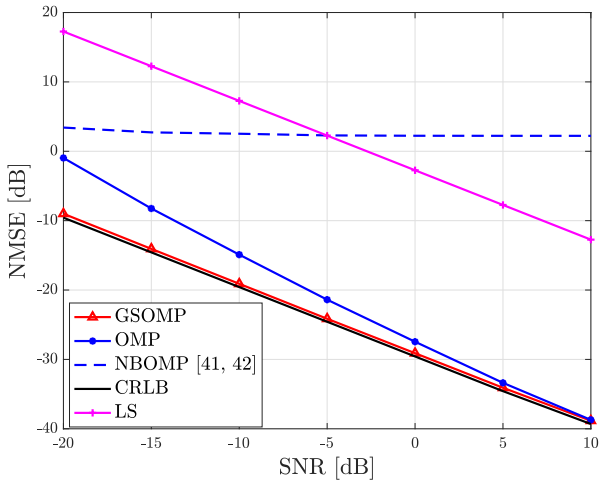

Figure 2.6: NMSE versus SNR. The OMP, NBOMP, and GSOMP estimators are evaluated under partial training of $N_{\text{beam}} = 0.8N_B$ pilot beams; 40×40-element UPA, $N_{\text{RF}} = 2$, NLoS channel with $L = 3$ paths, $f_c = 300$ GHz, $B = 40$ GHz, $S = 400$ subcarriers, and super-resolution dictionary with $G = 4N_B$.

being the subcarrier spacing. In this numerical experiment, we compare the following estimation schemes:

- The LS estimator (2.9) with full pilot training, i.e., $N_{\text{beam}} = N_B$.
- The narrowband OMP-based estimator (NBOMP) with a frequency-flat dictionary [41, 42].
- The OMP-based estimator, but with the proposed wideband dictionary.
- The GSOMP-based estimator and its Cramér-Rao lower bound (CRLB).

The NMSE of each scheme is depicted in Fig. 2.6. As observed, the NMSE of the LS method is prohibitively high since it scales linearly with the number of BS antennas. Likewise, the NBOMP exhibits a very poor performance as it neglects the spatial-wideband effect. Furthermore, the OMP-based estimator fails to successfully recover the common support in the low SNR regime, hence resulting in significant estimation errors. On the other hand, the proposed GSOMP-based estimator accurately detects the common support of the channel gain vectors for all SNR values ranging from -15 dB to 10 dB, thus attaining the CRLB.

2.5 Summary

In **paper I**, we investigated the spatial-wideband effect in THz massive MIMO with a UPA at the BS. In particular:

- We showed that standard analog combining leads to severe degradation of the array gain due to beam squint. More importantly, we derived a closed-form expression for that reduction.

- To address the beam squint problem, we proposed a TTD-based hybrid combiner, which enjoys low-complexity implementation thanks to the virtual subarray rationale. Specifically, our design enables nearly squint-free 3D combining/beamforming.

- For the channel estimation, we exploited the inherent sparsity of THz channels to employ CS techniques and reduce the CSI acquisition overhead. More specifically, we introduced a wideband dictionary and employed a novel variant of the simultaneous OMP. The resulting estimator, termed GSOMP, has exellent performance even in the low SNR regime.

3 Intelligent Reflecting Surfaces

3.1 Why Near-Field?

The severe path attenuation at THz bands along with the sub-wavelength size of each IRS element requires an electrically large IRS consisting of thousands of elements. Furthermore, in order to compensate for this path attenuation with a practical number of reflecting elements, the Tx or Rx has to work near the IRS. Consequently, the Tx/Rx is expected to be in the radiating near-field, i.e., Fresnel zone, of the IRS, where the spherical wavefront of the radiated waves cannot be ignored. Note that the Fresnel region includes all distances r from the IRS satisfying [43, Ch. 2]

$$0.62\sqrt{L_{\text{IRS}}^3/\lambda} < r \leq 2L_{\text{IRS}}^2/\lambda, \tag{3.1}$$

where λ is the wavelength, and L_{IRS} denotes the maximum dimension of the IRS.

Table 3.1: Key parameters of a rectangular IRS at $f = 300$ GHz.

IRS Size	Physical Size [m^2]	Fresnel Region [m]
$40\lambda \times 40\lambda$	0.039×0.039	$[0.15, 3.2]$
$50\lambda \times 50\lambda$	0.05×0.05	$[0.22, 5]$
$100\lambda \times 100\lambda$	0.1×0.1	$[0.62, 20]$

From Table 3.1, we observe that although an electrically large THz IRS occupies a small area in the order of square centimeters, its Fresnel region spans several meters. Thus, the far-field assumption of plane waves, which is acccurate for distances $r \gg 2L_{\text{IRS}}^2/\lambda$, starts becoming invalid as the IRS size grows. In conclusion, near-field propagation should be considered in most cases of interest. In light of these observations, a stream of recent papers [44–46] proposed a near-field channel model for IRSs, but using the popular "$\cos^q$" model [47] for the radiation pattern of each IRS element, and then choosing the parameter q according to experimental measurements. However, this approach exhibits limitations, as it does not provide a comprehensive electromagnetic-based framework for modeling the path loss. For example, different IRS orientations can yield different radiation patterns, and more importantly, they may change the polarization of the incident wave; hence, polarization mismatch losses must be taken into account as well.

To fill this gap in the literature, we invoke *physical optics* from EM theory to derive a near-field channel model. Since physical optics is an approximation, our analysis constitutes a first step toward EM-aware modeling of IRSs at THz

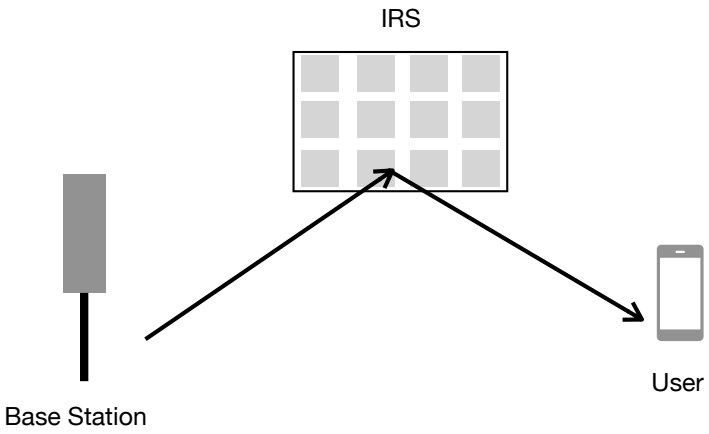

Figure 3.1: Illustration of an IRS-aided THz system.

Table 3.2: Main notation used in the channel model of discrete IRSs.

Notation	**Description**
$N = N_1 \times N_2$	Number of IRS elements
$L_x \times L_y$	Area of each reflecting element
$\varphi_{n,m}$	Phase induced by the (n,m)th IRS element
λ	Carrier wavelength
f	Carrier frequency
$k = 2\pi/\lambda$	Wavenumber
r_t	Radial distance of the Tx
$r_t(n,m)$	Distance between the Tx and the (n,m)th IRS element
r_r	Radial distance of the Rx
$r_r(n,m)$	Distance between the Rx and the (n,m)th IRS element

frequencies. In the following sections, we succinctly present the main results from **papers II-IV**.

3.2 Discrete IRSs

Consider an IRS-assisted THz system, as shown in Fig. 3.1. The Tx and Rx are equipped with a single antenna each. The IRS is modeled as a rectangular array of $N = N_1 \times N_2$ reflecting elements. Each IRS element can add a phase shift to the incident signal, and hence the reflection coefficient of the (n,m)th element is given by $e^{j\varphi_{n,m}}$, $\varphi_{n,m} \in [-\pi, \pi]$. Then, the baseband received signal is written as[1]

$$y = \sum_{n=0}^{N_1-1} \sum_{m=0}^{N_2-1} h_{n,m} e^{j\varphi_{n,m}} x + \tilde{n}, \tag{3.2}$$

where $h_{n,m} \in \mathbb{C}$ is the cascaded channel through the (n,m)th IRS element, x is the transmitted data symbol, $\mathbb{E}[|x|^2] = P_t$ is the average power per data symbol, and

[1]The Tx-Rx channel can be very weak for single-antenna transceivers, or it can be blocked by an obstacle. It is hence neglected; besides, our main focus is on modeling the Tx-IRS-Rx link.

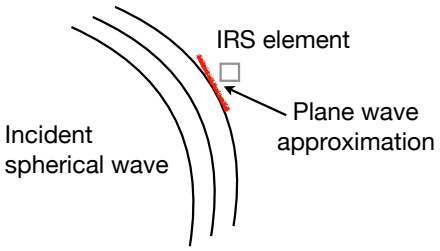

Figure 3.2: Illustration of the plane wave approximation over a single IRS element.

$\tilde{n} \sim \mathcal{CN}(0, \sigma^2)$ is the additive noise. Based on (3.2), the SNR is given by

$$\text{SNR} = \frac{P_t}{\sigma^2} \left| \sum_{n=0}^{N_1-1} \sum_{m=0}^{N_2-1} h_{n,m} e^{j\varphi_{n,m}} \right|^2 . \tag{3.3}$$

One critical question here is how to model the channel coefficients $\{h_{n,m}\}$, which play a key role in the IRS configuration, i.e., $\{\varphi_{n,m}\}$ and, ultimately, in the performance of the IRS-aided link.

3.2.1 Spherical Wave Channel Model

Due to the limited multipath scattering at THz frequencies, we consider LoS propagation for the Tx-IRS and IRS-Rx links. The channel coefficient $h_{n,m}$ is then expressed as

$$h_{n,m} = \sqrt{\text{PL}_{n,m}} e^{-jk(r_t(n,m)+r_r(n,m))}, \tag{3.4}$$

where $\text{PL}_{n,m}$ is the path loss through the (n,m)th IRS element, $k = \frac{2\pi}{\lambda}$ is the wavenumber, λ is the carrier wavelength, while $r_t(n,m)$ and $r_r(n,m)$ are the distances from the Tx and Rx to the (n,m)th IRS element, respectively. The parameters $\text{PL}_{n,m}$, $r_t(n,m)$, and $r_r(n,m)$ depend on the IRS orientation and area of its elements, as well as in the Tx and Rx locations. In **paper II**, we assumed that the IRS lies in the xy-plane, each reflecting element is of size $L_x \times L_y$, and the coordinate system is placed at the center of the $(0,0)$th IRS element. Then, the position vector of the (n,m)th IRS element is $\mathbf{p}_{n,m} = (nL_x, mL_y, 0)$. Also, the Tx and Rx locations are described in Cartesian coordinates by the vectors

$$\mathbf{p}_t = (x_t, y_t, z_t) = (r_t \cos\phi_t \sin\theta_t, r_t \sin\phi_t \sin\theta_t, r_t \cos\theta_t), \tag{3.5}$$

$$\mathbf{p}_r = (x_r, y_r, z_r) = (r_r \cos\phi_r \sin\theta_r, r_r \sin\phi_r \sin\theta_r, r_r \cos\theta_r), \tag{3.6}$$

where r, ϕ, and θ denote the corresponding radial distances, azimuth angles, and polar angles, respectively. Although the EM wave emitted by the Tx has a spherical wavefront, we can assume a plane wavefront over a single IRS element owing to its very small size,[2] as depicted in Fig. 3.2. Under this assumption, we can now specify the path loss $\text{PL}_{n,m}$ using the physical optics approach for a rectangular conducting plate of size $L_x \times L_y$ and an incident plane wave that is linearly polarized along the

[2]Each IRS element is of sub-wavelength size in order to act as an isotropic scatterer [48].

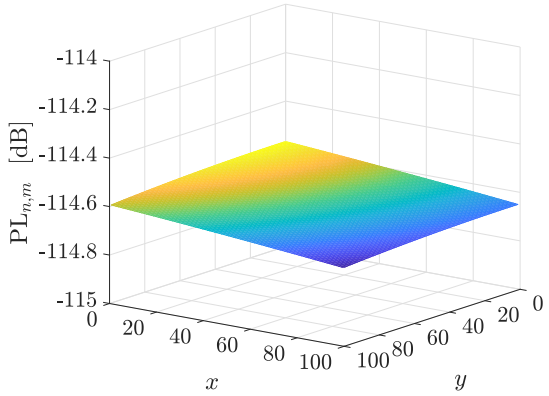

Figure 3.3: Path loss over an 100×100-element IRS. The other parameters are: $f = 300$ GHz, $\kappa_{\text{abs}}(f) = 0.0033$ m^{-1}, $L_x = L_y = \lambda/2$, $G_t = G_r = 20$ dBi, $\mathbf{p}_t = (0, -0.3, 0.6)$, $r_t = 0.67$ m, $\mathbf{p}_r = (0, 1, 1)$, and $r_r = 1.41$ m.

x-axis. By doing so, we obtain

$$\mathrm{PL}_{n,m} = \frac{G_t G_r (L_x L_y)^2}{(4\pi r_t(n,m) r_r(n,m))^2} F(\theta_t, \phi_r, \theta_r) e^{-\kappa_{\text{abs}}(f)(r_t(n,m)+r_r(n,m))}, \tag{3.7}$$

where G_t and G_r are the gains of the Tx and Rx antennas, respectively, $\kappa_{\text{abs}}(f)$ is the molecular absorption coefficient at frequency f, $e^{-\kappa_{\text{abs}}(f)(r_t(n,m)+r_r(n,m))}$ accounts for the molecular absorption loss in THz frequency bands [49], and $F(\theta_t, \phi_r, \theta_r) = \cos^2\theta_t(\cos^2\theta_r\cos^2\phi_r + \sin^2\phi_r)$. Note that the path loss through an IRS element depends on the reciprocal of the product $(r_t r_r)^2$ rather than of the sum $(r_t + r_r)^2$, as in the case of specular reflection [50]. Consequently, the path loss of each cascaded channel is very high in general.

We next plot $\mathrm{PL}_{n,m}$ for an electrically large IRS. From Fig. 3.3, we evince that $\mathrm{PL}_{n,m}$ marginally changes across the IRS even for $N = 100^2$ elements and a Tx distance $r_t = 0.67$ m. This is because of the small physical size of THz IRSs. In particular, the 100×100-element IRS occupies only 5×5 cm^2 for $L_x = L_y = \lambda/2$ at $f = 300$ GHz, as $\lambda = 10^{-3}$ m. Hereafter, we consider $\mathrm{PL}_{n,m} \approx \mathrm{PL}$, where PL denotes the path loss calculated using the radial distances r_t and r_r. In light of this observation, the SNR in (3.3) is recast as

$$\begin{aligned}
\mathrm{SNR} &= \frac{P_t}{\sigma^2}\left|\sum_{n=0}^{N_1-1}\sum_{m=0}^{N_2-1}\sqrt{\mathrm{PL}_{n,m}}e^{-jk(r_t(n,m)+r_r(n,m))}e^{j\varphi_{n,m}}\right|^2 \\
&\approx \frac{N^2 P_t \mathrm{PL}}{\sigma^2}\underbrace{\frac{\left|\sum_{n=0}^{N_1-1}\sum_{m=0}^{N_2-1}e^{-jk(r_t(n,m)+r_r(n,m))}e^{j\varphi_{n,m}}\right|^2}{N^2}}_{G} \\
&= \frac{N^2 G P_t \mathrm{PL}}{\sigma^2},
\end{aligned} \tag{3.8}$$

where $G \in [0, 1]$ is the *normalized power gain*. With the proper IRS configuration, $G = 1$ and a power gain of N^2 is attained, which scales quadratically with the number N of IRS elements [51].

3.2.2 Near-Field Beamfocusing

The N^2-power gain is obtained when the phase shift induced by the (n,m)th IRS element is

$$\varphi_{n,m} = k(r_t(n,m) + r_r(n,m)), \tag{3.9}$$

where

$$\begin{aligned} r_t(n,m) &\triangleq \|\mathbf{p}_t - \mathbf{p}_{n,m}\| \\ &= r_t\sqrt{1 + \frac{(nL_x)^2}{r_t^2} - \frac{2\cos\phi_t \sin\theta_t nL_x}{r_t} + \frac{(mL_y)^2}{r_t^2} - \frac{2\sin\phi_t \sin\theta_t mL_y}{r_t}}, \end{aligned} \tag{3.10}$$

and

$$\begin{aligned} r_r(n,m) &\triangleq \|\mathbf{p}_r - \mathbf{p}_{n,m}\| \\ &= r_r\sqrt{1 + \frac{(nL_x)^2}{r_r^2} - \frac{2\cos\phi_r \sin\theta_r nL_x}{r_r} + \frac{(mL_y)^2}{r_r^2} - \frac{2\sin\phi_r \sin\theta_r mL_y}{r_r}}. \end{aligned} \tag{3.11}$$

The phase shift design in (3.9) is referred to as *near-field beamfocusing* because the IRS focuses the incident wave onto the Rx point (x_r, y_r, z_r) rather than toward the Rx direction (θ_r, ϕ_r) [52]. We stress that a different design will yield $G \leq 1$.

3.2.3 Far-Field Beamforming

We now analyze the power gain under conventional far-field beamforming. Specifically, in the far-field, the spherical wavefront degenerates into a plane wave, which enables the use of the parallel-ray approximations

$$r_t(n,m) \approx r_t - nL_x\cos\phi_t\sin\theta_t - mL_y\sin\phi_t\sin\theta_t, \tag{3.12}$$

$$r_r(n,m) \approx r_r - nL_x\cos\phi_r\sin\theta_r - mL_y\sin\phi_r\sin\theta_r. \tag{3.13}$$

Mathematically speaking, (3.12) and (3.13) follow from the first-order Taylor expansion $(1+x)^a \approx 1 + ax$ of (3.10) and (3.11). In far-field beamforming, the phase shifts are designed based on the angular information (θ_t, ϕ_t) and (θ_r, ϕ_r), i.e.,

$$\begin{aligned} \varphi_{n,m} = -k(&nL_x\cos\phi_t\sin\theta_t + mL_y\sin\phi_t\sin\theta_t \\ &+ nL_x\cos\phi_r\sin\theta_r + mL_y\sin\phi_r\sin\theta_r). \end{aligned} \tag{3.14}$$

As a result, it can be highly suboptimal in the Fresnel zone. To analytically characterize the reduction in the power gain, we first consider that the IRS is deployed close to the Tx, and hence the Rx is in the far-field.[3] We then exploit the Fresnel

[3] In fact, deploying the IRS close to one of the link ends yields the maximum SNR, compared to placing it somewhere in between [53].

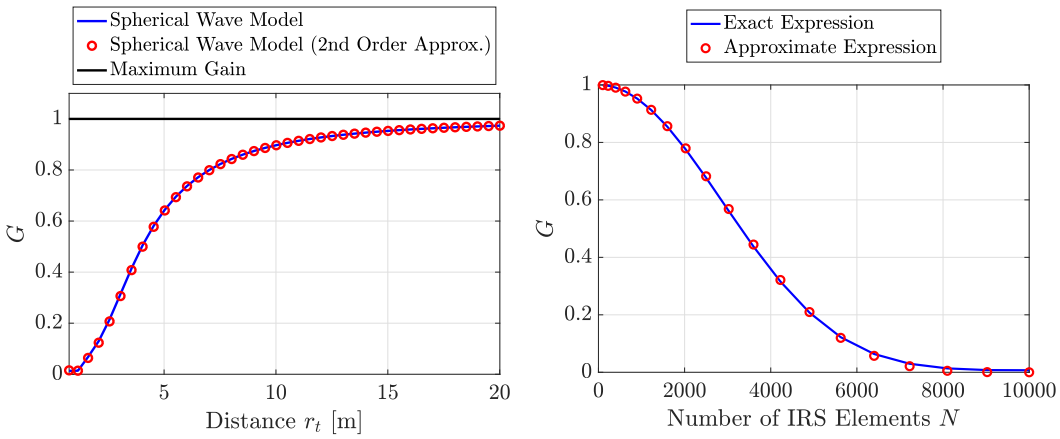

(a) (b)

Figure 3.4: Results for far-field beamforming: (a) normalized power gain versus distance r_t for an 100×100-element IRS, $\mathbf{p}_t = (0.4, 0.4, z)$, $0.5 \leq z \leq 10$, and $0.755 \leq r_t \leq 10.016$ m; (b) normalized power gain versus number of IRS elements N for $\mathbf{p}_t = (0.4, 0.4, 1)$, and $r_t = 1.15$ m. The other parameters are $f = 300$ GHz, and $L_x = L_y = \lambda/2$.

approximation [54] of the Tx distance

$$r_t(n,m) \approx r_t + \frac{(nL_x)^2(1-\cos^2\phi_t \sin^2\theta_t)}{2r_t} - nL_x \cos\phi_t \sin\theta_t + \frac{(mL_y)^2(1-\sin^2\phi_t \sin^2\theta_t)}{2r_t} - mL_y \sin\phi_t \sin\theta_t. \tag{3.15}$$

By combining (3.14) and (3.15), the normalized power gain is recast as

$$G = \frac{\left|\sum_{n=0}^{N_1-1} e^{-jk\frac{(nL_x)^2(1-\cos^2\phi_t \sin^2\theta_t)}{2r_t}}\right|^2}{N_1^2} \frac{\left|\sum_{m=0}^{N_2-1} e^{-jk\frac{(mL_y)^2(1-\sin^2\phi_t \sin^2\theta_t)}{2r_t}}\right|^2}{N_2^2}, \tag{3.16}$$

which admits the approximation

$$\begin{aligned} G &\approx \frac{\left|\sum_{n=0}^{N_1^2-1} e^{-jk\frac{nL_x^2(1-\cos^2\phi_t \sin^2\theta_t)}{2r_t}}\right|^2}{N_1^4} \frac{\left|\sum_{m=0}^{N_2^2-1} e^{-jk\frac{mL_y^2(1-\sin^2\phi_t \sin^2\theta_t)}{2r_t}}\right|^2}{N_2^4} \\ &= \left|D_{N_1^2}\left(\frac{2\pi}{\lambda}\frac{L_x^2(1-\cos^2\phi_t \sin^2\theta_t)}{2r_t}\right)\right|^2 \left|D_{N_2^2}\left(\frac{2\pi}{\lambda}\frac{L_y^2(1-\sin^2\phi_t \sin^2\theta_t)}{2r_t}\right)\right|^2, \end{aligned} \tag{3.17}$$

where $D_N(x) = \frac{\sin(Nx/2)}{N\sin(x/2)}$ denotes the Dirichlet sinc function.

The validity of the Fresnel approximation (3.15) is depicted in Fig. 3.4(a). Furthermor, the accuracy of the approximate closed-form expression (3.17) is evaluated in Fig. 3.4(b), which exhibits a very good match with the exact expression (3.16). Most importantly, we observe that beamforming substantially decreases the power gain when the Tx operates in the near-field of an electrically large IRS. Lastly, by availing of (3.17), we have the asymptotic result $G \to 0$ as $N \to \infty$. This implies that for a finite yet large number N of IRS elements, the total power gain N^2G tends

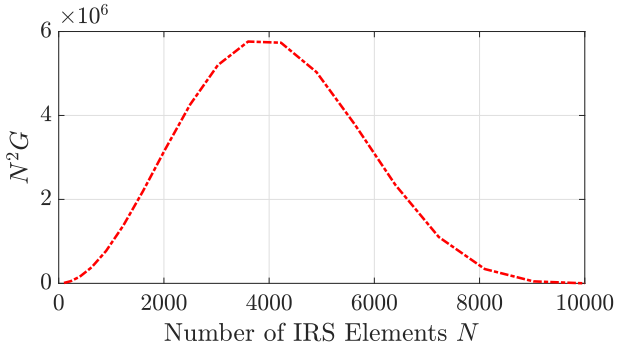

Figure 3.5: Power gain versus number of IRS elements N for $\mathbf{p}_t = (0.4, 0.4, 1)$, $r_t = 1.15$ m, $f = 300$ GHz, and $L_x = L_y = \lambda/2$.

to zero as N grows, which is demonstrated in Fig. 3.5. In conclusion, the reduction in the power gain cannot be compensated by increasing the number of IRS elements, and hence, near-field beamfocusing is the optimal mode of operation for THz IRSs.

3.2.4 Performance Analysis

Energy Efficiency

Capitalizing on the channel model of Section 3.2.1, we now investigate if IRS-aided MIMO can achieve higher EE than MIMO. Before proceeding, we briefly present the corresponding models.

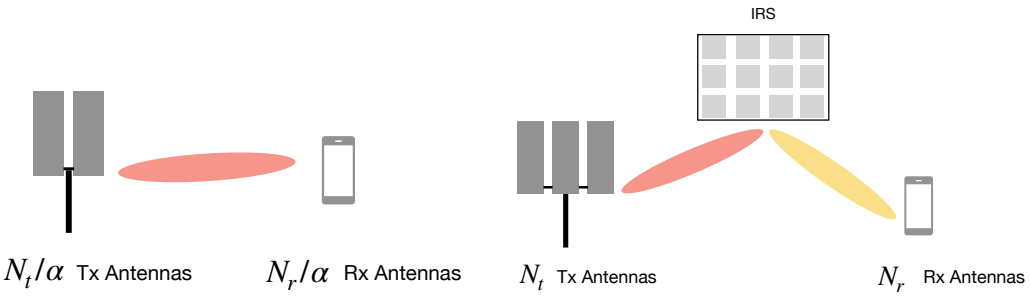

(a) MIMO

(b) IRS-aided MIMO

Figure 3.6: Illustration of the systems under investigation.

MIMO System: Consider a MIMO system where the Tx and Rx are equipped with N_t and N_r antennas, respectively. For efficient hardware implementation, hybrid array architectures are assumed at both link ends. The Tx seeks to communicate a single data stream to the Rx through a LoS channel, whose path loss is calculated using the Friss transmission formula

$$\mathrm{PL}_{\mathrm{MIMO}} = \frac{G_t G_r \lambda^2}{(4\pi r_d)^2} e^{-\kappa_{\mathrm{abs}}(f) r_d}, \tag{3.18}$$

where $r_d = \|\mathbf{p}_r - \mathbf{p}_t\|$. For an adequately small N_r and N_t, far-field propagation can be assumed. In this case, the LoS channel is rank-one [55, Ch. 7]. Hence, analog

beamforming and combining yield the received SNR

$$\mathrm{SNR}_{\mathrm{MIMO}} = \frac{N_r N_t P_t \mathrm{PL}_{\mathrm{MIMO}}}{\sigma^2}. \tag{3.19}$$

Lastly, the respective power consumption is calculated as[4]

$$P_{\mathrm{MIMO}} = P_t + N_r(P_{\mathrm{PS}} + P_{\mathrm{PA}}) + N_t(P_{\mathrm{PS}} + P_{\mathrm{PA}}), \tag{3.20}$$

where P_{PS} and P_{PA} denote the power consumption values for a phase shifter and a power amplifier, respectively.

IRS-Aided MIMO System: The Tx and Rx perform beamforming and combining to communicate a single stream through an N-element IRS. Due to the directional transmissions, the Tx-Rx link is very weak, and hence is ignored. In **paper II**, it was shown that the received SNR of this system is given by

$$\mathrm{SNR}_{\mathrm{IRS}} = \frac{N_t N_r N^2 P_t \mathrm{PL}_{\mathrm{IRS}}}{\sigma^2}, \tag{3.21}$$

where $\mathrm{PL}_{\mathrm{IRS}}$ denotes the path loss of the IRS-aided link in (3.7). The phase of each IRS element is controlled by a varactor diode, which consumes a negligible power compared to a typical phase shifter. Thus, the power expenditure of each reflecting element is set to $P_{\mathrm{e}} = 0$ [45], and the total power consumption of the IRS-assisted MIMO system is specified as $P_{\mathrm{IRS}} \approx P_{\mathrm{MIMO}}$. The power consumption parameters are summarized in the following table.

Proposition 3.2.1. *The IRS-aided MIMO system with N_t/α and N_r/α antennas, where α is a positive integer, attains a higher SNR than MIMO with N_t and N_r antennas for*

$$N^\star \geq \alpha \frac{\lambda}{L_x L_y} \frac{D_t D_r}{\sqrt{F(\theta_t, \phi_r, \theta_r) D_d}} e^{-\frac{1}{2}\kappa_{\mathrm{abs}}(f)(D_d - D_r - D_t)}. \tag{3.22}$$

Proof. Using (3.19) and (3.21), the IRS-aided system achieves a higher SNR for $N^\star \geq \sqrt{\alpha^2 \mathrm{PL}_{\mathrm{MIMO}}/\mathrm{PL}_{\mathrm{IRS}}}$, which gives the desired result after basic algebra. □

According to Proposition 3.2.1, we can decrease the number of Tx and Rx antennas by a factor α to reduce the power consumption as

$$P_{\mathrm{IRS}}(N_t/\alpha, N_r/\alpha) = P_t + \frac{N_r}{\alpha}(P_{\mathrm{PS}} + P_{\mathrm{PA}}) + \frac{N_t}{\alpha}(P_{\mathrm{PS}} + P_{\mathrm{PA}}) \approx P_{\mathrm{MIMO}}/\alpha, \tag{3.23}$$

while keeping the achievable rate fixed. Consequently, the EE gain with respect to MIMO is approximately equal to α.

Let B denote the transmit bandwidth. The achievable rate is finally calculated as

$$R = B \log_2(1 + \mathrm{SNR}_{\mathrm{IRS}}), \tag{3.24}$$

whilst the EE is given by $\mathrm{EE} \triangleq R/P_{\mathrm{IRS}}$. In our numerical experimental, we consider a MIMO setup with $N_t = N_r = 100$ antennas, e.g., 10×10-element uniform planar

[4]The power consumption of signal processing is neglected.

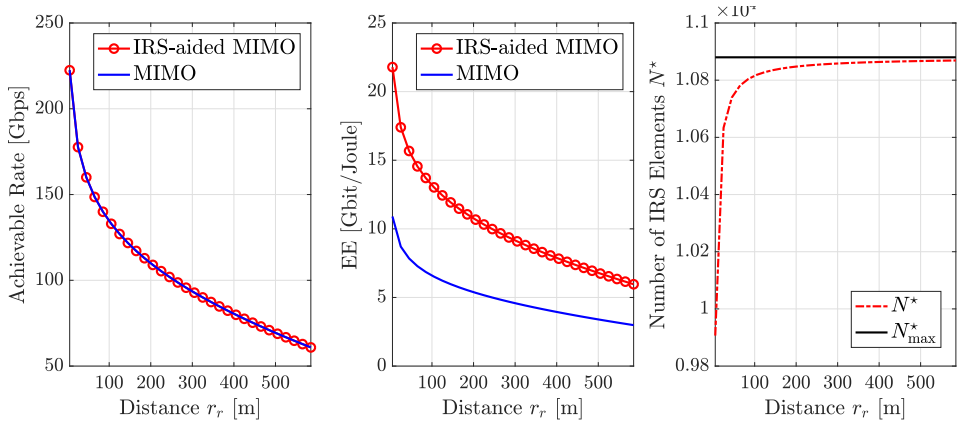

Figure 3.7: Achievable rate, EE, and number $N^\star$ of IRS elements versus distance r_r for $\alpha = 2$ and a fixed IRS location at $(0, 0, 0)$. In the MIMO system, $N_t = 100$ and $N_r = 100$. The other parameters are as follows: $G_t = G_r = 20$ dBi, $P_t = 10$ dBm, $P_{\text{PS}} = 42$ mW and $P_{\text{PA}} = 60$ mW [56], $\sigma^2 = -174$ dBm/Hz, $B = 10$ GHz, $f = 300$ GHz, $L_x = L_y = \lambda/2$, $\mathbf{p}_t = (0, -0.6, 1)$ with $r_t = 1.16$ m, and $\mathbf{p}_r = (0, r_r, 1)$.

arrays. From Fig. 3.7, we verify that the IRS-assisted system, with $N_t = N_r = 50$ antennas and $N^\star = 10,880$ reflecting elements, offers a two-fold EE gain. Specifically, an IRS can provide an alternative communication link, in addition to LoS, where the Tx and Rx employ a smaller number of antennas to communicate with each other, hence reducing the power consumption of the system. However, note that the suggested benefits are valid when: i) the power expenditure of IRS elements is negligible compared to that of conventional phase shifters; ii) the Tx operates near the IRS in order to have a reasonable number $N^\star$ of reflecting elements; and iii) reflection losses are small [57].

Remark 3.2.1. *In our EE analysis, we assumed $P_e \approx 0$, which implies that the IRS can have an arbitrarily large number of IRS elements without increasing the power consumption of the system. Since this assumption may not be realistic, we derive the necessary condition for having EE gains even when $P_e > 0$. Specifically, we need*

$$P_{\text{MIMO}} > P_{\text{IRS}} \Rightarrow P_{\text{MIMO}} > N^\star P_e + P_{\text{MIMO}}/\alpha \Rightarrow P_e < \frac{P_{\text{MIMO}}(1 - 1/\alpha)}{N^\star}. \quad (3.25)$$

For example, in the previous numerical experiment with $\alpha = 2$ and $N^\star = 10,880$ elements, P_e should be roughly smaller than 1 mW to attain an EE gain. As a result, the nearly passive implementation of THz IRSs is of paramount importance.

Optimal IRS Placement

We now study the impact of the IRS position on the number $N^\star$ of reflecting elements. For the deployment considered in Fig. 3.7, r_t is small, and hence $r_r^2 \approx r_t^2 + r_d^2$. Further, $\phi_r = \pi/2$ which gives $F(\theta_t, \phi_r, \theta_r) = \cos^2 \theta_t$. Then, (3.22) reduces to

$$N^\star = \alpha \frac{\lambda}{L_x L_y} \frac{r_t r_r}{\cos\theta_t \sqrt{r_r^2 - r_t^2}} e^{-\frac{1}{2}\kappa_{\text{abs}}(f)(\sqrt{r_r^2 - r_t^2} - r_r - r_t)}, \quad (3.26)$$

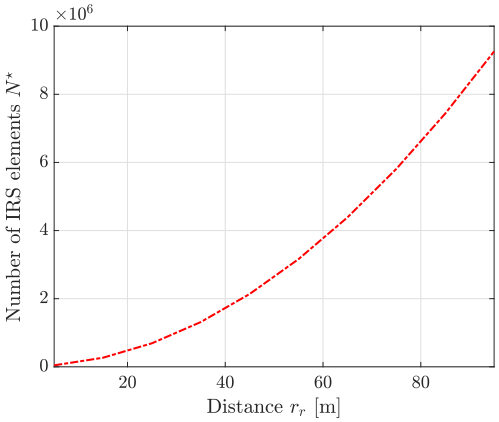

Figure 3.8: Number of IRS elements $N^\star$ versus distance r_r for $\alpha = 2$; $\mathbf{p}_t = (0, -0.6, 1)$, $\mathbf{p}_r = (0, r_r, 1)$, IRS at $(0, (r_r - y_t)/2, 1)$ with $y_t = -0.6$, $f = 300$ GHz, $\kappa_{\text{abs}}(f) = 0.0033\ \text{m}^{-1}$, and $L_x = L_y = \lambda/2$.

which takes the asymptotic value

$$N^\star_{\max} = \alpha \frac{\lambda}{L_x L_y} \frac{r_t}{\cos\theta_t} e^{\frac{1}{2}\kappa_{\text{abs}}(f) r_t} \tag{3.27}$$

as $r_r \to \infty$; this follows from $\sqrt{r_r^2 - r_t^2} \approx r_r$ for $r_r \gg r_t$. As evinced, $N^\star$ is bounded for a fixed IRS position near the Tx. We stress that due to symmetry, the same result holds when the IRS is near the Rx. For instance, $N^\star_{\max} = 10,880$ in Fig. 3.7. In contrast, when the IRS is deployed always in the middle of the link ends, $N^\star$ increases as $O(r_t r_r)$. This scaling law is depicted in Fig. 3.8. In short, the IRS has to be close to one of the link ends to compensate for the high propagation losses with a practical number of reflecting elements.

3.2.5 Summary

In **paper II**, we studied IRS-aided THz communications. In particular:

- We introduced a spherical wave channel model to characterize the near-field response of discrete THz IRSs. The path loss of the IRS-aided link was derived using physical optics and assuming a plane wavefront over each IRS element.
- We showed that conventional beamforming is highly suboptimal in the Fresnel zone, and hence can reduce the power gain. More importantly, we provided an approximate yet accurate expression for evaluating that reduction.
- We demonstrated that IRS-aided MIMO can achieve much higher EE than MIMO through nearly passive beamfocusing; hence, ultra-low power IRSs are key enablers of energy-efficient communications.
- We proved that the IRS must be placed close to one of the link ends, otherwise an extremely large (and hence impractical) number of IRS elements are needed to mitigate the severe path loss of the Tx-IRS-Rx link.

3.3 Holographic IRSs

So far, we treated the IRS as a rectangular array of sub-wavelength reflecting elements. This enabled us to assume a plane wavefront over each individual element, and hence employ existing results from physical optics, i.e., plane scattering from a rectangular plate, to specify the path loss of the IRS-aided link. In this section, we extend the previous analysis to the so-called holographic IRS, which integrates a virtually infinite number of elements into a limited area to form a spatially continuous aperture [58, 59].[5] Since the plane wave approximation cannot be applied to large holographic IRSs, we resort to spherical waves. Thus, we provide some background on spherical waves, and then introduce the near-field channel model.

3.3.1 Spherical Waves

The Tx antenna is modeled as an infinitesimal dipole of length $\ell \ll \lambda$, which is placed parallel to the z-axis. In spherical coordinates, the electric field (E-field) at a distance r is then given by [61, Ch. 6]

$$\mathbf{E} = -j\frac{I_0\ell\eta\cos\theta}{2\pi k}\left(\frac{jk}{r^2}+\frac{1}{r^3}\right)e^{-jkr}\mathbf{e}_r - j\frac{I_0\ell\eta\sin\theta}{4\pi k}\left(\frac{-k^2}{r}+\frac{jk}{r^2}+\frac{1}{r^3}\right)e^{-jkr}\mathbf{e}_\theta, \tag{3.28}$$

where $k = 2\pi/\lambda$ is the wavenumber, η is the free-space impedance, and I_0 is the excitation current. For any distance $r \gg \lambda$, the high-order terms $1/r^2$ and $1/r^3$ can be neglected. Hence, the radiated E-field is approximated by

$$\mathbf{E} \approx j\frac{I_0\ell\eta k\sin\theta}{4\pi r}e^{-jkr}\mathbf{e}_\theta = E_\theta\mathbf{e}_\theta. \tag{3.29}$$

Remark 3.3.1. *For notational convenience,* (3.29) *can be recast as*

$$\mathbf{E} = j\sqrt{\frac{2\eta PG(\theta)}{4\pi}}\frac{e^{-jkr}}{r}\mathbf{e}_\theta, \tag{3.30}$$

where $G(\theta) = \frac{3}{2}\sin^2\theta$ *and* $P = \frac{\eta(I_0\ell k)^2}{12\pi}$ *are the gain and total radiated power of the infinitesimal dipole, respectively.*

Hereafter, we will use (3.30) to represent spherical waves. Lastly, the associated magnetic field is specified according to the Maxwell's equation

$$\mathbf{H} = \frac{j}{\eta k}\nabla\times\mathbf{E} = \frac{j}{\eta k}\frac{1}{r}\frac{\partial(rE_\theta)}{\partial r}\mathbf{e}_\phi = \frac{j}{\eta}\sqrt{\frac{2\eta PG(\theta)}{4\pi}}\frac{e^{-jkr}}{r}\mathbf{e}_\phi = H_\phi\mathbf{e}_\phi, \tag{3.31}$$

whereas the power density ($\mathrm{W/m^2}$) at a distance r is calculated as

$$S_s = \frac{1}{2}E_\theta H_\phi^* = \frac{1}{2\eta}\|\mathbf{E}\|^2 = \frac{PG(\theta)}{4\pi r^2}. \tag{3.32}$$

[5] The operation of a spatially continuous aperture can be explained by optical holography, where the impinging EM field is recorded and then reconstructed. Please refer to [60] for more details.

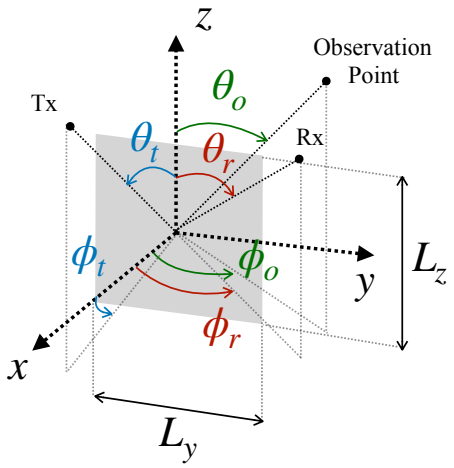

Figure 3.9: Illustration of the IRS geometry under consideration.

3.3.2 Spherical Wave Channel Model

Scattered Field: In **paper III**, the holographic IRS is modeled as a continuous surface of size $L_y \times L_z$, which is placed in the yz-plane. The coordinate system is at the center of the IRS, as depicted in Fig. 3.9. Moreover, the reflection coefficient of the (y,z)th IRS point is given by $e^{j\varphi(y,z)}$, $\varphi(y,z) \in [-\pi, \pi]$. The E-field component of the spherical wave impinging on the (y,z)th IRS point is then written as

$$\mathbf{E}_i = j\sqrt{\frac{2\eta P_t G_t}{4\pi}} \frac{e^{-jkr_t(y,z)}}{r_t(y,z)} \mathbf{e}_\theta, \tag{3.33}$$

where G_t is the gain of the Tx antenna,[6] and

$$\begin{aligned} r_t(y,z) &= \sqrt{x_t^2 + (y_t - y)^2 + (z_t - z)^2} \\ &= r_t \sqrt{1 + \frac{y^2}{r_t^2} - \frac{2\sin\phi_t \sin\theta_t y}{r_t} + \frac{z^2}{r_t^2} - \frac{2\cos\theta_t z}{r_t}} \end{aligned} \tag{3.34}$$

is the distance between the Tx and the (y,z)th IRS point. Similarly, the distance between the Rx and the (y,z)th IRS point is given by

$$\begin{aligned} r_r(y,z) &= \sqrt{x_r^2 + (y_r - y)^2 + (z_r - z)^2} \\ &= r_r \sqrt{1 + \frac{y^2}{r_r^2} - \frac{2\sin\phi_r \sin\theta_r y}{r_r} + \frac{z^2}{r_r^2} - \frac{2\cos\theta_r z}{r_r}}. \end{aligned} \tag{3.35}$$

Thanks to the small physical size of THz IRSs, the amplitude variation $1/r_t(y,z)$ is marginal, and hence it can be considered as constant over the IRS. In contrast, the phase variation $kr_t(y,z)$ is significant and cannot be ignored. We therefore consider

$$\frac{e^{-jkr_t(y,z)}}{r_t(y,z)} \approx \frac{e^{-jk(r_t + \tilde{r}_t(y,z))}}{r_t}, \tag{3.36}$$

[6] We assume that G_t is constant over the angular domain as our main focus is on modeling of the IRS response.

where r_t is the radial distance of the Tx, whilst $r_t + \tilde{r}_t(y,z)$ is the Fresnel approximation of the Tx distance

$$r_t(y,z) \approx r_t + \underbrace{\frac{y^2(1-\sin^2\phi_t\sin^2\theta_t)}{2r_t} - y\sin\phi_t\sin\theta_t + \frac{z^2\sin^2\theta_t}{2r_t} - z\cos\theta_t}_{\tilde{r}_t(y,z)}. \quad (3.37)$$

Mathematically speaking, (3.37) follows from the second-order Taylor expansion $(1+x)^\alpha \approx 1 + \alpha x + \frac{1}{2}\alpha(\alpha-1)x^2$ of (3.34), while ignoring the terms $O(r_t^{-q}), q \geq 3$. By exploiting the approximate expression in (3.36), we can determine the scattered field in closed-form, as articulated in the following proposition.

Proposition 3.3.1. *Let $\varphi(y,z) = k\left(C_1y^2 + C_2y + C_3z^2 + C_4z\right)$ be the phase profile of the IRS, where C_1, C_2, C_3, and C_4 are properly selected constants. Under the physical optics approximation [61, Ch. 7], the scattered E-field at the Rx location $\mathbf{p}_r$, when the IRS is illuminated by a spherical wave originated from $\mathbf{p}_t$, is specified as*

$$\mathbf{E}_s = -\frac{L_yL_z}{\lambda}\frac{|E_i|e^{-jk(r_t+r_r)}}{r_r}\cos\phi_t\sin\theta_rS_{yz}\mathbf{e}_\theta, \quad (3.38)$$

where $|E_i| = \sqrt{\frac{2\eta P_tG_t}{4\pi r_t^2}}$ is the magnitude of the incident E-field. Also, $S_{yz} \in [0,1]$ is the normalized space factor of the IRS defined as

$$S_{yz} \triangleq \frac{\pi}{4jkL_yL_z\sqrt{a_ya_z}}\left[\mathrm{erf}\left(\sqrt{jka_y}\left(\frac{L_y}{2} - \frac{b_y}{2a_y}\right)\right) - \mathrm{erf}\left(\sqrt{jka_y}\left(-\frac{L_y}{2} - \frac{b_y}{2a_y}\right)\right)\right]$$
$$\times\left[\mathrm{erf}\left(\sqrt{jka_z}\left(\frac{L_z}{2} - \frac{b_z}{2a_z}\right)\right) - \mathrm{erf}\left(\sqrt{jka_z}\left(-\frac{L_z}{2} - \frac{b_z}{2a_z}\right)\right)\right], \quad (3.39)$$

where

$$a_y = \frac{(1-\sin^2\phi_t\sin^2\theta_t)}{2r_t} + \frac{(1-\sin^2\phi_r\sin^2\theta_r)}{2r_r} - C_1, \quad (3.40)$$
$$b_y = \sin\phi_t\sin\theta_t + \sin\phi_r\sin\theta_r + C_2, \quad (3.41)$$
$$a_z = \frac{\sin^2\theta_t}{2r_t} + \frac{\sin^2\theta_r}{2r_r} - C_3, \quad (3.42)$$
$$b_z = \cos\theta_t + \cos\theta_r + C_4. \quad (3.43)$$

Proof. See **paper III**. □

Remark 3.3.2. *In the far-field, the parallel-ray approximations*

$$\tilde{r}_t(y,z) \approx -y\sin\phi_t\sin\theta_t - z\cos\theta_t, \quad (3.44)$$
$$\tilde{r}_r(y,z) \approx -y\sin\phi_r\sin\theta_r - z\cos\theta_r \quad (3.45)$$

are used. Then, $a_y = a_z = 0$, and the space factor of the IRS reduces to [61, Ch. 11]

$$S_{yz} = \mathrm{sinc}(Y)\mathrm{sinc}(Z), \quad (3.46)$$

where $Y \triangleq kL_yb_y/2$, and $Z \triangleq kL_zb_z/2$.

Remark 3.3.3 (Physical optics)**.** *In general, characterizing the scattered E-field requires the exact solutions of Maxwell's equations under specific boundary conditions. Since this is very challenging, if not impossible, in most cases, one can resort to numerical approaches such as the method of moments [62]. In our work, we employ physical optics to obtain an approximate yet insightful expression for the scattered field in the Fresnel zone. Moreover, our analysis becomes nearly exact (i.e., by ignoring edge effects) when the IRS is configured as a perfect electric conductor (PEC). In a similar spirit, other state-of-the-art papers [63–65] invoked physical optics to derive an EM-aware channel model, yet for the far-field region.*

Path Loss Expression: From Proposition (3.3.1), the power density of the scattered field is

$$S_s = \frac{1}{2\eta}\|\mathbf{E}_s\|^2 = \left(\frac{L_y L_z}{\lambda}\right)^2 \frac{P_t G_t}{4\pi r_t^2 r_r^2} \cos\phi_t^2 \sin^2\theta_r |S_{yz}|^2, \tag{3.47}$$

where $|S_{yz}|^2$ represents the normalized beampattern of the IRS. Considering the Rx aperture $A_r = G_r\lambda^2/(4\pi)$, the received power is calculated as $P_r = S_s A_r$. Taking also into account the molecular absorption losses in THz bands yields the path loss of the Tx-IRS-Rx link

$$\overline{\mathrm{PL}} = G_t G_r \left(\frac{L_y L_z}{4\pi}\right)^2 \frac{\cos^2\phi_t \sin^2\theta_r}{r_t^2 r_r^2} e^{-\kappa_{\mathrm{abs}}(f)(r_t+r_r)} |S_{yz}|^2 = \mathrm{PL}|S_{yz}|^2, \tag{3.48}$$

where $\kappa_{\mathrm{abs}}(f)$ denotes the molecular absorption coefficient at the carrier frequency f. From (3.48), we evince that the path loss of the IRS-aided link follows the plate scattering paradigm, by which the path attenuation mainly depends on the IRS area $L_y L_z$, the reciprocal of the product of squared distances r_t^2 and r_r^2, i.e., $1/(r_t r_r)^2$, as well as the beampattern $|S_{yz}|^2$.

Signal Model: By combining (3.38) and (3.48), the baseband received signal is expressed as

$$y = \sqrt{\mathrm{PL}} e^{-jk(r_r+r_t)} S_{yz} x + \tilde{n}, \tag{3.49}$$

where $x \sim \mathcal{CN}(0, P_t)$ is the transmitted data symbol, P_t is the average power per data symbol, S_{yz} is the normalized space factor[7] of the IRS, and $\tilde{n} \sim \mathcal{CN}(0, \sigma^2)$ is the additive noise. Finally, the SNR is given by

$$\mathrm{SNR} = \frac{P_t \mathrm{PL}|S_{yz}|^2}{\sigma^2}, \tag{3.50}$$

which is maximized for $|S_{yz}|^2 = 1$.

3.3.3 Near-Field versus Far-Field Response

In this section, we thoroughly discuss the near-field channel model of Section 3.3.2 and its impact on the optimal IRS design.

[7]Note that the space factor is the continuous analogue to the array factor of antenna arrays [43].

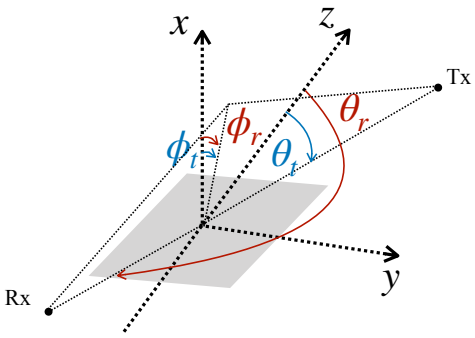

Figure 3.10: Illustration of the geometry for a holographic IRS configured as a PEC; the angles are $\phi_t = \phi_r$ and $\theta_t = \theta_r + \pi$.

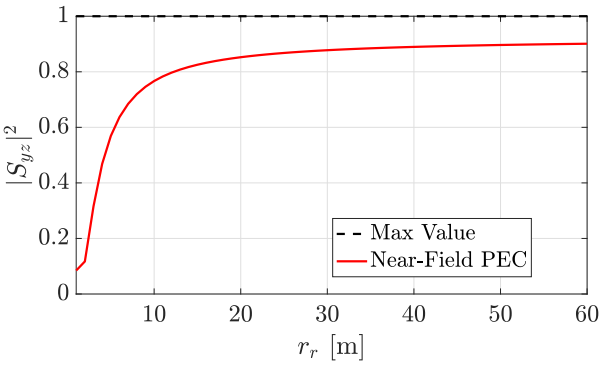

Figure 3.11: Normalized beampattern of a PEC in the Fresnel zone versus distance r_r. The parameters are: $L_y = L_z = 100\lambda$, $f = 300$ GHz, $(\theta_t, \phi_t) = (30°, 30°)$, $(\theta_r, \phi_t) = (30° + 180°, 30°)$, $r_t = 8$ m, and $1 \leq r_r \leq 60$ m.

The PEC Configuration

Assume that the IRS is configured to mimick a PEC, that is $C_1 = C_2 = C_3 = C_4 = 0$. In the far-field, (3.40)–(3.43) reduce to

$$a_y = a_z \approx 0, \tag{3.51}$$

$$b_y = \sin\phi_t \sin\theta_t + \sin\phi_r \sin\theta_r, \tag{3.52}$$

$$b_z = \cos\theta_t + \cos\theta_r. \tag{3.53}$$

As previously mentioned, the received power is maximized for $|S_{yz}|^2 = 1$, which occurs when the Tx and Rx directions are (θ_t, ϕ_t) and $(\theta_r + \pi, \phi_r)$, respectively; see Fig 3.10. In other words, the maximum of the scattered E-field is at the specular direction, as expected. Using Proposition 3.3.1, we now determine the PEC response in the Fresnel zone. Specifically, for (θ_t, ϕ_t) and $(\theta_r + \pi, \phi_r)$, we have

$$b_y = b_z = 0, \tag{3.54}$$

$$a_y = \frac{(1 - \sin^2\phi_t \sin^2\theta_t)}{2r_t} + \frac{(1 - \sin^2\phi_r \sin^2\theta_r)}{2r_r}, \tag{3.55}$$

$$a_z = \frac{\sin^2\theta_t}{2r_t} + \frac{\sin^2\theta_r}{2r_r}. \tag{3.56}$$

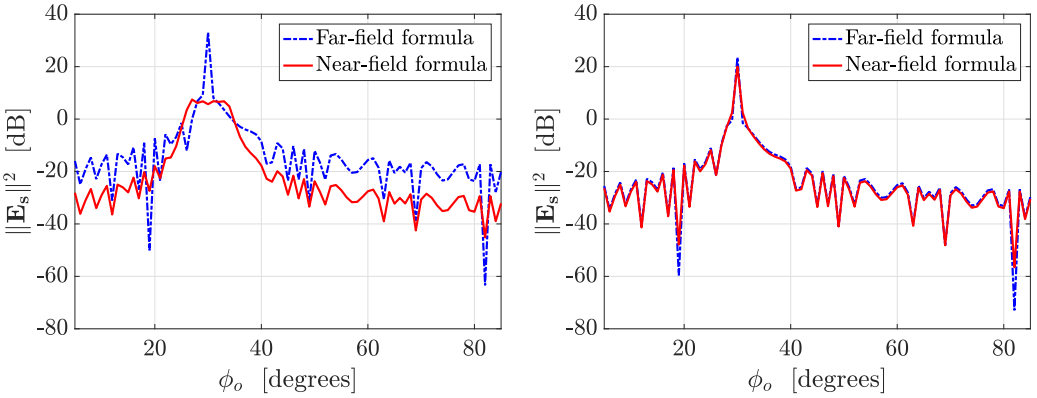

(a) $r_r = 2$ m and $r_o = 8$ m (b) $r_r = 6$ m and $r_o = 8$ m

Figure 3.12: Squared magnitude of the scattered E-field versus observation angle ϕ_o. The far-field formula uses the space factor in (3.46). The parameters are: $|E_i| = 1$, $L_y = L_z = 200\lambda$, $f = 300$ GHz, $\phi_t = 36°$, $(\theta_r, \phi_r) = (45°, 30°)$, and $(\theta_o, \phi_o) = (45°, \phi_o)$.

From Fig. 3.11, it is evident that the maximum value is not obtained when $r_t \neq r_r$. This is because the spherical wavefront of the emitted waves make S_{yz} depend on the distances r_t and r_r as well. This behavior is in sharp contrast to the far-field case, where the beampattern is a function only of the angular direction (θ, ϕ). In conclusion, the PEC configuration is not suitable for near-field communication, as it can significantly reduce the power gain, i.e., $|S_{yz}|^2 < 1$, even for distances of several meters from the IRS.

The Beamfocusing Configuration

Consider now the phase shift profile $\varphi(y, z) = k\left(C_1 y^2 + C_2 y + C_3 z^2 + C_4 z\right)$, with

$$C_1 = \frac{1 - \sin^2\phi_t \sin^2\theta_t}{2r_t} + \frac{1 - \sin^2\phi_o \sin^2\theta_o}{2r_o}, \tag{3.57}$$

$$C_2 = -\sin\phi_t \sin\theta_t - \sin\phi_o \sin\theta_o, \tag{3.58}$$

$$C_3 = \frac{\sin^2\theta_t}{2r_t} + \frac{\sin^2\theta_o}{2r_o}, \tag{3.59}$$

$$C_4 = -\cos\theta_t - \cos\theta_o, \tag{3.60}$$

where $(r_o \cos\phi_o \sin\theta_o, r_o \sin\phi_o \sin\theta_o, r_o \cos\theta_o)$ is an arbitrary observation position. This phase shift profile focuses the signal toward the Rx point. More particularly, (3.40)–(3.43) reduce to

$$a_y = \frac{1 - \sin^2\phi_r \sin^2\theta_r}{2r_r} - \frac{1 - \sin^2\phi_o \sin^2\theta_o}{2r_o}, \tag{3.61}$$

$$b_y = \sin\phi_r \sin\theta_r - \sin\phi_o \sin\theta_o, \tag{3.62}$$

$$a_z = \frac{\sin^2\theta_r}{2r_r} - \frac{\sin^2\theta_o}{2r_o}, \tag{3.63}$$

$$b_z = \cos\theta_r - \cos\theta_o. \tag{3.64}$$

Consequently, $S_{yz} = 1$ for $(r_o, \theta_o, \phi_o) = (r_r, \theta_r, \phi_r)$, yielding the desired result. We next plot the squared magnitude of the scattered E-field in Fig. 3.12. As observed

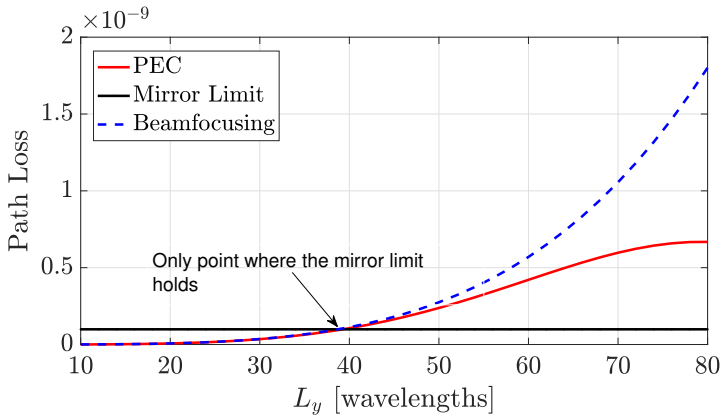

Figure 3.13: Path loss of different IRS configurations versus dimension L_y. The parameters are: $L_y = L_z$, $f = 300$ GHz, $(\theta_t, \phi_t) = (30°, 30°)$, $(\theta_r, \phi_t) = (30° + 180°, 30°)$, $r_t = 2$ m, and $r_r = 6$ m.

from Fig. 3.12(a), there is a discrepancy between the near and far scattered fields for $r_o \neq r_r$, which implies that the scattering from an electrically large IRS can not be accurately described by the far-field model.[8] Lastly, it is worth stressing that the near-field space factor in (3.39) coincides with its far-field counterpart (3.46) for either an electrically small IRS or relatively large distances r_r and r_o, i.e., Fig. 3.12(b).

3.3.4 Comparison with Anomalous Mirror

In the related literature [66–69], there has been a debate on whether the near-field path loss is proportional to $1/(r_t + r_r)^2$, which represents the specular reflection paradigm. Since specular reflection occurs only for an infinite flat surface, this power law is referred to as mirror limit. However, we have shown that the near-field path loss is PL $\propto 1/(r_t r_r)^2$ in general. Furthermore, beamfocusing is the optimal IRS configuration making the Rx power scale quadratically with the IRS area $L_y L_z$. As a result, the "mirror limit" configuration is suboptimal for unicast transmissions, and can be only useful in broadcasting scenarios [45]. To see this, consider the following options:

- PEC, where the path loss is calculated using (3.48).
- Beamfocuing, where the path loss is $\left(\frac{L_y L_z}{4\pi r_t r_r}\right)^2$.
- Mirror-limit, where the path loss is $\left(\frac{\lambda}{4\pi(r_t+r_r)}\right)^2$.

The results are depicted in Fig. 3.13. First, we observe that the PEC and beamfocusing configurations act the same for an electrically small IRS since the spherical wavefront can be neglected. However, as the IRS size increases, the PEC reduces the received power, i.e., $S_{yz} < 1$. More importantly, the path loss of the IRS coincides with that of the mirror only for a specific IRS size, and do not make the power scale as $(L_y L_z)^2$. In conclusion, the IRS should not be treated as an anomalous mirror either in the far-field or Fresnel zone.

[8] Recall that the spherical wavefront leads to a distance-dependent beampattern.

3.3.5 Discretizing a Holographic IRS

It might be difficut to implement a holographic IRS in practice. For this reason, the continuous surface of size $L_y \times L_z$ can be approximated by a planar structure of $N_1 = L_y/(d_y + \tilde{L}_y)$ and $N_2 = L_z/(d_z + \tilde{L}_z)$ reflecting elements, where $\tilde{L}_y \times \tilde{L}_z$ is the area of each element, whilst d_y and d_z are the inter-element spacings along the y and z directions, respectively. In **paper III**, we have shown that the discrete version of the space factor (3.39) can be expressed as

$$S_{yz}^{d} = \frac{\sum_{n=-\frac{N_1}{2}}^{\frac{N_1}{2}-1} e^{-jk\left((n(\tilde{L}_y+d_y))^2 a_y - n(\tilde{L}_y+d_y) b_y\right)}}{N_1} \times \frac{\sum_{m=-\frac{N_2}{2}}^{\frac{N_2}{2}-1} e^{-jk\left((m(\tilde{L}_z+d_z))^2 a_z - m(\tilde{L}_z+d_z) b_z\right)}}{N_2}, \tag{3.65}$$

with $S_{yz}^{d} \approx S_{yz}$ for $d_y = d_z = 0$, i.e., negligible inter-element spacing. Furthermore, the discretized IRS attains the same power gain as its holographic counterpart for $d_y = d_z = 0$.[9]

3.3.6 Summary

In **paper III**, we studied holographic IRSs at THz frequencies. In particular:

- We determined the scattered E-field from a holographic IRS in the Fresnel zone by leveraging physical optics. This enabled us to characterize the path loss of IRS-assisted propagation analytically. Our channel model accounts for the spherical wavefront of the radiated EM waves and, hence, reveals the beamfocusing capabilities of electrically large IRSs.

- Capitilizing on the derived channel model, we showed that the PEC configuration is suboptimal in the near-field as it can significantly reduce the power gian. Thus, the IRS should be configured to perform beamfocusing. This new paradigm shift in IRS design requires accurate localization of the Tx and Rx, which is an interersting research problem per se.

- We demonstrated that an electircally large IRS does not act as an anomalous mirror in general. Specifically, the path loss degenerates into the mirror-limit only for a particular IRS size. Besides, the mirror-limit configuration does not make the power scale quadratically with the IRS area, and hence can not be exploited to mitigate the severe path loss of the IRS-aided link.

- We discussed how a holographic IRS can be discretized to facilitate efficient hardware implementation. Specifically, a necessary condition is to have a sub-wavelength spacing between reflecting elements. The mutual coupling effects that kick in for ultra-dense IRSs play a key role in the overall performance, and hence their investigation is left for future work. The work in [70] can serve as a good starting point.

[9] The study of mutual coupling between adjacent reflecting elements is important and, hence, is left for future work.

3.4 Wideband Considerations

The abundant spectrum available at THz frequencies is widely deemed the key resource for attaining data rates in the order of terabits-per-second. However, IRS-aided wideband THz systems pose several new challenges. One of these challenges involves dealing with the spatial-wideband effect, which renders the channel response frequency-selective even for LoS propagation. In this section, we investigate the performance of IRS-assisted THz communication under the spatial-wideband effect. Note that existing works on THz IRSs (e.g., [71–73] and references therein) ignore the spatial-wideband effect.

3.4.1 Channel Model with Spatial-Wideband Effects

In **paper IV**, we considered a discrete IRS in the xy-plane. Specifically, the IRS consists of $N = N_1 \times N_2$ reflecting elements of size $L_x \times L_y$ each. The origin of the coordinate system is placed at the center of the IRS, and the position of each reflecting element is measured from its center. Then, assuming negligible inter-element spacing, the position vector of the (n,m)th element is $\mathbf{p}_{n,m} = ((n-1/2)L_x, (m-1/2)L_y, 0)$, for $n = -\frac{N_1}{2}, \ldots, \frac{N_1}{2}-1$ and $m = -\frac{N_2}{2}, \ldots, \frac{N_2}{2}-1$. The Tx distance (3.10) and Rx distance (3.11) are recast, respectively, as

$$r_t(n,m) = r_t \left(1 + \frac{\left((n-\frac{1}{2})L_x\right)^2}{r_t^2} - \frac{2\cos\phi_t \sin\theta_t (n-\frac{1}{2})L_x}{r_t} + \frac{\left((m-\frac{1}{2})L_y\right)^2}{r_t^2} - \frac{2\sin\phi_t \sin\theta_t (m-\frac{1}{2})L_y}{r_t} \right)^{1/2} \tag{3.66}$$

and

$$r_r(n,m) = r_r \left(1 + \frac{\left((n-\frac{1}{2})L_x\right)^2}{r_r^2} - \frac{2\cos\phi_r \sin\theta_r (n-\frac{1}{2})L_x}{r_r} + \frac{\left((m-\frac{1}{2})L_y\right)^2}{r_r^2} - \frac{2\sin\phi_r \sin\theta_r (m-\frac{1}{2})L_y}{r_r} \right)^{1/2}. \tag{3.67}$$

In the wideband case, the received baseband signal (3.2) at time t is expressed as

$$\begin{aligned} y(t) &= \sum_{n=-\frac{N_1}{2}}^{\frac{N_1}{2}-1} \sum_{m=-\frac{N_2}{2}}^{\frac{N_2}{2}-1} h_{n,m} e^{j\varphi_{n,m}} x(t-\tau_{n,m}) + \tilde{n}(t) \\ &= \sum_{n=-\frac{N_1}{2}}^{\frac{N_1}{2}-1} \sum_{m=-\frac{N_2}{2}}^{\frac{N_2}{2}-1} \sqrt{\mathrm{PL}_{n,m}} e^{-j2\pi f_c \tau_{n,m}} e^{j\varphi_{n,m}} x(t-\tau_{n,m}) + \tilde{n}(t), \end{aligned} \tag{3.68}$$

where f_c is the carrier frequency, $\tau_{n,m} \triangleq (r_t(n,m) + r_r(n,m))/c$ is the propagation delay of the signal reflected by the (n,m)th IRS element, and c is the speed of light.

The path loss $\mathrm{PL}_{n,m}$ is specified according to (3.7). Taking the continuous-time Fourier transform of (3.68) gives

$$Y(f) \approx \sqrt{\mathrm{PL}} \underbrace{\sum_{n=-\frac{N_1}{2}}^{\frac{N_1}{2}-1} \sum_{m=-\frac{N_2}{2}}^{\frac{N_2}{2}-1} e^{-j2\pi(f_c+f)\tau_{n,m}} e^{j\varphi_{n,m}}}_{H_{\text{eff}}(f)} X(f) + \tilde{N}(f), \tag{3.69}$$

where the approximation follows from $\mathrm{PL}_{n,m} \approx \mathrm{PL}$ thanks to the small physical size of THz IRSs, PL is the path loss calculated using the radial distances r_t and r_r, $\mathcal{F}\{y(t)\} = Y(f)$, $\mathcal{F}\{x(t)\} = X(f)$, $\mathcal{F}\{\tilde{n}(t)\} = \tilde{N}(f)$, and $H_{\text{eff}}(f)$ is the effective channel accounting for the phase shifts. Note that $H_{\text{eff}}(f)$ is frequency-dependent under LoS propagation because of the *spatial-wideband* effect. Next, consider OFDM modulation with S subcarriers for a signal bandwidth B. The subcarrier spacing is $\Delta\mathrm{B} = B/S$, whilst the baseband frequency of the sth subcarrier is specified as $f_s = \left(s - \frac{S-1}{2}\right)\Delta\mathrm{B}$, for $s = 0, \ldots, S-1$. Hence, the received signal at the sth OFDM subcarrier is given by

$$Y(f_s) = \sqrt{\mathrm{PL}} H_{\text{eff}}(f_s) X(f_s) + \tilde{N}(f_s), \tag{3.70}$$

where $X(f_s) \sim \mathcal{CN}(0, P_t/S)$ is the transmitted data symbol with average power P_t/S, and $\tilde{N}(f_s) \sim \mathcal{CN}(0, \sigma^2\Delta\mathrm{B})$ is the additive noise at each subcarrier.

Remark 3.4.1. *Let $T_s = 1/B$ denote the symbol period. For $\tau_{n,m} \ll T_s, \forall n, m$, we have the approximation $x(t - \tau_{n,m}) \approx x(t)$. This yields a spatially narrowband channel under LoS propagation.*

3.4.2 Performance Analysis

Power Gain

From (3.70), the SNR at the sth OFDM subcarrier is

$$\mathrm{SNR}_s = \frac{P_t \mathrm{PL} |H_{\text{eff}}|^2}{B\sigma^2} = \frac{N^2 G_s P_t \mathrm{PL}}{B\sigma^2}, \tag{3.71}$$

where $G_s \triangleq |H_{\text{eff}}|^2/N^2 \in [0, 1]$ is the normalized power gain. Under frequency-dependent beamfocusing, i.e., $\varphi_{n,m}(f_s) = 2\pi(f_c + f_s)\tau_{n,m}$, $G_s = 1$ and a power gain of N^2 is achived over all OFDM subcarriers. However, standard IRS designs[10] facilitate narrowband beamfocusing, where the phase shift induced by the (n, m)th element is $\varphi_{n,m} = 2\pi f_c \tau_{n,m}$. In this case, the normalized power gain reduces to

$$G_s = \frac{1}{N_1^2 N_2^2} \left| \sum_{n=-\frac{N_1}{2}}^{\frac{N_1}{2}-1} \sum_{m=-\frac{N_2}{2}}^{\frac{N_2}{2}-1} e^{-j2\pi f_s \frac{r_t(n,m) + r_r(n,m)}{c}} \right|^2, \tag{3.72}$$

[10]Each IRS element is typically modeled as a transmission line [74], where the argument of the reflection coefficient does not scale linearly with the frequency of the incident wave.

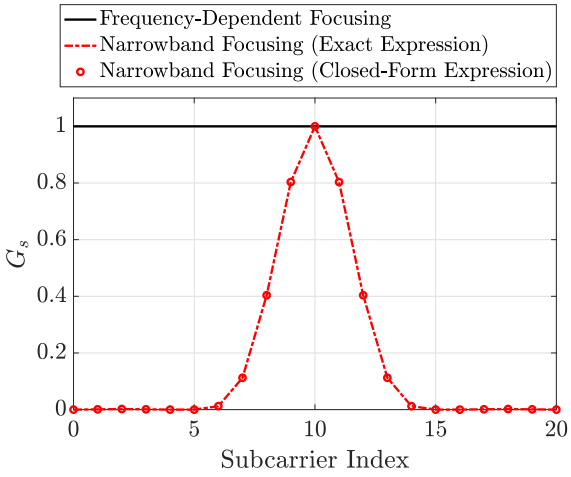

Figure 3.14: Normalized power gain for an 80×80-element IRS, $B = 20$ GHz, $f_c = 300$ GHz, $(r_t, \theta_t, \phi_t) = (1, \pi/3, \pi/5)$, and $(r_r, \theta_r, \phi_r) = (5, \pi/4, \pi/3)$.

which yields $G_s < 1$ for $f_s > 0$. Consequently, it is important to study the power gain under narrowband beamfocusing. To this direction, in **paper IV**, we derived a closed-form expression for the decrease in the power gain, which relies on the Fresnel approximation of the Tx and Rx distances r_t and r_r, respectively. From Fig. 3.14, the excellent match between the exact formula (3.72) and the derived approximate expression is verified. Most importantly, we observe that the normalized power gain G_s tends to zero at the subcarriers that are far from the carrier frequency f_c, hence creating severe power imbalance among different OFDM subcarriers due to beam squint.

Achievable Rate

Rate versus IRS size: By availing of the closed-form formula, we can show that the average power gain $N^2\bar{G}$, where $\bar{G} = \sum_{s=0}^{S-1} G_s/S$, can be bounded as $N^2\bar{G} \leq G_{\max}$ for some $G_{\max} > 0$. Then, we can write for the achievable rate

$$\begin{aligned} R = \sum_{s=0}^{S-1} \frac{B}{S} \log_2 \left(1 + \frac{N^2 G_s P_t \mathrm{PL}}{B\sigma^2}\right) &\overset{(a)}{\leq} B \log_2 \left(1 + \frac{1}{S} \sum_{s=0}^{S-1} \frac{N^2 G_s P_t \mathrm{PL}}{B\sigma^2}\right) \\ &= B \log_2 \left(1 + \frac{N^2 \bar{G} P_t \mathrm{PL}}{B\sigma^2}\right) \\ &\leq B \log_2 \left(1 + \frac{G_{\max} P_t \mathrm{PL}}{B\sigma^2}\right), \end{aligned} \tag{3.73}$$

where (a) follows from the inequality of arithmetic and geometric means. According to (3.73), the achievable rate R does not grow without bound as the number N of IRS elements grows. This result comes in sharp contrast to the spatially narrowband case, where increasing N would increase R as well. Practically speaking, this means that the performance degradation due to beam squint cannot be effectively mitigated by inceasing the number of IRS elements.

Beamfocusing Optimization: To improve the system performance, we resort to a

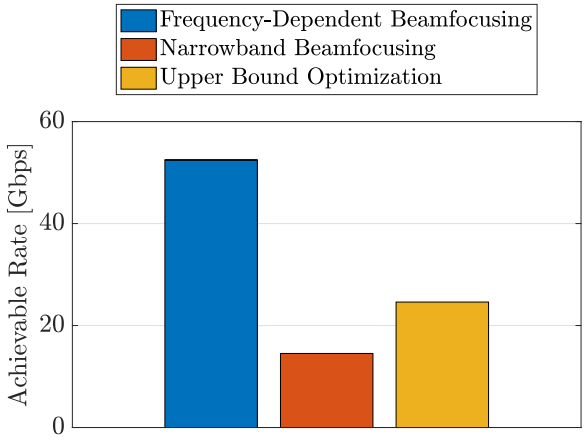

Figure 3.15: Achievable rate for an 80×80-element IRS, $B = 20$ GHz, $f_c = 300$ GHz, $S = 20$, $(r_t, \theta_t, \phi_t) = (1, \pi/3, \pi/5)$, and $(r_r, \theta_r, \phi_r) = (5, \pi/4, \pi/3)$.

more sophisticated phase shift design than narrowband beamfocusing. Specifically, in **paper IV**, we formulated an upper bound optimization problem,[11] which serves as a benchmark to assess the impact of the spatial-wideband effect on the achievable rate. In Fig. 3.15, the achievable rates of the frequency-dependent beamfocusing, narrowband beamfocusing, and upper bound optimization approach are 52.48 Gbps, 14.52 Gbps, and 24.61 Gbps, respectively. As evinced, narrowband beamfocusing performs very poorly and results in a 72.3% rate loss. Moreover, the upper bound optimization approach performs better, but it still yields a much smaller rate than frequency-dependent beamfocusing. This numerical experiment emphasizes the need of a wideband IRS implementation based on TTD-like elements [77].

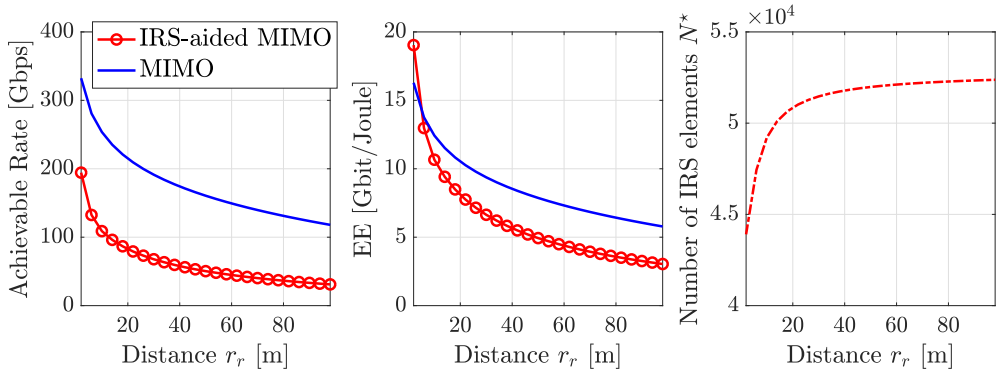

Figure 3.16: Results under narrowband beamfocusing for $\alpha = 2$ and a fixed IRS location at (0,0,0). In the MIMO system, $N_t = 100$ and $N_r = 100$. The other parameters are $G_t = G_r = 20$ dBi, $P_t = 10$ dBm, $P_{\text{PS}} = 42$ mW and $P_{\text{PA}} = 60$ mW [56], $\sigma^2 = -174$ dBm/Hz, $B = 20$ GHz, $S = 20$, $f_c = 300$ GHz, $L_x = L_y = \lambda/2$, $\mathbf{p}_t = (0.8, -0.8, 0.2)$, and $\mathbf{p}_r = (0.8, r_r, 0.2)$.

Energy Efficiency

In Section 3.2.4, we demonstrated that an IRS can improve the EE efficiency of THz MIMO, yet in the absence of beam squint. In **paper IV**, we extended the previous analysis to the wideband case. As observed from Fig. 3.16, the EE efficiency

[11] This is a well-established optimization approach in the related literature, e.g., [75, 76].

gains cannot be attained through narrowband beamfocusing because of the detrimental impact of beam squint. As a result, beam squint mitigation is of paramount importance to IRS-assisted wideband THz communications.

3.4.3 Summary

In **paper IV**, we studied, for the first time, the spatial-wideband effect in IRS-aided THz communications. In particular:

- We introduced a spherical wave channel model that accounts for the spatial-wideband effect.
- Building on the proposed channel model, we analyzed the power gain, achievable rate, and EE under narrowband beamfocusing. Specifically, our analysis shows that narrowband beamfocusing leads to severe performance degradation for large transmission bandwidths.
- The key conclusion drawn from our study is that conventional IRS designs cannot efficiently support wideband THz communication due to beam squint. Therefore, an interesting avenue for future work is how to implement an IRS with a broadband response. Inspired by wideband reflectarrays, frequency selective surfaces [77] might be promising.

4 Concluding Remarks

In this thesis, we studied THz communications from a physical layer perspective. Specifically, we first focused on massive MIMO, which is widely deemed a key enabler of 5G-and-beyond wireless networks. Unlike mmWave antenna systems, THz massive MIMO will incorporate an unprecedented number of BS antennas and will utilize extremely large bandwidths to facilitate terabit-per-second communications. It therefore poses multiple new challenges, including the hardware-friendly implementation of massive antenna arrays, low-overhead acquisition of CSI, and efficient beamforming in the face of beam squint, to name but a few. In this thesis, we sought to provide a solution to the channel estimation and combining problems under the constraint of a hybrid analog-digital antenna array at the BS. Our contribution was to devise a novel hybrid combiner and channel estimator suitable for ultra-wideband operation.

Looking beyond conventional antenna arrays, we thoroughly explored the concept of IRSs as well. In particular, we focused on the near-field region, and analyzed the channel modeling and phase shift design of electrically large IRSs. More importantly, we leveraged tools of EM theory to analytically characterize the near-field response of holographic IRSs, which constitute the asymptotic form of reconfigurable surfaces offering ultra-high power gains. We believe the research conducted in this thesis has shed light on the fundamentals of IRSs at THz frequency bands. The contributions made in this thesis are only an initial foray into the immersive world of EM metasurfaces and wavefront manipulation. For future research, there are several promising avenues, such as the modeling of mutual coupling in space-constrained IRSs, super-directivity, transmission line models for broadband IRS designs, and wireless power transfer in the near-field zone.

Paper I

Channel Estimation and Hybrid Combining for Wideband Terahertz Massive MIMO Systems

Konstantinos Dovelos, *Graduate Student Member, IEEE*, Michail Matthaiou, *Senior Member, IEEE*, Hien Quoc Ngo, *Senior Member, IEEE*, and Boris Bellalta, *Senior Member, IEEE*

***Abstract*—Terahertz (THz) communication is widely considered as a key enabler for future 6G wireless systems. However, THz links are subject to high propagation losses and inter-symbol interference due to the frequency selectivity of the channel. Massive multiple-input multiple-output (MIMO) along with orthogonal frequency division multiplexing (OFDM) can be used to deal with these problems. Nevertheless, when the propagation delay across the base station (BS) antenna array exceeds the symbol period, the spatial response of the BS array varies over the OFDM subcarriers. This phenomenon, known as beam squint, renders narrowband combining approaches ineffective. Additionally, channel estimation becomes challenging in the absence of combining gain during the training stage. In this work, we address the channel estimation and hybrid combining problems in wideband THz massive MIMO with uniform planar arrays. Specifically, we first introduce a low-complexity beam squint mitigation scheme based on true-time-delay. Next, we propose a novel variant of the popular orthogonal matching pursuit (OMP) algorithm to accurately estimate the channel with low training overhead. Our channel estimation and hybrid combining schemes are analyzed both theoretically and numerically. Moreover, the proposed schemes are extended to the multi-antenna user case. Simulation results are provided showcasing the performance gains offered by our design compared to standard narrowband combining and OMP-based channel estimation.**

***Index Terms*—Beam squint effect, compressive channel estimation, hybrid combining, massive MIMO, planar antenna arrays, wideband THz communication.**

I. Introduction

Spectrum scarcity is the main bottleneck of current wireless communication systems. As a result, new frequency bands and signal processing techniques are required to deal with the spectrum gridlock. In view of the enormous bandwidth available at terahertz (THz) frequencies, communication over the THz band is deemed a key technology for future 6G wireless systems [1]. Specifically, the THz band, spanning from 0.1 to 10 THz, offers much larger bandwidths than the millimeter wave (mmWave) band. For example, the licensed bandwidth in the mmWave band is usually up to 7 GHz whilst that in the THz band will be at least 10 GHz [2]. According to the Friis transmission formula, though, the path loss becomes more severe as the frequency increases, and thus THz signals undergo higher attenuation than their mmWave and microwave counterparts. However, thanks to the short wavelength of THz signals, a very large number of antennas can tightly be packed into a small area to form a massive multiple-input multiple-output (MIMO) transceiver, hence effectively compensating for the propagation losses by means of sharp beamforming [3]. Therefore, THz massive MIMO is expected to enable ultra-high-speed communication systems, such as terabit wireless personal/local area networks and femtocells [4].

Despite the promising performance gains of THz massive MIMO systems, the wideband transmissions in conjunction with the large array aperture might give rise to *spatial-frequency wideband (SFW)* effects [5]. In this case, the channel response becomes frequency-selective not only because of the delay spread of the multi-path channel, but also due to the large propagation delay across the array aperture [6]. As a result, the response of the BS array can be frequency-dependent also in a line-of-sight (LoS) scenario. When orthogonal frequency division multiplexing (OFDM) modulation is employed to combat inter-symbol interference, the spatial-wideband effect renders the direction-of-arrival (DoA) and direction-of-departure (DoD) of the signals to vary over the subcarriers. This phenomenon, termed *beam squint*, calls for frequency-dependent beamforming/combining, which is not available in a typical hybrid array architecture of THz massive MIMO. More particularly, narrowband beamforming/combining approaches can substantially reduce the array gain across the OFDM subcarriers, hence leading to performance degradation [7]. Consequently, beam squint compensation is of paramount importance for THz massive MIMO-OFDM systems.

Since accurate channel state information (CSI) is essential to effectively implement combining and/or beam squint mitigation, channel estimation under SFW effects is another important problem to address. Specifically, in the absence of combining gain during channel estimation, the detection of the paths present in the channel becomes challenging in the low signal-to-noise ratio (SNR) regime. Additionally, due to the massive number of BS antennas and the limited number of radio frequency (RF) chains in a hybrid array architecture, the channel estimation overhead becomes excessively large even for single-antenna users under standard approaches, such as the least squares (LS) method. In conclusion, THz massive

Manuscript received July 7, 2020; revised November 20, 2020, and February 12, 2021; accepted March 1, 2021. The work of K. Dovelos and B. Bellalta was supported by grants WINDMAL PGC2018-099959-B-I00 (MCIU/AEI/FEDER,UE), and SGR017-1188 (AGAUR). The work of M. Matthaiou was supported by the EPSRC, U.K., under Grant EP/P000673/1 and by a research grant from the Department for the Economy Northern Ireland under the US-Ireland R&D Partnership Programme. The work of H. Q. Ngo was supported by the U.K. Research and Innovation Future Leaders Fellowships under Grant MR/S017666/1.

K. Dovelos and B. Bellalta are with the Department of Information and Communication Technologies, Pompeu Fabra University, Barcelona, Spain (e-mail: konstantinos.dovelos@upf.edu; boris.bellalta@upf.edu).

M. Matthaiou and H. Q. Ngo are with the Institute of Electronics, Communications and Information Technology (ECIT), Queen's University Belfast, Belfast, U.K. (e-mail: m.matthaiou@qub.ac.uk; hien.ngo@qub.ac.uk).

MIMO brings new challenges in the signal processing design, and calls for carefully tailored solutions that take into account the unique propagation characteristics in THz bands.

A. Prior Work

In this section, we review prior work on channel estimation and hybrid beamforming in wideband mmWave/THz systems.

The authors in [8] proposed a novel single-carrier transmission scheme for THz massive MIMO, which utilizes minimum mean-square error precoding and detection. Nevertheless, a narrowband antenna aray model was considered, and hence the SFW effect was ignored. A stream of recent papers on wideband mmWave MIMO-OFDM systems (see [9]–[12], and references therein) proposed methods to jointly optimize the analog combiner and the digital precoder in order to maximize the achievable rate under the beam squint effect. In a similar spirit, [13] and [14] proposed a new analog beamforming codebook with wider beams to avoid the array gain degradation due to beam squint. These methods can enhance the achievable rate when the beam squint effect is mild. However, their performance becomes poor in THz MIMO systems as the signal bandwidth and number of BS antennas are much larger than their mmWave counterparts [17]. To this end, [15] proposed a wideband codebook for beam training for uniform linear arrays (ULAs) using true-time-delay (TTD) [16]. Nevertheless, this design is limited to ULAs and beam alignment without explicitely estimating the channel. From the relevant literature on hybrid beamforming, we distinguish [17], which proposed a TTD-based hybrid beamformer for THz massive MIMO, yet assuming ULAs and perfect CSI.

Despite the importance of channel estimation, there are only few recent works in the literature investigating the channel estimation problem under the spatial-wideband effect. More particularly, the seminal paper [5] introduced the SFW for mmWave massive MIMO systems, and proposed a channel estimation algorithm by capitalizing on the asymptotic properties of SFW channels. However, the proposed algorithm relies on multiplying the channel of an N-element uniform linear array by an N-point discrete Fourier transform (DFT) matrix, and hence entails high training overhead when the number of RF chains is much smaller than the number of BS antennas. In a similar spirit, [18] employed the orthogonal matching pursuit (OMP) algorithm along with an energy-focusing preprocessing step to estimate the SFW channel, while minimizing the power leakage effect. Finally, [19] leveraged tools from compressive sensing (CS) theory to tackle the channel estimation problem in frequency-selective multiuser mmWave MIMO systems but in the absence of the spatial-wideband effect.

B. Contributions

In this paper, we address the channel estimation and hybrid combining problems in wideband THz MIMO. To this end, we assume OFDM modulation, which is the most popular transmission scheme over frequency-selective channels. The main contributions of the paper are summarized as follows:

- We model the SFW effect in THz MIMO-OFDM systems with a uniform planar array (UPA) at the BS. Note that prior studies (e.g., [20], [21]) on mmWave/THz communication with UPAs ignore the SFW effect. We next show that frequency-flat combining leads to substantial performance losses due to the severe beam squint effect occuring across OFDM subcarriers, and propose a beam squint compensation strategy using TTD [22] and virtual array partition. The scope of the virtual array partition is to reduce the number of TTD elements needed to effectively mitigate beam squint. To this end, we derive the wideband combiner expression for a rectangular planar array, and establish its near-optimal performance with respect to fully-digital combining analytically, as well as through computer simulations.
- We propose a solution to the channel estimation problem under the SFW effect. Specifically, by availing of the channel sparsity in the angular domain, we first adopt a sparse representation of the THz channel, and formulate the channel estimation problem as a CS problem. We then propose a solution based on the OMP algorithm, which is one of the most common and simple greedy CS methods. Contrary to existing works, we employ a *wideband* dictionary and show that channels across different OFDM subcarriers share a common support. This enables us to apply a variant of the simultaneous OMP algorithm, coined as generalized simultaneous OMP (GSOMP), which exploits the information of multiple subcarriers to increase the probability of successfully recovering the common support. We also evaluate the computational complexity of the GSOMP to showcase its efficiency with respect to the OMP. Numerical results show that the propounded estimator outperforms the OMP-based estimator in the low and moderate SNR regimes, whilst achieving the same accuracy in the high SNR regime.
- We analyze the mean-square error of the GSOMP scheme by providing the Cramér-Rao lower bound (CRLB). Moreover, we calculate the average achievable rate assuming imperfect channel gain knowledge at the BS. We then show numerically that when the angle quantization error involved in the sparse channel representation is negligible, the performance of the GSOMP-based estimator is very close to the CRLB. Additionally, the average achievable rate approaches that of the perfect channel knowledge case at moderate and high SNR values, hence corroborating the good performance of our design. Finally, we extend our analysis to the case of a multi-antenna user, and discuss the benefits of deploying multiple antennas at the user side.

The rest of this paper is organized as follows: Section II introduces the system and channel models. Section III describes the hybrid combining problem under the beam squint effect, and presents the proposed combining scheme. Section IV formulates the channel estimation problem, introduces the standard estimation methods, and explains the propounded algorithm for estimating the SFW channel. Section V extends the analysis to the multi-antenna user case. Section VI is devoted to numerical simulations. Finally, Section VII summarizes the main conclusions derived in this work.

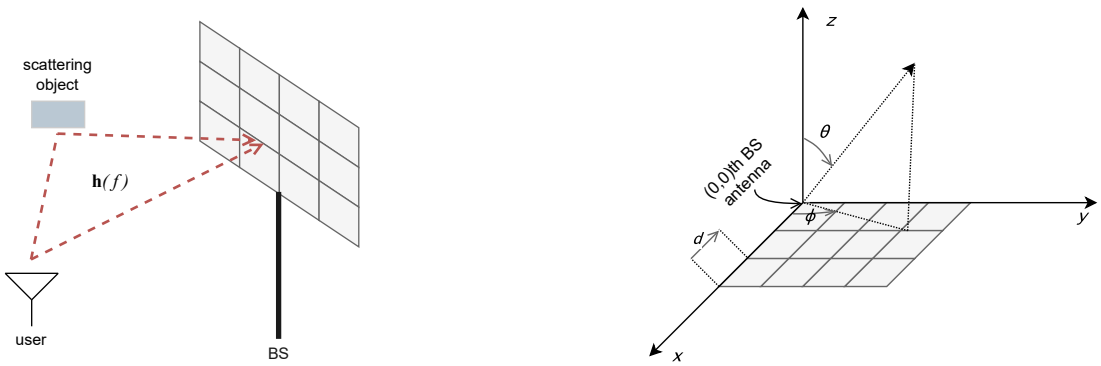

(a) Uplink setup

(b) Array geometry

Fig. 1: Illustration of the BS antenna array and its geometry considered in the system model.

Notation: Throughout the paper, $D_N(x) = \frac{\sin(Nx/2)}{N\sin(x/2)}$ is the Dirichlet sinc function; $\mathbf{A}$ is a matrix; $\mathbf{a}$ is a vector; a is a scalar; $\mathbf{A}^\dagger$, $\mathbf{A}^H$, and $\mathbf{A}^T$ are the pseudoinverse, conjugate transpose, and transpose of $\mathbf{A}$, respectively; $\mathbf{A}(i)$ is the ith column of matrix $\mathbf{A}$; $\mathbf{A}(\mathcal{I})$ is the submatrix containing the columns of $\mathbf{A}$ given by the indices set $\mathcal{I}$; $|\mathcal{I}|$ is the cardinality of set $\mathcal{I}$; $\text{tr}\{\mathbf{A}\}$ is the trace of $\mathbf{A}$; $\text{blkdiag}(\mathbf{A}_1, \ldots, \mathbf{A}_n)$ is the block diagonal matrix; $[\mathbf{A}]_{n,m}$ is the (n,m)th element of matrix $\mathbf{A}$; $\mathcal{F}\{\cdot\}$ denotes the continuous-time Fourier transform; $*$ denotes convolution; $\text{Re}\{\cdot\}$ is the real part of a complex variable; $\mathbf{1}_{N\times M}$ is the $N \times M$ matrix with unit entries; $\mathbf{I}_N$ is the $N \times N$ identity matrix; $[\mathbf{v}]_n$ is the nth entry of vector $\mathbf{v}$; $\text{supp}(\mathbf{v}) = \{n : [\mathbf{v}]_n \neq 0\}$ is the support of $\mathbf{v}$; $\otimes$ denotes the Kronecker product; $\odot$ is the element-wise product; $\|\mathbf{a}\|_1$ and $\|\mathbf{a}\|_2$ are the l_1-norm and l_2-norm of vector $\mathbf{a}$, respectively; $\mathbb{E}\{\cdot\}$ is expectation; and $\mathcal{CN}(\boldsymbol{\mu}, \mathbf{R})$ is a complex Gaussian vector with mean $\boldsymbol{\mu}$ and covariance matrix $\mathbf{R}$.

TABLE I
MAIN NOTATION USED IN THE SYSTEM MODEL

Notation	Description
S	Number of subcarriers
f_s	Frequency of the sth subcarrier
B	Total signal bandwidth
L	Number of NLoS paths
$\alpha_l(f)$	Frequency-selective attenuation of the lth path
τ_l	ToA of the lth path
(ϕ_l, θ_l)	DoA of the lth path
$\tau_{l,nm}$	Time delay to the (n,m)th BS antenna over the lth path
$\tau_{nm}(\phi_l, \theta_l)$	Time delay from the $(0,0)$th to the (n,m)th BS antenna
$\mathtt{x}(t)$	Baseband-equivalent of transmitted signal
$x(f)$	Fourier transform of $\mathtt{x}(t)$
$\mathtt{x}_l(t)$	Distorted version of $\mathtt{x}(t)$ over the lth path
$\tilde{r}_{nm}(t)$	Passband signal received by the (n,m)th BS antenna
$\mathtt{r}_{nm}(t)$	Baseband-equivalent of $\tilde{r}_{nm}(t)$
$r_{nm}(f)$	Fourier transform of $\mathtt{r}_{nm}(t)$
d	Antenna spacing
f_c	Carrier frequency
c	Speed of light
k_{abs}	Molecular absorption coefficient
$\mathtt{D}$	Distance between the BS and the user
$\Gamma_l(f)$	Reflection coefficient of the lth NLoS path

II. SYSTEM MODEL

Consider the uplink of a THz massive MIMO system where the BS is equipped with an $N \times M$-element UPA, and serves a single-antenna user as depicted in Fig 1(a); the multi-antenna user case is investigated in Section V. The total number of BS antennas is $N_B = NM$, and the baseband frequency response of the uplink channel is denoted by $\mathbf{h}(f) \in \mathbb{C}^{N_B \times 1}$. In the sequel, we present the channel and hybrid transceiver models used in this work.

A. THz Channel Model with Spatial-Wideband Effects

Due to limited scattering in THz bands, the propagation channel is represented by a ray-based model of $L + 1$ rays [21], [23]. Hereafter, we assume that the 0th ray corresponds to the LoS path, while the remaining $l = 1, \ldots, L$, rays are non-line-of-sight (NLoS) paths. Specifically, each path $l = 0, \ldots, L$, is characterized by its frequency-selective path attenuation $\alpha_l(f)$, time-of-arrival (ToA) τ_l, and DoA (ϕ_l, θ_l), where $\phi_l \in [-\pi, \pi]$ and $\theta_l \in [-\frac{\pi}{2}, \frac{\pi}{2}]$ are the azimuth and polar angles, respectively. In the far-field region[1] of the BS antenna array, the total delay between the user and the (n,m)th BS antenna through the lth path, $\tau_{l,nm}$, is calculated as

$$\tau_{l,nm} = \tau_l + \tau_{nm}(\phi_l, \theta_l), \tag{1}$$

where $\tau_{nm}(\phi_l, \theta_l)$ accounts for the propagation delay across the BS array, and is measured with respect to the $(0,0)$th BS antenna. For a UPA placed in the xy-plane (see Fig. 1(b)), we then have [24]

$$\tau_{nm}(\phi_l, \theta_l) \triangleq \frac{d(n \sin\theta_l \cos\phi_l + m \sin\theta_l \sin\phi_l)}{c}, \tag{2}$$

where d is the antenna separation, and c is the speed of light. The channel frequency response is derived as follows. Let $\mathtt{x}(t)$ be the baseband signal transmitted by the user, with $\mathcal{F}\{\mathtt{x}(t)\} = x(f)$. The passband signal, $\tilde{r}_{nm}(t)$, received by the (n,m)th BS antenna is written in the noiseless case as [25]

$$\tilde{r}_{nm}(t) = \sum_{l=0}^{L} \sqrt{2}\text{Re}\left\{\mathtt{x}_l(t - \tau_{l,nm}) e^{j2\pi f_c(t-\tau_{l,nm})}\right\}, \tag{3}$$

where f_c is the carrier frequency, $\mathtt{x}_l(t) \triangleq \mathtt{x}(t) * \chi_l(t)$ is the distorted baseband waveform due to the frequency-selective attenuation of the lth path, and $\chi_l(t)$ models the said distortion; namely, $\mathcal{F}\{\chi_l(t)\} = \alpha_l(f)$ and $\mathcal{F}\{\mathtt{x}_l(t)\} = \alpha_l(f)x(f)$ [26].

[1]Near-field considerations are provided in Section VI-D.

Next, the received passband signal $\tilde{r}_{nm}(t)$ is down-converted to the baseband signal $\mathtt{r}_{nm}(t)$, which is given by

$$\mathtt{r}_{nm}(t) = \sum_{l=0}^{L} e^{-j2\pi f_c \tau_l} e^{-j2\pi f_c \tau_{nm}(\phi_l,\theta_l)} \mathtt{x}_l(t-\tau_{l,nm}). \quad (4)$$

Taking the continuous-time Fourier transform of (4) yields

$$\begin{aligned} r_{nm}(f) &= \mathcal{F}\{\mathtt{r}_{nm}(t)\} \\ &= \sum_{l=0}^{L} \beta_l(f) e^{-j2\pi(f_c+f)\tau_{nm}(\phi_l,\theta_l)} x(f) e^{-j2\pi f \tau_l}, \quad (5) \end{aligned}$$

where $\beta_l(f) \triangleq \alpha_l(f) e^{-j2\pi f_c \tau_l}$ is the complex gain of the lth path. Lastly, collecting all $r_{nm}(f)$ into a vector $\mathbf{r}(f) \in \mathbb{C}^{N_B \times 1}$ gives the relation $\mathbf{r}(f) = \mathbf{h}(f)x(f)$, where

$$\mathbf{h}(f) = \sum_{l=0}^{L} \beta_l(f) \mathbf{a}(\phi_l, \theta_l, f) e^{-j2\pi f \tau_l} \quad (6)$$

is the baseband frequency response of the uplink channel, and

$$\begin{aligned} \mathbf{a}(\phi,\theta,f) = \Big[1, \ldots, e^{-j2\pi(f_c+f)\frac{d}{c}(n\sin\theta\cos\phi + m\sin\theta\sin\phi)}, \\ \ldots, e^{-j2\pi(f_c+f)\frac{d}{c}((N-1)\sin\theta\cos\phi + (M-1)\sin\theta\sin\phi)}\Big]^T \quad (7) \end{aligned}$$

is the array response vector of the BS. Here, the array response is frequency-dependent due to the *spatial-wideband* effect.[2]

We now introduce the path attenuation model. First, the so-called molecular absorption loss is no longer negligible at THz frequencies. Therefore, the path attenuation of the LoS path is calculated as [27]

$$|\beta_0(f)| = \alpha_0(f) = \frac{c}{4\pi(f_c+f)\mathtt{D}} e^{-\frac{1}{2}k_{\text{abs}}(f_c+f)\mathtt{D}}, \quad (8)$$

where $\mathtt{D}$ denotes the distance between the BS and the user, and $k_{\text{abs}}(\cdot)$ is the molecular absorption coefficient determined by the composition of the propagation medium; different from mmWave channels, the major molecular absorption in THz bands comes from water vapor molecules [27]. For the NLoS paths, we consider single-bounce reflected rays, since the diffused and diffracted rays are heavily attenuated for distances larger than a few meters [28]. To this end, the reflection coefficient, $\Gamma_l(f)$, should be taken into account, which is specified as [29, Eq. (2)]

$$\Gamma_l(f) = \frac{\cos\phi_{i,l} - n_t\cos\phi_{t,l}}{\cos\phi_{i,l} + n_t\cos\phi_{t,l}} e^{-\left(\frac{8\pi^2(f_c+f)^2\sigma^2_{\text{rough}}\cos^2\phi_{i,l}}{c^2}\right)}, \quad (9)$$

where $n_t \triangleq Z_0/Z$ is the refractive index, $Z_0 = 377\ \Omega$ is the free-space impedance, Z is the impedance of the reflecting material, $\phi_{i,l}$ is the incidence and reflection angle, $\phi_{t,l} = \arcsin\left(n_t^{-1}\sin\phi_{i,l}\right)$ is the refraction angle, and σ_{rough} characterizes the roughness of the reflecting surface. The path attenuation of the lth NLoS path is finally given by [30]

$$|\beta_l(f)| = \alpha_l(f) = |\Gamma_l(f)|\alpha_0(f), \quad (10)$$

where $l = 1, \ldots, L$.

[2]If the delay across the BS array is small relative to the symbol period, then $\mathtt{x}_l(t-\tau_{l,nm}) \approx \mathtt{x}_l(t-\tau_l)$. In this case, we have a spatially narrowband channel with frequency-flat array response vectors, i.e., $\mathbf{a}(\phi,\theta,0)$.

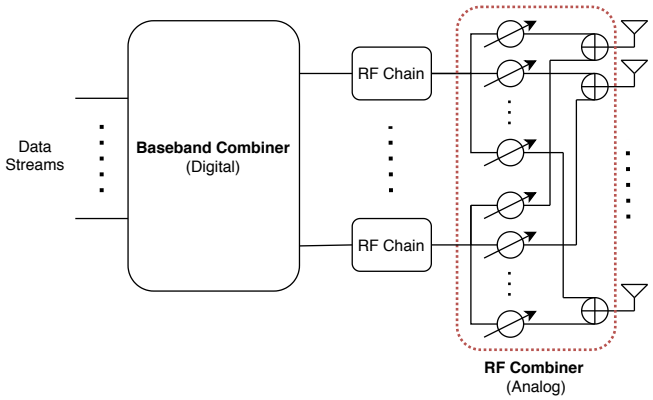

Fig. 2: Illustration of the hybrid array structure considered in the system model.

B. Hybrid Transceiver Model

Due to the frequency selectivity of the THz channel, OFDM modulation is employed to combat inter-symbol interference. Specifically, we consider S subcarriers over a signal bandwidth B. Then, the baseband frequency of the sth subcarrier is specified as $f_s = \left(s - \frac{S-1}{2}\right)\frac{B}{S}, s = 0, \ldots, S-1$. A hybrid analog-digital architecture with $N_{\text{RF}} \ll N_B$ RF chains is also considered at the BS to facilitate efficient hardware implementation; each RF chain drives the array through N_B analog phase shifters, as shown in Fig. 2. The hybrid combiner for the sth subcarrier is hence expressed as $\mathbf{F}[s] = \mathbf{F}_{\text{RF}}\mathbf{F}_{\text{BB}}[s] \in \mathbb{C}^{N_B \times N_{\text{RF}}}$, where $\mathbf{F}_{\text{RF}} \in \mathbb{C}^{N_B \times N_{\text{RF}}}$ is the frequency-flat RF combiner with elements of constant amplitude, i.e., $\frac{1}{\sqrt{N_B}}$, but variable phase, and $\mathbf{F}_{\text{BB}}[s] \in \mathbb{C}^{N_{\text{RF}} \times N_{\text{RF}}}$ is the baseband combiner. Finally, the post-processed baseband signal, $\mathbf{y}[s] \in \mathbb{C}^{N_{\text{RF}} \times 1}$, for the sth subcarrier is written as

$$\begin{aligned} \mathbf{y}[s] &= \mathbf{F}^H[s]\mathbf{r}[s] \\ &= \mathbf{F}^H[s]\left(\sqrt{P_d}\mathbf{h}[s]x[s] + \mathbf{n}[s]\right), \quad (11) \end{aligned}$$

where $\mathbf{r}[s] \triangleq \mathbf{r}(f_s)$ and $\mathbf{h}[s] \triangleq \mathbf{h}(f_s)$ are the received signal and uplink channel, respectively, $x[s] \triangleq x(f_s) \sim \mathcal{CN}(0,1)$ is the data symbol transmitted at the sth subcarrier, P_d denotes the average power per data subcarrier assuming equal power allocation among subcarriers, and $\mathbf{n}[s] \sim \mathcal{CN}(\mathbf{0}, \sigma^2\mathbf{I}_{N_B})$ is the additive noise vector.

Remark 1. *A promising alternative to OFDM is single-carrier with frequency domain equalization (SC-FDE) due to its favorable peak-to-average power ratio (PAPR). In our work, we exploit the inherent characteristics of THz channels, i.e., high path loss and directional transmissions, which result in a coherence bandwidth of hundreds of MHz [28]. Therefore, a relatively small number of subcarriers is used, which is expected to yield a tolerant PAPR.*

III. Hybrid Combining

A. The Beam Squint Problem

Even for a moderate number of BS antennas, the propagation delay across the array can exceed the sampling period due

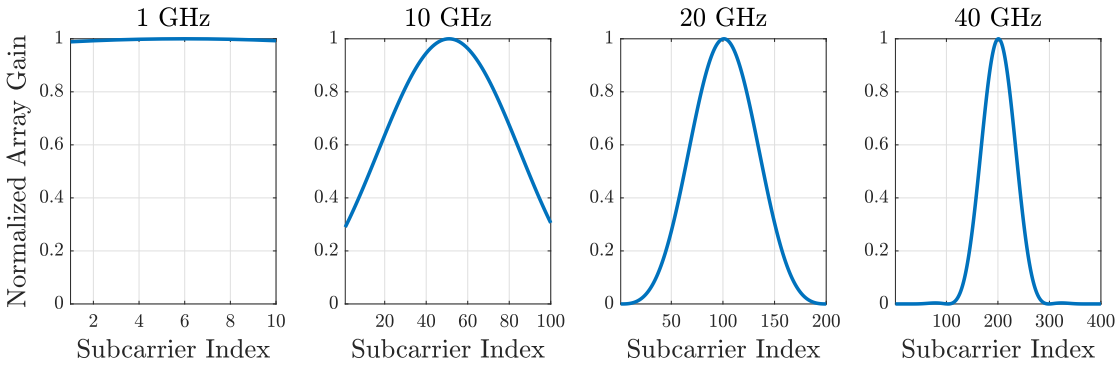

Fig. 3: Normalized array gain for various bandwidths; 100×100-element UPA, $f_c = 300$ GHz, coherence bandwidth of 100 MHz, and $(\phi, \theta) = (\pi/3, \pi/4)$.

to the ultra-high bandwidth used in THz communication. As a result, the DoA/DoD varies across the OFDM subcarriers, and the array gain becomes frequency-selective. This phenomenon, known as *beam squint* in the array processing literature, calls for a frequency-dependent combining design which is feasible only in a fully-digital array architecture.

To demonstrate the detrimental effect of beam squint when frequency-flat RF combining is employed, we consider a single ray impinging on the BS array with DoA (ϕ, θ); thus, we omit the subscript "l" hereafter. In the narrowband case, the uplink channel is given by $\mathbf{h}(0) = \beta \mathbf{a}(\phi, \theta, 0)$. Let $\mathbf{f}_{\text{RF}} = \mathbf{f}/\sqrt{N_B}$ be an arbitrary RF combiner, with $\|\mathbf{f}\|^2 = N_B$. For the combiner $\mathbf{f}_{\text{RF}}$, the power of the received signal is calculated as

$$|\beta|^2 \frac{\left|\mathbf{f}^H \mathbf{a}(\phi, \theta, 0)\right|^2}{N_B} P_d = |\beta|^2 N_B G(\phi, \theta, 0) P_d, \tag{12}$$

where $G(\phi, \theta, f) \triangleq |\mathbf{f}^H \mathbf{a}(\phi, \theta, f)|^2 / N_B^2$ is the *normalized array gain*. Choosing $\mathbf{f} = \mathbf{a}(\phi, \theta, 0)$ yields $G(\phi, \theta, 0) = 1$, and the maximum array gain is obtained. In a wideband THz system, though, the array gain varies across the OFDM subcarriers. In particular, we have that

$$\begin{aligned} G(\phi, \theta, f) &= \frac{|\mathbf{a}^H(\phi, \theta, 0) \mathbf{a}(\phi, \theta, f)|^2}{N_B^2} \\ &= \left|D_N(2\pi f \Delta_x(\phi, \theta))\right|^2 \left|D_M(2\pi f \Delta_y(\phi, \theta))\right|^2, \end{aligned} \tag{13}$$

where $\Delta_x(\phi, \theta) \triangleq (d \sin\theta \cos\phi)/c$ and $\Delta_y(\phi, \theta) \triangleq (d \sin\theta \sin\phi)/c$; please refer to Appendix A for the proof. Figure 3 shows the array gain for various bandwidths, when the narrowband RF combiner $\mathbf{f}_{\text{RF}} = \mathbf{a}(\phi, \theta, 0)/\sqrt{N_B}$ is used. As we see, the array gain reduces substantially across the OFDM subcarriers. Furthermore, using the technique of [31], one can show that $G(\phi, \theta, f) \to 0$ as $NM \to \infty$. Contrary to narrowband massive MIMO, where the signal power increases monotonically with the number of BS antennas, here it may decrease. Consequently, beam squint compensation is of paramount importance for the successful deployment of THz massive MIMO systems.

B. Proposed Combiner for Single-Path Channels

In this section, we introduce our wideband combining scheme for single-path channels, and then extend it to the multi-path case. To this end, we consider that the BS employs a single RF chain to combine the incoming signal, and hence the RF combiner is denoted by $\mathbf{f}_{\text{RF}}$. Next, we analyze the normalized array gain by decomposing the array into $N_{\text{sb}} \times M_{\text{sb}}$ virtual subarrays of $\tilde{N}\tilde{M}$ antennas each, where $\tilde{N} \triangleq N/N_{\text{sb}}$ and $\tilde{M} \triangleq M/M_{\text{sb}}$.

1) Virtual Array Partition: The array response vector in (7) is decomposed as

$$\mathbf{a}(\phi, \theta, f) = \mathbf{a}_x(\phi, \theta, f) \otimes \mathbf{a}_y(\phi, \theta, f), \tag{14}$$

where $\mathbf{a}_x(\cdot)$ and $\mathbf{a}_y(\cdot)$ are defined, respectively, as

$$\begin{aligned} \mathbf{a}_x(\phi, \theta, f) \triangleq \Big[1, \ldots, e^{-j2\pi(f_c+f)n\Delta_x(\phi,\theta)}, \\ \ldots, e^{-j2\pi(f_c+f)(N-1)\Delta_x(\phi,\theta)}\Big]^T \end{aligned} \tag{15}$$

and

$$\begin{aligned} \mathbf{a}_y(\phi, \theta, f) \triangleq \Big[1, \ldots, e^{-j2\pi(f_c+f)m\Delta_y(\phi,\theta)}, \\ \ldots, e^{-j2\pi(f_c+f)(M-1)\Delta_y(\phi,\theta)}\Big]^T. \end{aligned} \tag{16}$$

Using the previously mentioned virtual array partition, we can write

$$\mathbf{a}_x(\phi, \theta, f) = \left[\mathbf{a}_{x,1}(\phi, \theta, f), \ldots, \mathbf{a}_{x,N_{\text{sb}}}(\phi, \theta, f)\right]^T, \tag{17}$$

$$\mathbf{a}_y(\phi, \theta, f) = \left[\mathbf{a}_{y,1}(\phi, \theta, f), \ldots, \mathbf{a}_{y,M_{\text{sb}}}(\phi, \theta, f)\right]^T, \tag{18}$$

where $\mathbf{a}_{x,n}(\phi, \theta, f)$ corresponds to the response vector of the nth virtual subarray, which is defined as

$$\begin{aligned} \mathbf{a}_{x,n}(\phi, \theta, f) \triangleq \Big[e^{-j2\pi(f_c+f)(n-1)\tilde{N}\Delta_x(\phi,\theta)}, \\ \ldots, e^{-j2\pi(f_c+f)(n\tilde{N}-1)\Delta_x(\phi,\theta)}\Big]^T. \end{aligned} \tag{19}$$

Finally, each vector $\mathbf{a}_{x,n}(\phi, \theta, f)$ is expressed in terms of $\mathbf{a}_{x,1}(\phi, \theta, f)$, i.e., the response of the *first subarray*, as

$$\mathbf{a}_{x,n}(\phi, \theta, f) = e^{-j2\pi(f_c+f)(n-1)\tilde{N}\Delta_x(\phi,\theta)} \mathbf{a}_{x,1}(\phi, \theta, f). \tag{20}$$

We stress that similar expressions hold for the vector $\mathbf{a}_y$. Capitalizing on the virtual subarray notation, the normalized array gain $G(\phi, \theta, f)$ is recast as in (21) at the bottom of the next page. Then, for an adequately small $\tilde{N}\tilde{M}$, we have the approximation $|D_{\tilde{N}}(2\pi f_s \Delta_x(\phi, \theta))|^2 |D_{\tilde{M}}(2\pi f_s \Delta_y(\phi, \theta))|^2 \approx 1$.

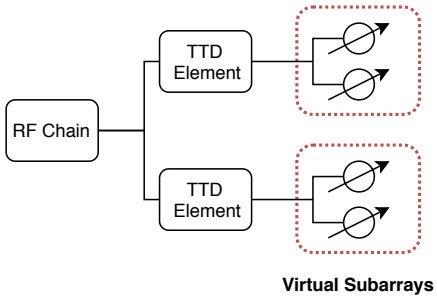

Fig. 4: Illustration of the TTD-based wideband combiner with virtual array partition; the circles with arrows represent frequency-flat phase shifters.

2) Size of Virtual Subarrays: The size of each virtual subarray, $\tilde{N} \times \tilde{M}$, is selected such that the maximum delay across the first virtual subarray is smaller than the sampling period $1/B$. Specifically, the maximum delay, $\tau_{\max}$, across the first subarray is given by (2) for $n = \tilde{N} - 1$, $m = \tilde{M} - 1$, $\sin\theta = 1$, and $\sin\phi = \cos\phi = 1/\sqrt{2}$, yielding $\tau_{\max} = d(\tilde{N} + \tilde{M} - 2)/(\sqrt{2}c)$. For half-wavelength antenna spacing and $\tilde{N} = \tilde{M}$, the condition $\tau_{\max} < 1/B$ reduces to $(\tilde{N} - 1) < \sqrt{2} f_c/B$, which is used to determine $\tilde{N}$.

3) TTD-Based Combining: The factor $\Omega(\phi, \theta, f) \leq 1$ in (21) accounts for the losses caused by the delay between consecutive virtual subarrays, and it can be canceled through an analog TTD network placed between virtual subarrays, as depicted in Fig. 4. Then, we obtain $\Omega(\phi, \theta, f_s) = 1$ by multiplying the received signal at the (n, m)th virtual subarray by $e^{j2\pi f_s \Delta_{mn}(\phi,\theta)}$, where $\Delta_{mn}(\phi, \theta) \triangleq (n-1)\tilde{N}\Delta_x(\phi, \theta) + (m-1)\tilde{M}\Delta_y(\phi, \theta)$ is the delay to be mitigated. Because all OFDM subcarriers share the same delay $\Delta_{mn}(\phi, \theta)$, this can be compensated using a single TTD element. Therefore, the wideband RF combiner is designed as

$$\mathbf{f}_{\text{RF}}[s] = \frac{1}{\sqrt{N_B}} \text{vec}\left(\mathbf{A}(\phi, \theta, 0) \odot \mathbf{T}[s]\right), \tag{22}$$

where $\mathbf{T}[s] \triangleq \left[e^{-j2\pi f_s \Delta_{mn}(\phi,\theta)}\right]_{m=1,n=1}^{M_{\text{sb}}, N_{\text{sb}}} \otimes \mathbf{1}_{\tilde{M}\times\tilde{N}}$ contains the frequency-dependent phase shifts of the TTD network, $\mathbf{A}(\phi, \theta, 0) \triangleq \mathbf{a}_y(\phi, \theta, 0)\mathbf{a}_x^T(\phi, \theta, 0)$ is realized by the frequency-flat phase shifters, and $\|\mathbf{f}_{\text{RF}}[s]\|^2 = 1$.

Proposition 1. *With the proposed combiner* (22)*, we have*

$$\left|\mathbf{f}_{\text{RF}}^H \mathbf{a}(\phi, \theta, f)\right|^2 = N_B \left|D_{\tilde{N}}(2\pi f \Delta_x)\right|^2 \left|D_{\tilde{M}}(2\pi f \Delta_y)\right|^2, \tag{23}$$

where $D_N(x) = \frac{\sin(Nx/2)}{N\sin(x/2)}$ *is the Dirichlet sinc function.*

Proof. See Appendix B. □

From (23), we conclude that for sufficiently small $\tilde{N}$ and $\tilde{M}$, an array gain N_B is approximately achieved over the whole signal bandwidth B. Thus, the SNR at the sth OFDM subcarrier is $|\beta(f_s)|^2 N_B P_d/\sigma^2$. Lastly, $(N_{\text{sb}} M_{\text{sb}} - 1)$ TTD elements are employed per RF chain, where $N_{\text{sb}} = N/\tilde{N}$ and $M_{\text{sb}} = M/\tilde{M}$.

C. Proposed Combiner for Multi-Path Channels

The propounded method can readily be applied to multi-path channels. For example, consider a THz channel comprising of $L = 2$ NLoS paths. In a fully-digital array, the optimal combiner for the sth subcarrier is given by the maximum-ratio combiner $\mathbf{h}[s]/\|\mathbf{h}[s]\|$. By employing $N_{\text{RF}} = 2$ RF chains, we have that

$$\frac{\mathbf{h}[s]}{\|\mathbf{h}[s]\|} = \mathbf{F}_{\text{RF}}[s]\mathbf{F}_{\text{BB}}[s]\mathbf{1}_{2\times 1}, \tag{24}$$

where

$$\mathbf{F}_{\text{RF}}[s] = \frac{1}{\sqrt{N_B}}\left[\mathbf{a}(\phi_1, \theta_1, f_s) \quad \mathbf{a}(\phi_2, \theta_2, f_s)\right], \tag{25}$$

$$\mathbf{F}_{\text{BB}}[s] = \frac{\sqrt{N_B}}{|\mathbf{h}[s]|}\begin{bmatrix}\beta_1(f_s)e^{-j2\pi f_s \tau_1} & 0 \\ 0 & \beta_2(f_s)e^{-j2\pi f_s \tau_2}\end{bmatrix}. \tag{26}$$

The columns of the *wideband* RF combiner $\mathbf{F}_{\text{RF}}[s]$ are then approximated using (22), whilst the vector $\mathbf{1}_{2\times 1}$ with unit entries performs the addition of the two outputs of the baseband combiner. Note that $N_{\text{RF}} = L$ are required to implement the maximum-ratio combiner in a hybrid array architecture.

Remark 2. *A few recent papers in the literature (e.g., [32] and references therein) suggested the use of TTD to provide frequency-dependent phase shifts at each antenna of an N-element ULA, yielding a wideband multi-beam architecture. In our work, we adopt a hybrid array architecture, where each frequency-independent phase shifter drives a single antenna whilst each TTD element controls a group of antennas, i.e., virtual subarray. Moreover, we consider a UPA, and hence our design enables squint-free three-dimensional (3D) combining.*

IV. Sparse Channel Estimation

We have introduced an effective wideband combiner assuming that the BS has perfect knowledge of the uplink channel. In this section, we investigate the channel estimation problem under the *spatial-wideband* effect. More particularly, we first formulate a CS problem to estimate the channel at each subcarrier independently with reduced training overhead. We then propound a wideband dictionary and employ an estimation algorithm that leverages information from multiple subcarriers to increase the reliability of the channel estimates in the low and moderate SNR regimes.

$$G(\phi, \theta, f) = \frac{\left|\mathbf{a}_{x,1}^H(\phi, \theta, 0)\mathbf{a}_{x,1}(\phi, \theta, f)\right|^2 \left|\mathbf{a}_{y,1}^H(\phi, \theta, 0)\mathbf{a}_{y,1}(\phi, \theta, f)\right|^2}{\tilde{N}^2\tilde{M}^2} \underbrace{\frac{\left|\sum_{n=1}^{N_{\text{sb}}}\sum_{m=1}^{M_{\text{sb}}} e^{-j2\pi(n-1)\tilde{N}f\Delta_x(\phi,\theta)} e^{-j2\pi(m-1)\tilde{M}f\Delta_y(\phi,\theta)}\right|^2}{N_{\text{sb}}^2 M_{\text{sb}}^2}}_{\Omega(\phi,\theta,f)}$$

$$= \left|D_{\tilde{N}}(2\pi f\Delta_x(\phi, \theta))\right|^2 \left|D_{\tilde{M}}(2\pi f\Delta_y(\phi, \theta))\right|^2 \Omega(\phi, \theta, f). \tag{21}$$

A. Problem Formulation

We assume a block-fading model where the channel coherence time is much larger than the training period. Specifically, the training period consists of N_{slot} time slots. At each time slot $t = 1, \ldots, N_{\text{slot}}$, the user transmits the pilot signal $x_t[s] = \sqrt{P_p}$, $\forall s \in \mathcal{S}$, where $\mathcal{S} \triangleq \{1, \ldots, S\}$ denotes the set of OFDM subcarriers, and P_p is the power per pilot subcarrier. In turn, the BS combines the pilot signal at each subcarrier $s \in \mathcal{S}$ using a training hybrid combiner $\mathbf{W}_t[s] \in \mathbb{C}^{N_B \times N_{\text{RF}}}$. Therefore, the post-processed signal at slot t, $\mathbf{y}_t[s] \in \mathbb{C}^{N_{\text{RF}} \times 1}$, is written as

$$\mathbf{y}_t[s] = \sqrt{P_p}\mathbf{W}_t^H[s]\mathbf{h}[s] + \mathbf{W}_t^H[s]\mathbf{n}_t[s], \tag{27}$$

where $\mathbf{n}_t[s] \sim \mathcal{CN}(\mathbf{0}, \sigma^2\mathbf{I}_{N_B})$ is the additive noise vector. Let $N_{\text{beam}} = N_{\text{slot}}N_{\text{RF}}$ denote the total number of pilot beams. After N_{slot} training slots, the BS acquires the measurement vector $\bar{\mathbf{y}}[s] \triangleq [\mathbf{y}_1^T[s], \ldots, \mathbf{y}_{N_{\text{slot}}}^T[s]]^T \in \mathbb{C}^{N_{\text{beam}} \times 1}$ for $\mathbf{h}[s]$ as

$$\begin{aligned}\bar{\mathbf{y}}[s] &= \sqrt{P_p}\begin{bmatrix}\mathbf{W}_1^H[s]\\ \vdots \\ \mathbf{W}_{N_{\text{slot}}}^H[s]\end{bmatrix}\mathbf{h}[s] + \begin{bmatrix}\mathbf{W}_1^H[s]\mathbf{n}_1[s]\\ \vdots \\ \mathbf{W}_{N_{\text{slot}}}^H[s]\mathbf{n}_{N_{\text{slot}}}[s]\end{bmatrix}\\ &= \sqrt{P_p}\,\overline{\mathbf{W}}^H[s]\mathbf{h}[s] + \bar{\mathbf{n}}[s],\end{aligned} \tag{28}$$

where $\overline{\mathbf{W}}[s] \triangleq [\mathbf{W}_1[s], \ldots, \mathbf{W}_{N_{\text{slot}}}[s]] \in \mathbb{C}^{N_B \times N_{\text{beam}}}$, and $\bar{\mathbf{n}}[s] \in \mathbb{C}^{N_{\text{beam}} \times 1}$ denotes the effective noise. More particularly, $\mathbf{R}_{\bar{\mathbf{n}}[s]} \triangleq \sigma^2\text{diag}\left(\mathbf{W}_1^H[s]\mathbf{W}_1[s], \ldots, \mathbf{W}_{N_{\text{slot}}}^H[s]\mathbf{W}_{N_{\text{slot}}}[s]\right)$ is the covariance matrix of the effective noise, which is colored in general. Regarding the pilot combiners, due to the hybrid array architecture, $\overline{\mathbf{W}}[s] = \overline{\mathbf{W}}_{\text{RF}}\overline{\mathbf{W}}_{\text{BB}}[s]$, with $\overline{\mathbf{W}}_{\text{RF}} = [\mathbf{W}_{\text{RF},1}, \ldots, \mathbf{W}_{\text{RF},N_{\text{slot}}}] \in \mathbb{C}^{N_B \times N_{\text{beam}}}$ containing the RF pilot beams and $\overline{\mathbf{W}}_{\text{BB}}[s] = \text{blkdiag}(\mathbf{W}_{\text{BB},1}[s], \ldots, \mathbf{W}_{\text{BB},N_{\text{slot}}}[s]) \in \mathbb{C}^{N_{\text{beam}} \times N_{\text{beam}}}$ comprising the $N_{\text{RF}} \times N_{\text{RF}}$ baseband combiners. The design of the pilot combiners is detailed in Section IV-D3.

B. Least Squares Estimator

From (28), we have N_{beam} observations, while $\mathbf{h}[s]$ includes N_B variables. Thus, to obtain a good estimate of $\mathbf{h}[s]$, we need that $N_{\text{beam}} \geq N_B$. With this condition, the LS estimate is[3]

$$\hat{\mathbf{h}}^{\text{LS}}[s] = \mathbf{Q}_s^{\dagger}\bar{\mathbf{y}}[s], \tag{29}$$

where $\mathbf{Q}_s \triangleq \sqrt{P_p}\,\overline{\mathbf{W}}^H[s] \in \mathbb{C}^{N_{\text{beam}} \times N_B}$ is the sensing matrix. The mean square error (MSE) of the LS estimator for the sth subcarrier is given by

$$J_s^{\text{LS}} \triangleq \mathbb{E}\left\{\left\|\mathbf{h}[s] - \hat{\mathbf{h}}^{\text{LS}}[s]\right\|^2\right\} = \text{tr}\left(\mathbf{Q}_s^{\dagger}\mathbf{R}_{\bar{\mathbf{n}}[s]}(\mathbf{Q}_s^{\dagger})^H\right). \tag{30}$$

The optimal $\mathbf{Q}_s$ satisfies $\mathbf{Q}_s^H\mathbf{Q}_s = P_p\mathbf{I}_{N_B}$ [33], [34]. In the hybrid array architecture under consideration, this is achieved by $\overline{\mathbf{W}}_{\text{BB}}[s] = \mathbf{I}_{N_B}$ and $\overline{\mathbf{W}}_{\text{RF}} = \mathbf{U} \in \mathbb{C}^{N_B \times N_B}$, where $\mathbf{U}$ is the DFT matrix generating the RF pilot beams [34]. We then have $\mathbf{R}_{\bar{\mathbf{n}}[s]} = \sigma^2\mathbf{I}_{N_B}$, $\mathbf{Q}_s^{\dagger} = (1/\sqrt{P_p})\mathbf{U}$, and

$$J_s^{\text{LS}} = \sigma^2 N_B/P_p. \tag{31}$$

[3]We consider the LS instead of the minimum mean-square error (MMSE) method because we focus on estimators that exploit only instantaneous CSI. The LS estimator (29) requires $N_{\text{beam}} \geq N_B$, and hence yields a prohibitively high training overhead when the number of RF chains is much smaller than the number of BS antennas.

C. Sparse Formulation and Orthogonal Matching Pursuit

By exploiting the angular sparsity of THz channels, we can have a sparse formulation of the channel estimation problem as follows. The physical channel in (6) is also expressed as

$$\mathbf{h}[s] = \mathbf{A}[s]\boldsymbol{\beta}[s], \tag{32}$$

where $\mathbf{A}[s] \triangleq [\mathbf{a}(\phi_0, \theta_0, f_s), \ldots, \mathbf{a}(\phi_L, \theta_L, f_s)] \in \mathbb{C}^{N_B \times (L+1)}$, with $\mathbf{a}(\phi_l, \theta_l, f_s)$ being specified by (7) for $f = f_s$, is the so-called wideband array response matrix, and $\boldsymbol{\beta}[s] \triangleq [\beta_0(f_s)e^{-j2\pi f_s\tau_0}, \ldots, \beta_L(f_s)e^{-j2\pi f_s\tau_L}]^T \in \mathbb{C}^{(L+1)\times 1}$ is the vector of channel gains. Next, consider a dictionary $\bar{\mathbf{A}}[s] \in \mathbb{C}^{N_B \times G}$ whose G columns are the array response vectors associated with a predefined set of DoA. Then, the uplink channel can be approximated as

$$\mathbf{h}[s] \approx \bar{\mathbf{A}}[s]\bar{\boldsymbol{\beta}}[s], \tag{33}$$

where $\bar{\boldsymbol{\beta}}[s] \in \mathbb{C}^{G\times 1}$ has $L+1$ nonzero entries whose positions and values correspond to their DoA and path gains [35]. Therefore, (28) is recast as

$$\bar{\mathbf{y}}[s] = \boldsymbol{\Phi}_s\bar{\boldsymbol{\beta}}[s] + \bar{\mathbf{n}}[s], \tag{34}$$

where $\boldsymbol{\Phi}_s \triangleq \sqrt{P_p}\,\overline{\mathbf{W}}^H[s]\bar{\mathbf{A}}[s] \in \mathbb{C}^{N_{\text{beam}} \times G}$ is the *equivalent* sensing matrix. Since $(L+1) \ll G$, the channel gain vector $\bar{\boldsymbol{\beta}}[s]$ is $(L+1)$-sparse, and the channel estimation problem can be formulated as the sparse recovery problem [34]

$$\begin{aligned}\hat{\bar{\boldsymbol{\beta}}}[s] = \arg\min_{\bar{\boldsymbol{\beta}}[s]} \;& \|\bar{\boldsymbol{\beta}}[s]\|_1\\ \text{s.t.} \;& \left\|\bar{\mathbf{y}}[s] - \boldsymbol{\Phi}_s\bar{\boldsymbol{\beta}}[s]\right\|_2 \leq \epsilon\end{aligned} \tag{35}$$

where $\epsilon \leq \mathbb{E}\{\|\bar{\mathbf{n}}[s]\|_2\}$ is an appropriately chosen bound on the mean magnitude of the effective noise. The above optimization problem can be solved for each subcarrier independently, i.e., single measurement vector formulation. Finally, the estimate of $\mathbf{h}[s]$ is obtained as $\hat{\mathbf{h}}^{\text{CS}}[s] = \bar{\mathbf{A}}[s]\hat{\bar{\boldsymbol{\beta}}}[s]$.

Several greedy algorithms have been proposed to find approximate solutions of the l_1-norm optimization problem. The OMP algorithm [36] described in Algorithm 1 is one of the most common and simple greedy CS methods that can solve problem (35).

Algorithm 1 OMP-Based Estimator

Input: equivalent sensing matrix $\boldsymbol{\Phi}_s$ and measurement vector $\bar{\mathbf{y}}[s]$ for the sth subcarrier, and a threshold ϵ.
1: $\mathcal{I}_{-1} = \emptyset$, $\mathcal{G} = \{1, \ldots, G\}$, $\mathbf{r}_{-2}[s] = \mathbf{0}$, $\mathbf{r}_{-1}[s] = \bar{\mathbf{y}}[s]$, and $l = 0$.
2: **while** $\|\mathbf{r}_{l-1}[s] - \mathbf{r}_{l-2}[s]\|^2 > \epsilon$ **do**
3: $\quad g^{\star} = \arg\max_{g\in\mathcal{G}} \left|\boldsymbol{\Phi}_s^H(g)\mathbf{r}_{l-1}[s]\right|$
4: $\quad \mathcal{I}_l = \mathcal{I}_{l-1} \cup \{g^{\star}\}$
5: $\quad \mathbf{r}_l[s] = \left(\mathbf{I}_{N_{\text{beam}}} - \boldsymbol{\Phi}_s(\mathcal{I}_l)\boldsymbol{\Phi}_s^{\dagger}(\mathcal{I}_l)\right)\bar{\mathbf{y}}[s]$
6: $\quad l = l + 1$
7: **end while**
8: $\hat{\bar{\boldsymbol{\beta}}}[s] = \boldsymbol{\Phi}_s^{\dagger}(\mathcal{I}_{l-1})\bar{\mathbf{y}}[s]$
9: **return** $\hat{\mathbf{h}}^{\text{CS}}[s] = \bar{\mathbf{A}}[s]\hat{\bar{\boldsymbol{\beta}}}[s]$.

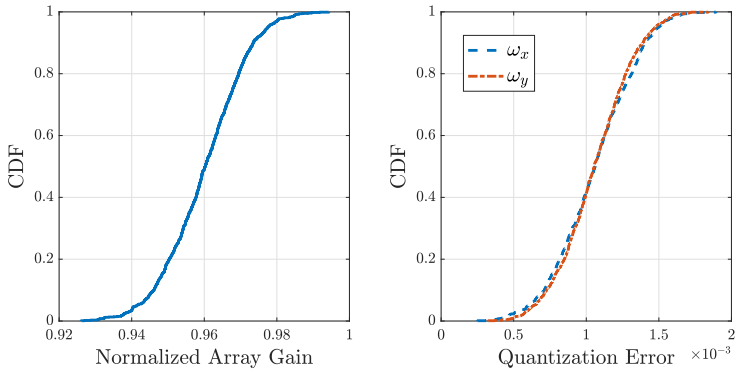

Fig. 5: CDF of the normalized array gain and quantization error for a single-path channel and a super-resolution dictionary with $G_x = 4N$ and $G_y = 4M$; 1,000 channel realizations, 40×40-element UPA, $\mathbf{f}_{\text{RF}} = \mathbf{a}(\bar{\omega}_x(q), \bar{\omega}_y(p), f_s)/\sqrt{N_B}$, $B = 40$ GHz, $S = 400$ subcarriers, and $s = 200$th subcarrier.

D. Proposed Channel Estimator

1) Wideband Dictionary for UPAs: For half-wavelength antenna separation, the array response vector (7) is recast as

$$\mathbf{a}(\omega_x, \omega_y, f) = \Big[1, \ldots, e^{-j2\pi\left(1+\frac{f}{f_c}\right)(n\omega_x + m\omega_y)}, \ldots, e^{-j2\pi\left(1+\frac{f}{f_c}\right)((N-1)\omega_x + (M-1)\omega_y)}\Big]^T, \quad (36)$$

where $\omega_x = 1/2 \sin\theta\cos\phi$ and $\omega_y = 1/2 \sin\theta \sin\phi$ are the *spatial frequencies* [37]. The one-to-one mapping between the spatial frequencies (ω_x, ω_y) and the physical angles (ϕ, θ) is given by the relationships

$$\phi = \tan^{-1}\left(\omega_y/\omega_x\right), \quad (37)$$

$$\theta = \sin^{-1}\left(2\sqrt{\omega_x^2 + \omega_y^2}\right). \quad (38)$$

Since both ω_x and ω_y lie in $[-1/2, 1/2]$, we consider the grids of discrete spatial frequencies

$$\mathcal{G}_x = \{\bar{\omega}_x(q) = q/G_x,\ q = -(G_x-1)/2, \ldots, (G_x-1)/2\}, \quad (39)$$

$$\mathcal{G}_y = \{\bar{\omega}_y(p) = p/G_y,\ p = -(G_y-1)/2, \ldots, (G_y-1)/2\}, \quad (40)$$

where $G_x G_y = G$ is the overall dictionary size.

For the sth subcarrier, we define the array response matrices $\bar{\mathbf{A}}_x[s] \in \mathbb{C}^{N \times G_x}$ and $\bar{\mathbf{A}}_y[s] \in \mathbb{C}^{M \times G_y}$ whose columns are the array response vectors $\mathbf{a}_x(\cdot, f_s)$ and $\mathbf{a}_y(\cdot, f_s)$ evaluated at the grid points of $\mathcal{G}_x$ and $\mathcal{G}_y$, respectively. Now, the dictionary $\bar{\mathbf{A}}[s] \triangleq \bar{\mathbf{A}}_x[s] \otimes \bar{\mathbf{A}}_y[s] \in \mathbb{C}^{N_B \times G}$ can be used to approximate the uplink channel $\mathbf{h}[s]$ at the sth subcarrier. Although this approximation entails quantization errors, these become small for large G_x and G_y [35]. More specifically, we can use a super-resolution dictionary with $G_x > N$ and $G_y > M$ to reduce the mismatch between the quantized and the actual channel. We evaluate the accuracy of the proposed dictionary by generating a DoA with (ω_x, ω_y), which is then quantized to the closest value $(\bar{\omega}_x(q), \bar{\omega}_y(p))$. Figure 5 shows the cumulative distribution function (CDF) of the normalized array gain $\left|\mathbf{a}^H(\bar{\omega}_x(q), \bar{\omega}_y(p), f_s)\mathbf{a}(\omega_x, \omega_y, f_s)\right|^2/N_B^2$, and the quantization errors $|\omega_x - \bar{\omega}_x(q)|$ and $|\omega_y - \bar{\omega}_y(p)|$ of the spatial frequencies. As observed, the errors are small, and do not affect significantly the normalized array gain. Consequently, we neglect the quantization errors and assume that the DoA of each path lies on the dictionary grid. Note that for $G_x = N$ and $G_y = M$, the dictionary $\bar{\mathbf{A}}[s]$ reduces to the known virtual channel representation (VCR) [38] in the spatial-narrowband case. Lastly, a similar representation, termed extended VCR, was introduced in [39] for narrowband massive MIMO systems.

2) Generalized Multiple Measurement Vector Problem: Thanks to the frequency-dependent dictionary, the channel gain vectors $\{\bar{\boldsymbol{\beta}}[s]\}_{s=0}^{S-1}$ share the same support. Therefore, we can exploit the common support property and consider the problem in (35) as a generalized multiple measurement vector (GMMV) problem, where multiple sensing matrices are employed [40]. To solve the GMMV problem, we employ the simultaneous OMP algorithm [41]. The proposed channel estimator is described in Algorithm 2.

Algorithm 2 GSOMP-Based Estimator

Input: set $\mathcal{S}$ of pilot subcarriers, sensing matrices $\boldsymbol{\Phi}_s$ and measurement vectors $\bar{\mathbf{y}}[s], \forall s \in \mathcal{S}$, and a threshold ϵ.

$\mathcal{I}_{-1} = \emptyset$, $\mathcal{G} = \{1, \ldots, G\}$, $\mathbf{r}_{-1}[s] = \bar{\mathbf{y}}[s]$, $\mathsf{MSE} = \sum_{s\in\mathcal{S}} \|\bar{\mathbf{y}}[s]\|^2$, and $l = 0$.
while $\mathsf{MSE} > \epsilon$ **do**
  $g^\star = \underset{g \in \mathcal{G}\setminus\mathcal{I}_{l-1}}{\arg\max} \sum_{s\in\mathcal{S}} \left|\boldsymbol{\Phi}_s^H(g)\mathbf{r}_{l-1}[s]\right|$
  $\mathcal{I}_l = \mathcal{I}_{l-1} \cup \{g^\star\}$
  $\mathbf{r}_l[s] = \left(\mathbf{I}_{N_{\text{beam}}} - \boldsymbol{\Phi}_s(\mathcal{I}_l)\boldsymbol{\Phi}_s^\dagger(\mathcal{I}_l)\right)\bar{\mathbf{y}}[s],\ \forall s \in \mathcal{S}$
  $\mathsf{MSE} = \frac{1}{|\mathcal{S}|}\sum_{s\in\mathcal{S}} \|\mathbf{r}_l[s] - \mathbf{r}_{l-1}[s]\|^2$
  $l = l + 1$
end while
$\hat{\bar{\boldsymbol{\beta}}}[s] = \boldsymbol{\Phi}_s^\dagger(\mathcal{I}_{l-1})\bar{\mathbf{y}}[s], \forall s \in \mathcal{S}$
return $\hat{\mathbf{h}}^{\text{CS}}[s] = \bar{\mathbf{A}}[s]\hat{\bar{\boldsymbol{\beta}}}[s], \forall s \in \mathcal{S}$.

Regarding the stopping criterion of the OMP/GSOMP algorithms, we design the pilot combiners so that the effective noise is white. In this case, the variance of the noise power is $\mathbb{E}\left\{\|\bar{\mathbf{n}}[s]\|^2\right\} = N_{\text{beam}}\sigma^2$, and the threshold can be chosen as $\epsilon = N_{\text{beam}}\sigma^2$, or a fraction of the average noise power. Additionally, a thresholding step can be incorporated into the algorithms, in which only the entries of the estimate $\hat{\bar{\boldsymbol{\beta}}}$

with power higher than the noise variance will be selected as detected paths. After estimating the spatial frequencies of each path, the physical angles are obtained through (37) and (38), which are then used in the TTD-based wideband combiner.

3) Pilot Beam Design: The elements of the RF combiner $\overline{\mathbf{W}}_{\text{RF}}$ are selected from the set $\{-1/\sqrt{N_B}, 1/\sqrt{N_B}\}$ with equal probability. The reason we adopt a randomly formed RF combiner is that it has been shown to have a low mutual-column coherence, and therefore can be expected to attain a high recovery probability according to the CS theory [42]. The specific RF pilot design leads to a colored effective noise, however the SOMP algorithm is based on the assumption that the noise covariance matrix is diagonal. To this end, we design the baseband combiner such that the combined noise remains white. In particular, let $\mathbf{D}_t^H\mathbf{D}_t$ be the Cholesky decomposition of $\mathbf{W}_{\text{RF,t}}^H\mathbf{W}_{\text{RF,t}}$, where $\mathbf{D} \in \mathbb{C}^{N_{\text{RF}}\times N_{\text{RF}}}$ is an upper triangular matrix. Then, the baseband combiner of the tth slot is set to $\mathbf{W}_{\text{BB},t}[s] = \mathbf{D}_t^{-1}$, and hence $\overline{\mathbf{W}}[s] = \overline{\mathbf{W}}_{\text{RF}}\text{blkdiag}(\mathbf{D}_1^{-1}, \ldots, \mathbf{D}_{N_{\text{slot}}}^{-1})$. Under this pilot beam design, the covariance matrix of the effective noise becomes $\mathbf{R}_{\bar{\mathbf{n}}} = \sigma^2\mathbf{I}_{N_{\text{beam}}}$, yielding the desired result. We finally point out that the combiners $\overline{\mathbf{W}}[s]$ can be computed offline.

E. Performance of the Proposed Channel Estimator

1) Lower Bound Error Analysis: As previously mentioned, for semi-unitary combiners $\mathbf{W}_t[s]$ with $\mathbf{W}_t^H[s]\mathbf{W}_t[s] = \mathbf{I}_{N_{\text{RF}}}, \forall t = 1, \ldots, N_{\text{slot}}$, the covariance matrix of the effective noise $\bar{\mathbf{n}}[s]$ is equal to $\sigma^2\mathbf{I}_{N_{\text{beam}}}$. Next, we derive the CRLB assuming that the GSOMP recovers the exact support of $\bar{\boldsymbol{\beta}}[s]$, i.e., $\mathcal{I}_{l-1} = \text{supp}\left(\bar{\boldsymbol{\beta}}[s]\right) = \mathcal{I}$.[4] To this end, we can define the following linear model for the sth subcarrier

$$\bar{\mathbf{y}}[s] = \boldsymbol{\Phi}_s(\mathcal{I})\tilde{\bar{\boldsymbol{\beta}}}[s] + \bar{\mathbf{n}}[s], \tag{41}$$

where $\tilde{\bar{\boldsymbol{\beta}}}[s] \in \mathbb{C}^{L\times 1}$ denotes the vector to be estimated, and $\bar{\mathbf{y}}[s]$ is distributed as $\mathcal{CN}\left(\boldsymbol{\Phi}_s(\mathcal{I})\tilde{\bar{\boldsymbol{\beta}}}[s], \sigma^2\mathbf{I}_{N_{\text{beam}}}\right)$. The model in (41) is linear on the parameter vector $\tilde{\bar{\boldsymbol{\beta}}}[s]$, and the solution $\hat{\bar{\boldsymbol{\beta}}}[s] = \boldsymbol{\Phi}_s^{\dagger}(\mathcal{I})\bar{\mathbf{y}}[s]$ gives $\mathbb{E}\left\{\hat{\bar{\boldsymbol{\beta}}}[s]\right\} = \tilde{\bar{\boldsymbol{\beta}}}[s]$. Specifically, $\hat{\bar{\boldsymbol{\beta}}}[s]$ is the mininum variance unbiased estimator of $\tilde{\bar{\boldsymbol{\beta}}}[s]$, hence attaining the CRLB [43]. Next, the Fisher information matrix for (41) is calculated as

$$\mathbf{I}\left(\tilde{\bar{\boldsymbol{\beta}}}[s]\right) = \frac{1}{\sigma^2}\boldsymbol{\Phi}_s^H(\mathcal{I})\boldsymbol{\Phi}_s(\mathcal{I}). \tag{42}$$

The channel estimate for the sth subcarrier is acquired as $\hat{\mathbf{h}}^{\text{CS}}[s] = \bar{\mathbf{A}}_s(\mathcal{I})\hat{\tilde{\bar{\boldsymbol{\beta}}}}[s]$, where $\bar{\mathbf{A}}_s(\mathcal{I})$ denotes the matrix with the columns of $\bar{\mathbf{A}}[s]$ given by the support $\mathcal{I}$. Let J_s^{CS} denote the MSE of the OMP. Since $\mathbb{E}\left\{\hat{\mathbf{h}}^{\text{CS}}\right\} = \bar{\mathbf{A}}_s(\mathcal{I})\tilde{\bar{\boldsymbol{\beta}}}[s] \triangleq \boldsymbol{\psi}\left(\tilde{\bar{\boldsymbol{\beta}}}[s]\right)$, the CRLB for the sth subcarrier is given by [43]

$$J_s^{\text{CS}} \geq \text{tr}\left\{\frac{\partial\boldsymbol{\psi}\left(\tilde{\bar{\boldsymbol{\beta}}}[s]\right)}{\partial\tilde{\bar{\boldsymbol{\beta}}}[s]}\mathbf{I}^{-1}\left(\tilde{\bar{\boldsymbol{\beta}}}[s]\right)\frac{\partial\boldsymbol{\psi}^H\left(\tilde{\bar{\boldsymbol{\beta}}}[s]\right)}{\partial\tilde{\bar{\boldsymbol{\beta}}}[s]}\right\}, \tag{43}$$

where $\partial\boldsymbol{\psi}\left(\tilde{\bar{\boldsymbol{\beta}}}[s]\right)/\partial\tilde{\bar{\boldsymbol{\beta}}}[s] = \bar{\mathbf{A}}_s(\mathcal{I})$.

[4]This is a well accepted assumption in the related literature; see [19] and references therein.

2) Complexity Analysis: In this section, we detail the computational complexity per iteration l of the GSOMP scheme. Specifically, we have the following operations:

- The l_2-norm operations at step 1 and step 6 have $\mathcal{O}(|\mathcal{S}|N_{\text{beam}})$ complexity.
- The calculation of the product $\boldsymbol{\Phi}_s^H(g)\mathbf{r}_{l-1}[s]$ at step 3 is $\mathcal{O}(|\mathcal{S}|N_{\text{beam}}(G-l))$ because there are $G-l$ elements to examine at the lth iteration, where G is the size of the dictionary.
- To find the maximum element from $G-l$ values at step 3 is on the order of $\mathcal{O}(G-l)$.
- The LS operation at step 5 is $\mathcal{O}(l^3 + 2l^2N_{\text{beam}})$ for each pilot subcarrier. This is because $\boldsymbol{\Phi}(\mathcal{I}_l)$ is a $N_{\text{beam}} \times l$ matrix, and hence its pseudoinverse entails $l^3 + l^2N_{\text{beam}}$ operations plus the multiplication with $\boldsymbol{\Phi}(\mathcal{I}_l)$ entailing l^2N_{beam} additional multiplications.

Given the above, the overall online computational complexity is $\mathcal{O}\left(|\mathcal{S}|(N_{\text{beam}}(G-l) + l^3 + 2l^2N_{\text{beam}}) + (G-l)\right)$. Note that the OMP has $\mathcal{O}(|\mathcal{S}|G)$ at step 3 for finding the maximum correlation between the measurement vector and the columns of the dictionary. As a result, the GSOMP leads to a computational reduction as well.

V. The Multi-Antenna User Case

We now discuss how the previous analysis can be extended to the case of a multi-antenna user. To this end, we consider a user with an N_U-element ULA. The frequency response of the uplink channel, $\mathbf{H}(f) \in \mathbb{C}^{N_B\times N_U}$, is then expressed as

$$\mathbf{H}(f) = \sum_{l=0}^{L}\beta_l(f)\mathbf{a}_B(\phi_l, \theta_l, f)\mathbf{a}_U^H(\varphi_l, f)e^{-j2\pi f\tau_l}, \tag{44}$$

where $\mathbf{a}_B(\cdot,\cdot,\cdot)$ denotes the response vector (7) of the BS array, φ_l is the angle-of-departure (AoD) of the lth path from the user, and

$$\mathbf{a}_U(\varphi, f) \triangleq \Big[1, e^{-j2\pi(f_c+f)\frac{d}{c}\sin\varphi}, \ldots, e^{-j2\pi(f_c+f)(N_U-1)\frac{d}{c}\sin\varphi}\Big]^T \tag{45}$$

is the wideband response vector of the user array.

At the BS, the post-processed baseband signal for the sth subcarrier is expressed as

$$\mathbf{y}[s] = \mathbf{F}^H[s]\left(\mathbf{H}[s]\mathbf{B}[s]\tilde{\mathbf{x}}[s] + \mathbf{n}[s]\right), \tag{46}$$

where $\mathbf{B}[s] \in \mathbb{C}^{N_U\times N_{\text{RF}}^u}$ is the hybrid precoder when the user employs N_{RF}^u RF chains, $\tilde{\mathbf{x}}[s] = \mathbf{P}[s]\mathbf{x}[s]$ is the transmitted signal at the sth subcarrier, $\mathbf{P}[s] = \text{diag}(p_{1,s}, \ldots, p_{N_{\text{RF}}^u,s})$ is the power allocation matrix, and $\mathbf{x}[s] \sim \mathcal{CN}(\mathbf{0}, \mathbf{I}_{N_{\text{RF}}^u})$ is the vector of data symbols. Note that the the power constraint $\sum_{s=0}^{S-1}\mathbb{E}\left\{\|\mathbf{B}[s]\tilde{\mathbf{x}}[s]\|^2\right\} \leq P_t$ should be satisfied, so that the transmit power does not exceed the user's power budget P_t.

A. Hybrid Combining and Beamforming

Consider a single-path channel with AoD φ from the user and DoA (ϕ, θ) at the BS. For the frequency-flat beamformer $\mathbf{a}_U(\varphi, 0)/\sqrt{N_U}$ and combiner $\mathbf{a}_B(\phi, \theta, 0)/\sqrt{N_B}$, the normalized array gain in (13) is recast as in (47) at the bottom

of this page, where $\Delta(\varphi) \triangleq d\sin\varphi/c$. Employing TTD-based combining and beamforming yields $G(\phi,\theta,\varphi,f) \approx 1$, and the SNR at the sth subcarrier is approximately equal to $|\beta(f_s)|^2 N_U N_B P_d/\sigma^2$. Compared to the single-antenna user case, we have an additional beamforming gain N_U.

Now consider, for instance, a multi-path channel of $L = 2$ NLoS paths. In a fully-digital array, the combiner and precoder maximizing the achievable rate are given by the singular value decomposition (SVD) of the channel matrix $\mathbf{H}[s]$ [11]. For our hybrid analog-digital array structure, we adopt a practical approach, as in [17]. We first decompose the channel matrix as $\mathbf{H}(f) = \mathbf{H}_B(f)\mathbf{H}_U^H(f)$, where

$$\mathbf{H}_B(f) = \left[\mathbf{a}_B(\phi_1,\theta_1,f), \quad \mathbf{a}_B(\phi_2,\theta_2,f)\right], \tag{48}$$

and

$$\mathbf{H}_U(f) = \big[\beta_1(f)\mathbf{a}_U(\varphi_1,f)e^{-j2\pi f\tau_1}, \\ \beta_2(f)\mathbf{a}_U(\varphi_2,f)e^{-j2\pi f\tau_2}\big]. \tag{49}$$

Next, the RF combiner and beamformer are the matched filters of the channels $\mathbf{H}_B(f)$ and $\mathbf{H}_U^H(f)$, respectively, whereas the baseband combiner and precoder are designed using the SVD of the effective channel, when both ends have full CSI. Note that for a multi-path channel with $L > N_{\text{RF}}$ paths, the user communicates at most $\min(L, N_{\text{RF}})$ spatial streams to the BS in the absence of inter-stream interference through SVD-based transmission.

B. Sparse Channel Estimation

The user employs a training codebook $\{\mathbf{v}_i \in \mathbb{C}^{N_U\times 1}, i = 1,\ldots,N^u_{\text{beam}}\}$, which consists of N^u_{beam} pilot RF beamformers. When the ith pilot beamformer is used during N_{slot} training slots, (28) is recast as

$$\bar{\mathbf{y}}_i[s] = \sqrt{P_p}\ \overline{\mathbf{W}}^H[s]\mathbf{H}[s]\mathbf{v}_i + \bar{\mathbf{n}}_i[s]. \tag{50}$$

By collecting all vectors $\bar{\mathbf{y}}_i[s]$ into a single matrix $\mathbf{Y}[s] = [\bar{\mathbf{y}}_1[s],\ldots,\bar{\mathbf{y}}_{N^u_{\text{beam}}}[s]] \in \mathbb{C}^{N_{\text{beam}}\times N^u_{\text{beam}}}$, we can write

$$\mathbf{Y}[s] = \sqrt{P_p}\ \overline{\mathbf{W}}^H[s]\mathbf{H}[s]\mathbf{V} + \mathbf{N}[s], \tag{51}$$

where $\mathbf{V} = [\mathbf{v}_1,\ldots,\mathbf{v}_{N^u_{\text{beam}}}] \in \mathbb{C}^{N_U\times N^u_{\text{beam}}}$, and $\mathbf{N} = [\bar{\mathbf{n}}_1[s],\ldots,\bar{\mathbf{n}}_{N^u_{\text{beam}}}[s]] \in \mathbb{C}^{N_{\text{beam}}\times N^u_{\text{beam}}}$. Utilizing the identity $\text{vec}(\mathbf{ABC}) = (\mathbf{C}^T\otimes\mathbf{A})\text{vec}(\mathbf{B})$, we express (51) in vector form as

$$\text{vec}(\mathbf{Y}[s]) = \sqrt{P_p}\left(\mathbf{V}^T\otimes\overline{\mathbf{W}}^H[s]\right)\text{vec}(\mathbf{H}[s]) + \text{vec}(\mathbf{N}[s]), \tag{52}$$

where $\text{vec}(\mathbf{Y}[s]) \in \mathbb{C}^{N_{\text{beam}}N^u_{\text{beam}}\times 1}$ is the overall measurement vector, $\text{vec}(\mathbf{H}[s]) \in \mathbb{C}^{N_BN_U\times 1}$ is the uplink channel to be estimated, and $\text{vec}(\mathbf{N}[s]) \in \mathbb{C}^{N_{\text{beam}}N^u_{\text{beam}}\times 1}$ is the noise vector. Now, the proposed GSOMP-based estimator can readily be used by considering the equivalent sensing matrix $\mathbf{\Phi}_s = \sqrt{P_p}\left(\mathbf{V}^T\otimes\overline{\mathbf{W}}^H[s]\right)\bar{\mathbf{A}}[s] \in \mathbb{C}^{N_{\text{beam}}N^u_{\text{beam}}\times GG^u}$, where $\bar{\mathbf{A}}[s] \triangleq \bar{\mathbf{A}}^*_u[s]\otimes(\bar{\mathbf{A}}_x[s]\otimes\bar{\mathbf{A}}_y[s]) \in \mathbb{C}^{N_BN_U\times GG^u}$ is the equivalent dictionary accounting also for the dictionary $\bar{\mathbf{A}}_u[s] \in \mathbb{C}^{N_U\times G^u}$ of size G^u at the user side. Finally, the estimated channel is constructed as $\text{vec}(\hat{\mathbf{H}}[s]) = \bar{\mathbf{A}}[s]\hat{\bar{\boldsymbol{\beta}}}[s]$.

TABLE II
MAIN SIMULATION PARAMETERS [27], [28]

Parameter	Value
Bandwidth	$B = 40$ GHz
Carrier frequency	$f_c = 300$ GHz
Transmit power	$P_t = 10$ dBm
Power density of noise	$\sigma^2 = -174$ dBm/Hz
Azimuth AoA	$\phi_l \sim \mathcal{U}(-\pi,\pi)$
Polar AoA	$\theta_l \sim \mathcal{U}(-\pi/2,\pi/2)$
LoS path length	$\mathtt{D} = 15$ m
ToA of LoS	$\tau_0 = 50$ nsec
ToA of NLoS	$\tau_l \sim \mathcal{U}(50,55)$ nsec
Absorption coefficient	$k_{\text{abs}} = 0.0033$ m^{-1}
Refractive index	$n_t = 2.24 - j0.025$
Roughness factor	$\sigma_{\text{rough}} = 0.088\cdot 10^{-3}$ m

VI. NUMERICAL RESULTS

In this section, we conduct numerical simulations to evaluate the performance of the proposed channel estimator and hybrid combiner. To this end, we consider the following setup:

- Number of OFDM Subcarriers: For a NLoS multi-path scenario where $\tau_l \sim \mathcal{U}(50,55)$ nsec, the delay spread is $D_s = 5$ nsec. The coherence bandwidth is then calculated as $B_c = 1/(2D_s) = 100$ MHz [25], which results in $S \approx B/B_c = 400$ subcarriers. On the other hand, for a LoS scenario, the delay spread is equal to the maximum delay across the UPA due to the spatial-wideband effect. This results in $S \approx 18$ subcarriers for an 100×100-element UPA and $B = 40$ GHz.
- Antenna Gain: Each BS antenna element has a directional power pattern, $\Lambda(\phi,\theta)$, which is specified according to the 3GPP standard as [48]

$$\Lambda(\phi,\theta) = \Lambda_{\max} - \min\left[-\Lambda_H(\phi) - \Lambda_V(\theta), \Lambda_{\text{FBR}}\right], \tag{53}$$

where

$$\Lambda_H(\phi) = -\min\left[12\left(\frac{\phi}{\phi_{\text{3dB}}}\right)^2, \Lambda_{\text{FBR}}\right], \tag{54}$$

$$\Lambda_V(\theta) = -\min\left[12\left(\frac{\theta-90^\circ}{\theta_{\text{3dB}}}\right)^2, \text{SLA}_v\right], \tag{55}$$

where $\min[\cdot,\cdot]$ denotes the minimum between the input arguments, $\Lambda_{\max}$ is the maximum gain in the boresight direction, $\phi_{\text{3dB}} = 65^\circ$ and $\theta_{\text{3dB}} = 65^\circ$ are the horizontal and vertical half-power beamwidths, respectively, $\Lambda_{\text{FBR}} = 30$ dB is the front-to-back ratio, and $\text{SLA}_v = 30$ dB is the side lobe attenuation in the vertical direction. We choose

$$G(\phi,\theta,\varphi,f) = \frac{|\mathbf{a}_B^H(\phi,\theta,0)\mathbf{a}_B(\phi,\theta,f)|^2}{N_B^2}\frac{|\mathbf{a}_U^H(\varphi,f)\mathbf{a}_U(\varphi,0)|^2}{N_U^2} \\ = |D_N(2\pi f\Delta_x(\phi,\theta))|^2\,|D_M(2\pi f\Delta_y(\phi,\theta))|^2\,|D_{N_U}(2\pi f\Delta(\varphi))|^2. \tag{47}$$

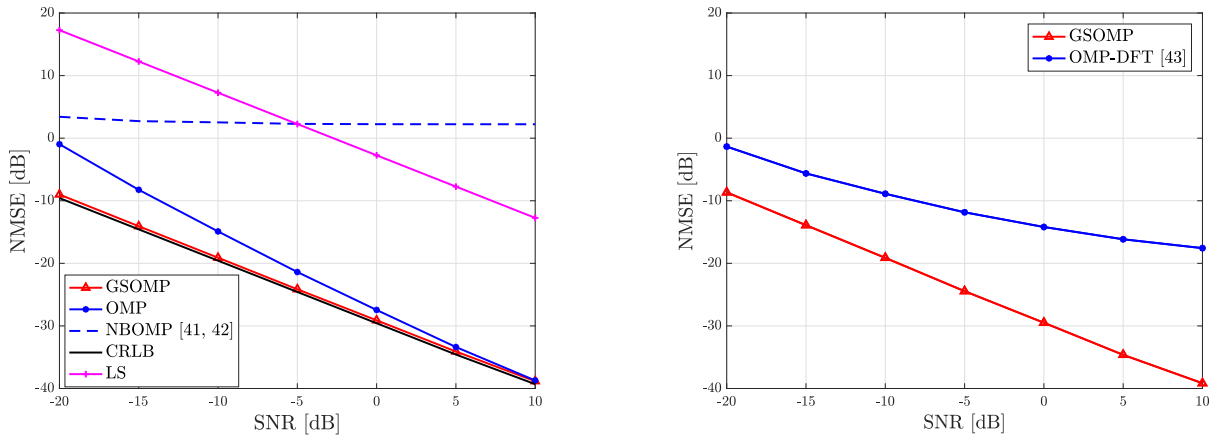

Fig. 6: NMSE versus SNR for a single-antenna user. The OMP, NBOMP, and GSOMP estimators are evaluated under partial training of $N_{\text{beam}} = 0.8N_B$ pilot beams; 40×40-element UPA, $N_{\text{RF}} = 2$, NLoS channel with $L = 3$ paths, $S = 400$ subcarriers, and super-resolution dictionary with $G = 4N_B$.

$\Lambda_{\max} = 50$ dBi [27]. At the user side, we assume omnidirectional antennas. The channel model is then recast by replacing $\mathbf{a}(\phi, \theta, f)$ with $\sqrt{\Lambda(\phi, \theta)}\mathbf{a}(\phi, \theta, f)$ [49].

The other simulation parameters are summarized in Table II.

A. Channel Estimation

1) Single-Antenna User: Our performance metric is the normalized mean-square error (NMSE) versus the average receive SNR. The NMSE is defined as

$$\text{NMSE} \triangleq \frac{1}{|\mathcal{S}|} \sum_{s \in \mathcal{S}} \mathbb{E}\left\{ \left\| \mathbf{h}[s] - \hat{\mathbf{h}}[s] \right\|^2 / \|\mathbf{h}[s]\|^2 \right\}, \qquad (56)$$

where $\hat{\mathbf{h}}[s]$ denotes the estimate of the corresponding estimator. The NMSE is computed numerically over 100 channel realizations. The complex path gains $\{\beta_l(f_s)\}_{l=1}^L$ are generated as $\mathcal{CN}(0, \sigma_\beta^2)$, with $\sigma_\beta^2 = 10^{-9}$, i.e., -90 dB, modeling the high path attenuation at THz frequencies [23].[5] The average receive SNR is then calculated as $\text{SNR} = \sigma_\beta^2 P_p / P_n$, where $P_p = P_t/|\mathcal{S}|$ is the power per pilot subcarrier, and $P_n = \Delta B \sigma^2$ is the noise power at each subcarrier, with $\Delta B \approx B/S$ being the subcarrier spacing.

In the first numerical experiment, we compare the following estimation schemes:

- The LS scheme of Section IV-B under full training, i.e., $N_{\text{beam}} = N_B$.
- The narrowband OMP-based estimator (NBOMP) with a frequency-flat dictionary [44], [45].
- The OMP-based estimator, but with the wideband dictionary of Section IV-D1.
- The proposed GSOMP-based estimator and its CRLB.

The NMSE metrics for the LS method and the CRLB are computed using (31) and (43) in the numerator of (56), respectively. The NMSE attained by each scheme is depicted in Fig. 6(a). As we observe, the NMSE of the LS method is prohibitively high since it scales linearly with the number of BS antennas. Likewise, the NBOMP exhibits a very poor performance since it neglects the spatial-wideband effect. Moreover, the OMP-based estimator fails to successfully recover the common support in the low SNR regime, hence resulting in significant estimation errors. On the other hand, the proposed GSOMP-based estimator accurately detects the common support of the channel gain vectors for all SNR values ranging from -15 dB to 10 dB, and thus attains the CRLB.

Next, we focus on the state-of-the-art of estimation techniques based on the OMP. To this end, we distinguish the work in [46], which proposed a *nonuniform* dictionary and an RF pilot beam design based on the DFT for a narrowband system with ULAs; henceforth, we will refer to this scheme as OMP-DFT. Here, we extend the aforementioned design to the UPA case with spatial-wideband effects, and compare it with our proposed method. As we see from Fig. 6(b), the GSOMP outperfoms the OMP-DFT. The poor performance of the OMP-DFT stems from the fact that the dictionary and RF pilot beams become highly correlated for a large number of BS antennas and high SNR values. To see this, recall that the dictionary resembles a DFT matrix. Consequently, the product of the DFT-based pilot combiner and the dictionary tends to have multiple close-to-zero columns, thereby destroying the incoherence of the equivalent sensing matrix.

2) Multi-Antenna User: We now investigate how multiple user antennas affect the channel estimation performance at the BS. In order to have a fair comparison between the single-antenna and multi-antenna user cases, we fix the total number of antennas to $N_B N_U = 160$, and consider an 20×20-element UPA at the BS and an 4-element ULA at the user.[6] For $\varphi \sim \mathcal{U}(-\pi/2, \pi/2)$, the continuous spatial frequency $\omega = 1/2 \sin\varphi$ lies in the interval $[-1/2, 1/2]$. Thus, the user's dictionary consists of the spatial frequencies $\{\bar{\omega}(p) = p/G^u, p = -(G^u - 1)/2, \ldots, (G^u - 1)/2\}$. The

[5] The path gains are generated in this way so that we have a single average SNR over the OFDM subcarriers.

[6] In this way, the overhead of partial training, $0.8N_B N_U$, is kept fixed too.

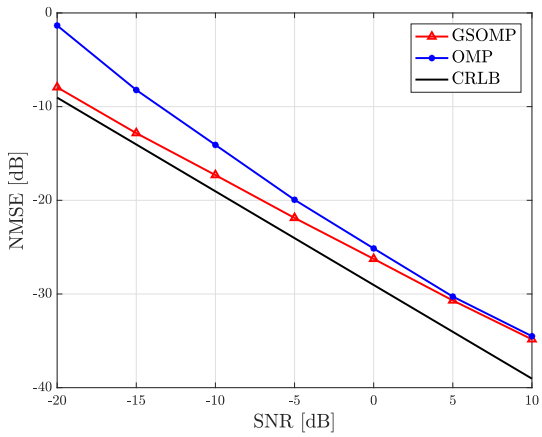

Fig. 7: NMSE versus SNR for a user with an 4-element ULA; 20×20-element UPA, $N_{\text{RF}}=2$, NLoS channel with $L=3$ paths, $S=400$ subcarriers, and super-resolution dictionaries with $G=4N_B$ and $G^u=4N_U$.

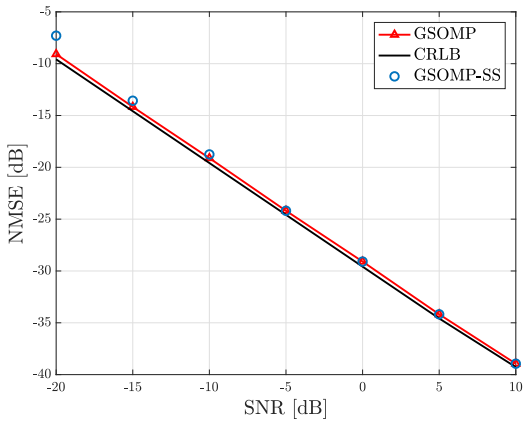

Fig. 8: NMSE versus SNR for a single-antenna user. In GSOMP-SS, one pilot subcarrier per 50 subcarriers is used to detect the common support; 40×40-element UPA, $N_{\text{RF}}=2$, NLoS channel with $L=3$ paths, and $S=400$ subcarriers.

elements of the pilot RF beamformers $\{\mathbf{v}_i\}$ are selected from the set $\{-1/\sqrt{N_U},1/\sqrt{N_U}\}$ with equal probability.

The NMSE is computed by replacing $\mathbf{h}[s]$ and $\hat{\mathbf{h}}[s]$ in (56) with $\text{vec}(\mathbf{H}[s])$ and $\text{vec}(\hat{\mathbf{H}}[s])$, respectively. The MSE of the LS scheme (31) is the same as in the single-antenna user case since we have kept fixed the total number of antennas. Figure 7 depicts the performance of the GSOMP and OMP. As observed, there is a slight increase in the NMSE compared to the single-antenna user case, i.e., Fig. 6(a). Furthermore, this increase becomes significant in the high SNR regime, but yet, the proposed estimator outperforms the OMP for low and moderate SNR values. The performance degradation is because the equivalent sensing matrices $\{\mathbf{\Phi}_s\}_{s=0}^{S-1}$ have higher total coherence compared to the single-antenna user case, which is defined for each matrix $\mathbf{\Phi}_s$ as [46]

$$\mu(\mathbf{\Phi}_s)\triangleq\sum_{i=1}^{GG^u}\sum_{j=1,j\neq i}^{GG^u}\frac{|\mathbf{\Phi}_s^H(i)\mathbf{\Phi}_s(j)|}{\|\mathbf{\Phi}_s(i)\|\|\mathbf{\Phi}_s(j)\|}. \tag{57}$$

It is worth pointing out that different pilot beam designs might change the performance of the estimators, which hinges on the coherence of the equivalent sensing matrices $\{\mathbf{\Phi}_s\}_{s=0}^{S-1}$.

3) Subcarrier Selection: In the previous experiments, we assumed that the GSOMP estimator employs all the subcarriers, i.e., $|\mathcal{S}|=400$, to estimate the common support of the channel gain vectors $\{\boldsymbol{\beta}[s]\}_{s=0}^{S-1}$. However, this might lead to a very high computation burden. Thus, we can employ only a set of successive subcarriers to detect the common support, i.e., steps $2-8$ of Algorithm 2, and then use this support to estimate the channel at every subcarrier $s\in\mathcal{S}$, which corresponds to step 9 of Algorithm 2. We refer to this scheme as GSOMP with subcarrier selection (GSOMP-SS). From Fig. 8, we observe that we can accurately estimate the uplink channel in the moderate SNR regime by employing only a small number of pilot subcarriers in the common support detection steps. Note, though, that using one subcarrier per 50 pilot subcarriers slightly increases the NMSE in the low SNR regime.

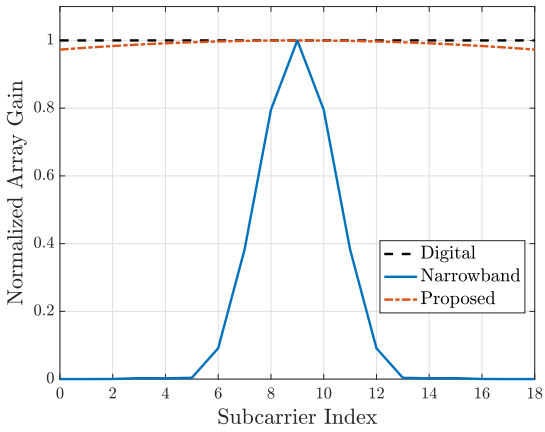

Fig. 9: Normalized array gain for an 100×100-element UPA. In the proposed scheme, $N_{\text{sb}}M_{\text{sb}}-1=99$ TTD elements are employed; LoS channel, $(\phi_0,\theta_0)=(\pi/4,\pi/3)$, and $S=18$ subcarriers.

B. Hybrid Combining for Single-Antenna Users

1) Achievable Rate with Perfect CSI: We start the performance assessment of our combiner by considering a LoS channel. In this case, the complex path gain is given by $\beta_0(f)=\alpha_0(f)e^{-j2\pi f_c\tau_0}$, where $\tau_0=\texttt{D}/c$ is the ToA of the LoS path, and $\alpha_0(f)$ is specified according to (8). For each channel realization, perfect knowledge of the DoA is assumed at the BS, which can be acquired using the GSOMP estimator. We also consider the following cases:

- A fully-digital architecture, where the BS employs the frequency-selective combiner $\mathbf{a}(\phi_0,\theta_0,f)/\sqrt{N_B}$.
- A hybrid architecture, where the BS uses the narrowband combiner $\mathbf{a}(\phi_0,\theta_0,0)/\sqrt{N_B}$.
- A hybrid architecture, where the proposed combiner (22) is used, with $N_{\text{sb}}=10$ and $M_{\text{sb}}=10$ virtual subarrays.

The normalized array gain is plotted in Fig. 9, where we see that our combiner atttains approximately the maximum gain over the entire signal bandwidth of $B=40$ GHz. Next, we

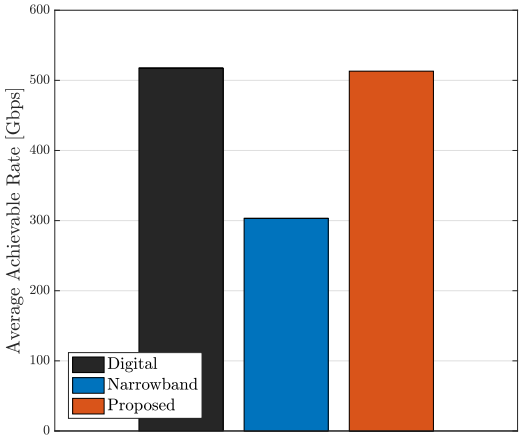

Fig. 10: Average achievable rate under perfect CSI for a LoS channel; single-antenna user, 100×100-element UPA, 99 TTD elements in the proposed scheme, and $S = 18$ subcarriers.

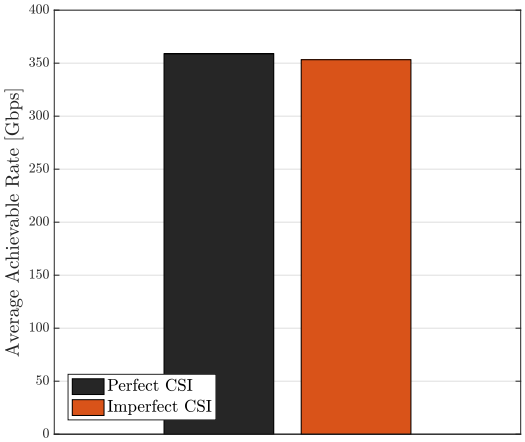

Fig. 11: Average achievable rate under imperfect CSI for a NLoS channel with $L = 2$ paths; single-antenna user, 100×100-element UPA, 99 TTD elements per RF chain, and $S = 400$ subcarriers.

focus on the average achievable rate, which is calculated as

$$R = \sum_{s=1}^{S} \Delta B \mathbb{E}\left\{\log_2\left(1 + \frac{P_d|\mathbf{f}_{\text{RF}}^H \mathbf{h}[s]|^2}{\Delta B \sigma^2}\right)\right\}, \quad (58)$$

where $P_d = P_t/S$ is the power per subcarrier, and $\mathbf{f}_{\text{RF}}$ denotes the corresponding combiner. The results are given in Fig. 10. Specifically, the achievable rates are 517 Gbps, 514 Gbps, and 303 Gbps for the digital, proposed, and narrowband schemes, respectively. Thus, the proposed combiner performs very close to the fully-digital scheme, while offering a 40% gain with respect to the narrowband combiner. Additionally, this is done by employing only $N_{\text{sb}}M_{\text{sb}} - 1 = 99$ TTD elements for an 100×100-element UPA, which yields an excellent trade-off between hardware complexity and performance. Lastly, note that transmission rates at least $R = 0.5$ Tbps at $\mathtt{D} = 15$ meters can be achieved through an 100×100-element UPA, which would not be feasible with an equivalent ULA under a footprint constraint.

2) Achievable Rate with Imperfect CSI: We now evaluate the average achievable rate attained by the proposed combiner along with the GSOMP-based estimator. To this end, we consider a NLoS multi-path channel. The complex path gain of the lth NLoS path is $\beta_l(f) = \alpha_l(f)e^{-j2\pi f_c \tau_l}$, where τ_l is the ToA, and $\alpha_l(f)$ is calculated according to (10) assuming $\phi_{i,l} \sim \mathcal{U}(-\pi/2, \pi/2)$. Under imperfect CSI, the BS treats the channel estimate as the true channel, and combines the received signal with the maximum-ratio combiner $\hat{\mathbf{h}}[s]/\|\hat{\mathbf{h}}[s]\|$. Let $\mathbf{h}[s] = \hat{\mathbf{h}}[s] - \mathbf{e}[s]$, with $\mathbf{e}[s]$ denoting the channel estimation error for the sth subcarrier. The combined signal for the sth subcarrier is then written as

$$\begin{aligned} y[s] &= \sqrt{P_d}\|\hat{\mathbf{h}}[s]\|x[s] - \sqrt{P_d}\frac{\hat{\mathbf{h}}^H[s]\mathbf{e}[s]}{\|\hat{\mathbf{h}}[s]\|}x[s] + \frac{\hat{\mathbf{h}}^H[s]}{\|\hat{\mathbf{h}}[s]\|}\mathbf{n}[s] \\ &= \sqrt{P_d}\|\hat{\mathbf{h}}[s]\|x[s] + n_{\text{eff}}[s], \end{aligned} \quad (59)$$

where $n_{\text{eff}}[s] = (-\sqrt{P_d}\hat{\mathbf{h}}^H[s]\mathbf{e}[s]x[s] + \hat{\mathbf{h}}^H[s]\mathbf{n}[s])/\|\hat{\mathbf{h}}[s]\|$ is the effective noise. Unfortunately, it is challenging to derive an achievable rate of channel model (59) since the effective noise is correlated with the desired signal. Nevertheless, as shown in the previous numerical results, the channel estimation error is small. Hence, it is reasonably assumed that, conditioned on the channel estimates, the effective noise is uncorrelated with the desired signal. Then, we obtain the following approximation for the equivalent SNR at the sth subcarrier [47]

$$\text{SNR}_{\text{eq}}[s] \approx \frac{P_d\|\hat{\mathbf{h}}[s]\|^2}{\Delta B\sigma^2 + P_d\hat{\mathbf{h}}^H[s]\mathbf{R}_{\mathbf{e}[s]}\hat{\mathbf{h}}[s]/\|\hat{\mathbf{h}}[s]\|^2}, \quad (60)$$

where $\mathbf{R}_{\mathbf{e}[s]} \triangleq \mathbb{E}\{\mathbf{e}[s]\mathbf{e}^H[s]\}$. The corresponding average achievable rate under imperfect CSI is then [47]

$$R \approx \sum_{s=1}^{S} \Delta B \mathbb{E}\left\{\log_2\left(1 + \text{SINR}_{\text{eq}}[s]\right)\right\}. \quad (61)$$

A closed-form expression for $\mathbf{R}_{\mathbf{e}[s]}$ can be derived by assuming perfect recovery of the common support of the channel gain vectors. More specifically, from the CRLB analysis, we have that the error $\mathbf{e}[s] \triangleq \bar{\mathbf{A}}_s(\mathcal{I})\left(\hat{\tilde{\boldsymbol{\beta}}}[s] - \tilde{\boldsymbol{\beta}}[s]\right)$ is distributed as $\mathcal{CN}\left(\mathbf{0}, \mathbf{R}_{\mathbf{e}[s]}\right)$, where $\mathbf{R}_{\mathbf{e}[s]} = \bar{\mathbf{A}}_s(\mathcal{I})\mathbf{I}^{-1}\left(\tilde{\boldsymbol{\beta}}[s]\right)\bar{\mathbf{A}}_s^H(\mathcal{I})$. Figure 11 depicts the average achievable rate under perfect and imperfect CSI. In the imperfect CSI case, the common support of the channel gain vectors is computed by the GSOMP-based estimator. As observed from Fig. 11, the average achievable rate attained by the proposed channel estimator approaches that of the perfect CSI case.

C. Hybrid SVD Transmission for Multi-Antenna Users

In this section, we consider a multi-antenna user. As previously shown, we can accurately estimate the channel using the GSOMP-based estimator, and hence perfect CSI is assumed. To have a fair comparison between the single-antenna and multi-antenna user cases, we fix the number of antennas to $N_U N_B = 100 \times 100$, and we consider an 100×50-element UPA at the BS and an 2-element ULA at the user. Due to the small user array size, we assume a fully-digital array at the user, where $N_{\text{RF}}^u = N_U = 2$. Subsequently, we compare the following transmission schemes:

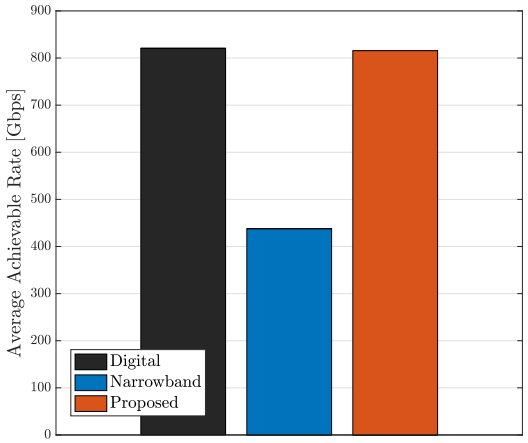

Fig. 12: Average achievable rate a for a NLoS channel with $L = 2$ paths; multi-antenna user with an 2-element ULA, 100×50-element UPA, 49 TTD elements per RF chain, and $S = 400$ subcarriers.

- Digital: the combiner $\mathbf{F}[s]$ and precoder $\mathbf{B}[s]$ are designed using the SVD of the channel $\mathbf{H}[s]$.
- Proposed: the wideband RF combiner $\mathbf{F}_{\text{RF}}[s]$ implements the scaled matrix $\mathbf{H}_B(f)/\sqrt{N_B}$, defined in (48), using TTD and virtual array partition. The baseband combiner $\mathbf{F}_{\text{BB}}[s]$ and precoder $\mathbf{B}[s]$ are then designed using the SVD of the effective channel $\mathbf{F}_{\text{RF}}^H[s]\mathbf{H}[s]$.
- Narrowband: the frequency-flat RF combiner $\mathbf{F}_{\text{RF}}$ implements the scaled matrix $\mathbf{H}_B(0)/\sqrt{N_B}$ defined in (48). The baseband combiner $\mathbf{F}_{\text{BB}}[s]$ and precoder $\mathbf{B}[s]$ are then designed based on the SVD of the effective channel $\mathbf{F}_{\text{RF}}^H\mathbf{H}[s]$.

The average achievable rate is calculated as

$$R = \sum_{s=0}^{S-1} \sum_{n=0}^{N_{\text{RF}}^u} \Delta B \mathbb{E}\left\{ \log_2 \left(1 + \frac{p_{n,s}\sigma_n^2(\mathbf{F}^H[s]\mathbf{H}[s]\mathbf{B}[s])}{\Delta B \sigma^2} \right) \right\}, \tag{62}$$

where the set $\{p_{n,s}\}$ of powers is calculated using the waterfilling power allocation algorithm, and $\sigma_n(\cdot)$ denotes the nth singular value of the input matrix. From Fig. 12, we validate the effectiveness of the proposed TTD-based method, which performs close to the fully-digital transmission scheme. More importantly, the deployment of a few antennas at the user side along with waterfilling power allocation boosts the average achievable rate compared to the single-antenna user case, which enables rates much higher than $R = 0.5$ Tbps at a distance $\mathtt{D} = 15$ m. Another benefit of having multiple user antennas is the reduction of the BS array size, which permits combating the spatial-wideband effect with a small number of TTD elements. In particular, for the 100×50-element UPA under consideration, we have used $N_{\text{sb}} = 10$ and $M_{\text{sb}} = 5$ virtual subarrays, resulting in $N_{\text{sb}}M_{\text{sb}} - 1 = 49$ TTD elements.

D. Near-Field Considerations

In the far-field region, the spherical wavefront degenerates to a plane wavefront, which allows the use of the parallel-ray approximation to derive the array response vector (7). Due to the large array aperture of THz massive MIMO, though, near-field considerations are of particular interest. Recall that near-field refers to distances smaller than the Fraunhofer distance $\mathtt{D}_f \triangleq 2\mathtt{D}_{\max}^2/\lambda$, where $\mathtt{D}_{\max}$ is the maximum dimension of the antenna array, and λ is the carrier wavelength. For a UPA with $N = M$, we have $\mathtt{D}_{\max}^2 = 2(N-1)^2d^2$, i.e., length of its diagonal dimension, which leads to $\mathtt{D}_f = (N-1)^2\lambda$ for a half-wavelength spacing. Then, for $f_c = 300$ GHz and an 100×100-element UPA, $\mathtt{D}_f \approx 9.8$ meters. As a result, the plane wave assumption may not hold anymore in small distances from the BS [50]. In this case, a spherical wavefront is a more appropriate model [51]. Under this model, the array response matrix, $\mathbf{A}(\phi, \theta, f) \in \mathbb{C}^{M \times N}$, of the BS is defined as

$$[\mathbf{A}(\phi, \theta, f)]_{m,n} \triangleq e^{-j2\pi(f_c+f)\frac{\mathtt{D}_{mn}(\phi,\theta)}{c}}, \tag{63}$$

where $\mathtt{D}_{mn}(\phi, \theta) = \left((x - nd)^2 + (y - md)^2 + z^2\right)^{1/2}$ is the distance between the (n, m)th BS antenna and the scatterer with coordinates (x, y, z); $x \triangleq \mathtt{D}\cos\phi\sin\theta$, $y \triangleq \mathtt{D}\sin\phi\sin\theta$, and $z \triangleq \mathtt{D}\cos\theta$, where $\mathtt{D}$ denotes the distance from the $(0, 0)$th BS antenna. The array response vector is then obtained as $\mathbf{a}(\phi, \theta, f) = \text{vec}(\mathbf{A}(\phi, \theta, f))$. We now calculate the average achievable rate for the TTD-based combiner (22) under the plane and spherical wave models. The combiner is designed assuming a plane wavefront in both cases. From Fig. 13, a very good match between the two models is observed even for distances smaller than the Fraunhofer distance. Thus, the proposed combiner can be used at near-field distances without incurring a significant rate loss. However, we stress that a comprehensive study of the near-field effects under different array arrangements and sizes is left for future work.

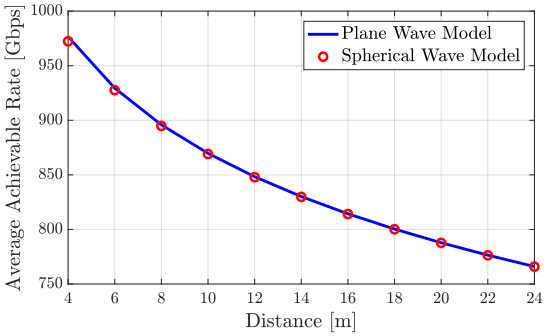

Fig. 13: Average achievable rate of the TTD-based wideband combiner for a LoS channel; single-antenna user, and 100×100-element UPA.

VII. Conclusions

We have proposed a solution to the channel estimation and hybrid combining problems in wideband THz massive MIMO. Specifically, we first derived the THz channel model with SFW effects for a UPA at the BS and a single-antenna user. We then showed that standard narrowband combining leads to severe reduction of the array gain due to beam squint. To tackle this problem, we introduced a novel TTD-based wideband combiner with a low-complexity implementation due to the virtual subarray rationale. We next proposed a CS algorithm

along with a wideband dictionary to acquire reliably the CSI with reduced training overhead under the spatial-wideband effect. To study the performance of the proposed schemes, we derived the CRLB and computed the achievable rate under imperfect CSI. We also extended our analysis to the multi-antenna user case, and conducted numerical results.

Simulations demonstrated that our design provides nearly *beam squint-free* operation, as well as enables accurate CSI acquisition even in the low SNR regime. Regarding the insights drawn from our study, the deployment of multiple antennas at the user can alleviate the spatial-wideband effect by reducing the BS' array size, whilst keeping constant the total number of antennas. As a result, the TTD-based wideband array can offer the power gain required to compensate for the very high propagation losses at THz bands. Additionally, in the case of multi-path propagation, it has been shown that SVD-based transmission can boost the performance and offer rates higher than half terabit per second over a distance of several meters. In conclusion, wideband massive MIMO will play a pivotal role in future THz wireless networks.

Regarding future work, it would be interesting to study the performance of wideband THz massive MIMO under hardware impairments, as well as investigate the beam tracking problem in high-mobility scenarios. Moreover, it would be interesting to compare OFDM with SC-FDE, and derive an analytical expression for the PAPR metric.

APPENDIX A

For the normalized array gain, we have that

$$\begin{aligned}&\frac{|\mathbf{a}^H(\phi,\theta,0)\mathbf{a}(\phi,\theta,f)|}{N_B} = \\ &= \frac{|\left(\mathbf{a}_x(\phi,\theta,0)^H \otimes \mathbf{a}_y(\phi,\theta,0)^H\right)\left(\mathbf{a}_x(\phi,\theta,f)\otimes \mathbf{a}_y(\phi,\theta,f)\right)|}{NM} \\ &= \frac{|\left(\mathbf{a}_x(\phi,\theta,0)^H\mathbf{a}_x(\phi,\theta,f)\right)\left(\mathbf{a}_y^H(\phi,\theta,0)\mathbf{a}_y(\phi,\theta,f)\right)|}{NM}.\end{aligned}$$

Then, it holds

$$\begin{aligned}\frac{|\mathbf{a}_x(\phi,\theta,0)^H\mathbf{a}_x(\phi,\theta,f)|}{N} &= \frac{1}{N}\left|\sum_{n=0}^{N-1} e^{-j2\pi f n\frac{d}{c}\sin\theta\cos\phi}\right| \\ &= \frac{1}{N}\left|\frac{1-e^{-j2\pi f N\frac{d}{c}\sin\theta\cos\phi}}{1-e^{-j2\pi f\frac{d}{c}\sin\theta\cos\phi}}\right| \\ &= \frac{1}{N}\left|\frac{\sin\left(N\pi f\Delta_x\right)}{\sin\left(\pi f\Delta_x\right)}\right| \\ &= |D_N(2\pi f\Delta_x)|,\end{aligned}$$

where $\Delta_x = \frac{d}{c}\sin\theta\cos\phi$. Likewise, we get

$$\frac{|\mathbf{a}_y(\phi,\theta,0)^H\mathbf{a}_y(\phi,\theta,f)|}{M} = |D_M(2\pi f\Delta_y)|,$$

where $\Delta_y = \frac{d}{c}\sin\theta\sin\phi$, which yields the desired result.

APPENDIX B

Using the identity $\mathbf{a}_x\otimes\mathbf{a}_y = \text{vec}\left(\mathbf{a}_y\mathbf{a}_x^T\right)$, we have

$$\begin{aligned}&\mathbf{A}(\phi,\theta,f) \triangleq \mathbf{a}_y(\phi,\theta,f)\mathbf{a}_x^T(\phi,\theta,f) \\ &= \begin{bmatrix}\mathbf{a}_{y,1}(\phi,\theta,f)\\ \vdots \\ \mathbf{a}_{y,M_{\text{sb}}}(\phi,\theta,f)\end{bmatrix}\left[\mathbf{a}_{x,1}^T(\phi,\theta,f),\cdots,\mathbf{a}_{x,N_{\text{sb}}}^T(\phi,\theta,f)\right] \\ &= \begin{bmatrix}\mathbf{A}_{11}(\phi,\theta,f) & \cdots & \mathbf{A}_{1N_{\text{sb}}}(\phi,\theta,f)\\ \mathbf{A}_{21}(\phi,\theta,f) & \cdots & \mathbf{A}_{1N_{\text{sb}}}(\phi,\theta,f)\\ \vdots & \ddots & \vdots \\ \mathbf{A}_{M_{\text{sb}}1}(\phi,\theta,f) & \cdots & \mathbf{A}_{M_{\text{sb}}N_{\text{sb}}}(\phi,\theta,f)\end{bmatrix},\end{aligned} \tag{64}$$

where $\mathbf{A}_{mn}(\phi,\theta,f) \triangleq \mathbf{a}_{y,m}(\phi,\theta,f)\mathbf{a}_{x,n}^T(\phi,\theta,f)$. We also have that

$$\begin{aligned}&\mathbf{A}_{mn}(\phi,\theta,f) = \mathbf{a}_{y,m}(\phi,\theta,f)\mathbf{a}_{x,n}^T(\phi,\theta,f) \\ &= e^{-j2\pi(n-1)\tilde{N}(f_c+f)\Delta_x - j2\pi(m-1)\tilde{M}(f_c+f)\Delta_y}\mathbf{A}_{11}(\phi,\theta,f).\end{aligned}$$

Using the above relationships, we can write

$$\mathbf{A}(\phi,\theta,0)\odot\mathbf{T}[s] = \mathbf{v}_y\mathbf{v}_x^T, \tag{65}$$

where

$$\mathbf{v}_x = \left[e^{-j2\pi(n-1)\tilde{N}(f_c+f)\Delta_x}\mathbf{a}_{x,1}(\phi,\theta,0)\right]_{n=1}^{N_{\text{sb}}}, \tag{66}$$

and

$$\mathbf{v}_y = \left[e^{-j2\pi(m-1)\tilde{M}(f_c+f)\Delta_y}\mathbf{a}_{y,1}(\phi,\theta,0)\right]_{m=1}^{M_{\text{sb}}}. \tag{67}$$

Now consider a path with array response $\mathbf{a}^H(\phi,\theta,f)$. Then,

$$\begin{aligned}&\mathbf{f}_{\text{RF}}^H\mathbf{a}(\phi,\theta,f) = \\ &= \frac{1}{\sqrt{N_B}}\text{vec}^H(\mathbf{A}(\phi,\theta,0)\odot\mathbf{T}[s])\mathbf{a}(\phi,\theta,f) \\ &= \frac{\sqrt{N_B}}{N_B}\left(\mathbf{v}_x^H\otimes\mathbf{v}_y^H\right)\left(\mathbf{a}_x(\phi,\theta,f)\otimes\mathbf{a}_y(\phi,\theta,f)\right) \\ &= \frac{\sqrt{N_B}}{N_B}\left(\mathbf{v}_x^H\mathbf{a}_x(\phi,\theta,f)\right)\left(\mathbf{v}_y^H\mathbf{a}_y(\phi,\theta,f)\right) \\ &= \sqrt{N_B}\frac{\mathbf{a}_{x,1}^H(\phi,\theta,0)\mathbf{a}_{x,1}(\phi,\theta,f)}{\tilde{N}}\frac{\mathbf{a}_{y,1}^H(\phi,\theta,0)\mathbf{a}_{y,1}(\phi,\theta,f)}{\tilde{M}}.\end{aligned}$$

As a result, we obtain (23) in Proposition 1.

REFERENCES

[1] T. S. Rappaport *et al.*, "Wireless communications and applications above 100 GHz: Opportunities and challenges for 6G and beyond," *IEEE Access*, vol. 7, pp. 78729-78757, 2019.

[2] T. Kürner, "Towards future THz communications systems," *Terahertz Sci. Technol.*, vol. 5, no. 1, pp. 11–17, 2012.

[3] J. Zhang *et al.*, "Prospective multiple antenna technologies for beyond 5G," *IEEE J. Sel. Areas Commun.*, vol. 38, no. 8, pp. 1637–1660, Aug. 2020.

[4] H. J. Song and T. Nagatsuma, "Present and future of terahertz communications," *IEEE Trans. THz Sci. Technol.*, vol. 1, no. 1, pp. 256–263, Sep. 2011.

[5] B. Wang, F. Gao, S. Jin, H. Lin, and G. Y. Li, "Spatial- and frequency-wideband effects in millimeter wave massive MIMO systems," *IEEE Trans. Signal Process.*, vol. 66, no. 13, pp. 3393-3406, Jul. 2018.

[6] B. Wang *et al.*, "Spatial-wideband effect in massive MIMO with application in mmWave systems," *IEEE Commun. Mag.*, vol. 56, no. 12, pp. 134-141, Dec. 2018.

[7] R. J. Mailloux, *Phased Array Antenna Handbook*. Norwood, MA, USA: Artech House, 2005.

[8] B. Peng, S. Wesemann, K. Guan, W. Templ, and T. Kürner, "Precoding and detection for broadband single carrier terahertz massive MIMO systems using LSQR algorithm," *IEEE Trans. Wireless Commun.*, vol. 18, no. 2, pp. 1026-1040, Feb. 2019.

[9] F. Sohrabi and W. Yu, "Hybrid analog and digital beamforming for mmWave OFDM large-scale antenna arrays," *IEEE J. Sel. Areas Commun.*, vol. 35, no. 7, pp. 1432-1443, July 2017.

[10] J. P. González-Coma, W. Utschick, and L. Castedo, "Hybrid LISA for wideband multiuser millimeter-wave communication systems under beam squint," *IEEE Trans. Wireless Commun.*, vol. 18, no. 2, pp. 1277-1288, Feb. 2019.

[11] S. Park, A. Alkhateeb, and R. W. Heath, Jr., "Dynamic subarrays for hybrid precoding in wideband mmwave MIMO systems," *IEEE Trans. Wireless Commun.*, vol. 16, no. 5, pp. 2907–2920, May 2017.

[12] L. Kong, S. Han, and C. Yang, "Hybrid precoding with rate and coverage constraints for wideband massive MIMO systems," *IEEE Trans. Wireless Commun.*, vol. 17, no. 7, pp. 4634–4647, July 2018.

[13] M. Cai *et al*, "Effect of wideband beam squint on codebook design in phased-array wireless systems," in *Proc. IEEE GLOBECOM*, Dec. 2016.

[14] X. Liu and D. Qiao, "Space-time block coding-based beamforming for beam squint compensation," *IEEE Wireless Commun. Lett.*, vol. 8, no. 1, pp. 241–244, Feb. 2019.

[15] C. Lin, G. Y. Li, and L. Wang, "Subarray-based coordinated beamforming training for mmWave and sub-THz communications," *IEEE J. Sel. Areas Commun.*, vol. 35, no. 9, pp. 2115-2126, Sept. 2017.

[16] H. Hashemi, T. Chu, and J. Roderick, "Integrated true-time-delay-based ultra-wideband array processing," *IEEE Commun. Mag.*, vol. 46, no. 9, pp. 162–172, Sep. 2008.

[17] J. Tan and L. Dai, "Delay-phase precoding for THz massive MIMO with beam split," in *Proc. IEEE GLOBECOM*, Dec. 2019.

[18] B. Wang, X. Li, F. Gao, and G. Y. Li, "Power leakage elimination for wideband mmWave massive MIMO-OFDM systems: An energy-focusing window approach," *IEEE Trans. Signal Process.*, vol. 67, no. 21, pp. 5479-5494, Nov. 2019.

[19] J. P. González-Coma, J. Rodríguez-Fernández, N. González-Prelcic, L. Castedo, and R. W. Heath, Jr., "Channel estimation and hybrid precoding for frequency selective multiuser mmWave MIMO systems," *IEEE J. Sel. Topics Signal Process.*, vol. 12, no. 2, pp. 353-367, May 2018.

[20] C. Lin and G. Y. Li, "Indoor terahertz communications: How many antenna arrays are needed?," *IEEE Trans. Wireless Commun.*, vol. 14, no. 6, pp. 3097-3107, June 2015.

[21] H. Sarieddeen, M.-S. Alouini, and T. Y. Al-Naffouri, "Terahertz-band ultra-massive spatial modulation MIMO," *IEEE J. Sel. Areas Commun.*, vol. 37, no. 9, pp. 2040-2052, Sept. 2019.

[22] Q. Ma, D. M. W. Leenaerts, and P. G. M. Baltus, "Silicon-based true-time-delay phased array front-ends at Ka-band," *IEEE Trans. Microw. Theory Techn.*, vol. 63, no. 9, pp. 2942–2952, Sep. 2015.

[23] C. Han and Y. Chen, "Propagation modeling for wireless communications in the terahertz band," *IEEE Commun. Mag.*, vol. 56, no. 6, pp. 96-101, June 2018.

[24] C. A. Balanis, *Antenna Theory: Analysis and Design*, John Wiley & Sons, 2012.

[25] D. Tse and P. Viswanath, *Fundamentals of Wireless Communication*. New York, NY, USA: Cambridge Univ. Press, 2005.

[26] A. F. Molisch, "Ultrawideband propagation channels-theory, measurement, and modeling," *IEEE Trans. Veh. Technol.*, vol. 54, no. 5, pp. 1528-1545, Sept. 2005.

[27] A. A. Boulogeorgos, E. N. Papasotiriou, and A. Alexiou, "Analytical performance assessment of THz wireless systems," *IEEE Access*, vol. 7, pp. 11436-11453, 2019.

[28] C. Han, A. O. Bicen, and I. F. Akyildiz, "Multi-ray channel modeling and wideband characterization for wireless communications in the terahertz band," *IEEE Trans. Wireless Commun.*, vol. 14, no. 5, pp. 2402–2412, May 2015.

[29] R. Piesiewicz *et al.*, "Scattering analysis for the modeling of THz communication systems," *IEEE Trans. Antennas Propag.*, vol. 55, no. 11, pp. 3002–3009, Nov. 2007.

[30] C. Lin and G. Y. Li, "Adaptive beamforming with resource allocation for distance-aware multi-user indoor terahertz communications," *IEEE Trans. Commun.*, vol. 63, no. 8, pp. 2985-2995, Aug. 2015.

[31] O. E. Ayach, R. W. Heath, Jr., S. Abu-Surra, S. Rajagopal, and Z. Pi, "The capacity optimality of beam steering in large millimeter wave MIMO systems," in *Proc. IEEE SPAWC*, June 2012, pp. 100-104.

[32] S. M. Perera, A. Madanayake, and R. J. Cintra, "Radix-2 self-recursive sparse factorizations of delay Vandermonde matrices for wideband multi-beam antenna arrays," *IEEE Access*, vol. 8, pp. 25498-25508, 2020.

[33] W. U. Bajwa, J. Haupt, A. M. Sayeed, and R. Nowak, "Compressed channel sensing: a new approach to estimating sparse multipath channels," *Proc. IEEE*, vol. 98, no. 6, pp. 1058-1076, June 2010.

[34] R. Méndez-Rial, C. Rusu, N. González-Prelcic, A. Alkhateeb, and R. W. Heath, Jr., "Hybrid MIMO architectures for millimeter wave communications: Phase shifters or switches?," *IEEE Access*, vol. 4, pp. 247-267, 2016.

[35] R. W. Heath, Jr., N. González-Prelcic, S. Rangan, W. Roh, and A. M. Sayeed, "An overview of signal processing techniques for millimeter wave MIMO systems," *IEEE J. Sel. Topics Signal Process.*, vol. 10, no. 3, pp. 436-453, Apr. 2016.

[36] T. T. Cai and L. Wang, "Orthogonal matching pursuit for sparse signal recovery with noise," *IEEE Trans. Inf. Theory*, vol. 57, no. 7, pp. 4680-4688, July 2011.

[37] L. Harry and V. Trees, *Optimum Array Processing: Detection, Estimation, and Modulation Theory*. John Wiley & Sons, 2002.

[38] A. M. Sayeed, "Deconstructing multi-antenna fading channels," *IEEE Trans. Signal Process.*, vol. 50, no. 10, pp. 2563–2579, Oct. 2002.

[39] H. Xie, F. Gao, S. Zhang, and S. Jin, "A unified transmission strategy for TDD/FDD massive MIMO systems with spatial basis expansion model," *IEEE Trans. Veh. Technol.*, vol. 66, no. 4, pp. 3170-3184, Apr. 2017.

[40] Z. Gao, L. Dai, Z. Wang, and S. Chen, "Spatially common sparsity based adaptive channel estimation and feedback for FDD massive MIMO," *IEEE Trans. Signal Process.*, vol. 63, no. 23, pp. 6169-6183, Dec. 2015.

[41] J. A. Tropp, A. C. Gilbert, and M. J. Strauss, "Algorithms for simultaneous sparse approximation—part I: Greedy pursuit," *Signal Process.*, vol. 86, no. 3, pp. 572–588, 2006.

[42] J. A. Tropp and A. C. Gilbert, "Signal recovery from random measurements via orthogonal matching pursuit," *IEEE Trans. Inf. Theory*, vol. 53, no. 12, pp. 4655–4666, Dec. 2007.

[43] S. M. Kay, *Fundamentals of Statistical Processing: Estimation Theory*, vol. 1. Upper Saddle River, NJ, USA: Prentice-Hall, 1993.

[44] J. Lee, G. Gil, and Y. H. Lee, "Exploiting spatial sparsity for estimating channels of hybrid MIMO systems in millimeter wave communications," in *Proc. IEEE GLOBECOM*, Dec. 2014, pp. 3326-3331.

[45] Y. You, L. Zhang, and M. Liu, "IP aided OMP based channel estimation for millimeter wave massive MIMO communication," in *Proc. IEEE WCNC*, Apr. 2019.

[46] J. Lee, G. Gil, and Y. H. Lee, "Channel estimation via orthogonal matching pursuit for hybrid MIMO systems in millimeter wave communications," *IEEE Trans. Commun.*, vol. 64, no. 6, pp. 2370-2386, June 2016.

[47] T. L. Marzetta, E. G. Larsson, H. Yang, and H. Q. Ngo, *Fundamentals of Massive MIMO*. Cambridge, UK: Cambridge University Press, 2016.

[48] Q. Nadeem, A. Kammoun, and M.-S. Alouini, "Elevation beamforming with full dimension MIMO architectures in 5G systems: A tutorial," *IEEE Commun. Surveys Tuts.*, vol. 21, no. 4, pp. 3238-3273, Jul. 2019.

[49] O. E. Ayach, S. Rajagopal, S. A.-Surra, Z. Pi, and R. W. Heath, Jr., "Spatially sparse precoding in millimeter wave MIMO systems," *IEEE Trans. Wireless Commun.*, vol. 13, no. 3, pp. 1499-1513, Mar. 2014.

[50] M. Matthaiou, P. de Kerret, G. K. Karagiannidis, and J. A. Nossek, "Mutual information statistics and beamforming performance analysis of optimized LoS MIMO systems," *IEEE Trans. Commun.*, vol. 58, no. 11, pp. 3316-3329, Nov. 2010.

[51] F. Bøhagen, P. Orten, and G. E. Øien, "On spherical vs. plane wave modeling of line-of-sight MIMO channels," *IEEE Trans. Commun.*, vol. 57, no. 3, pp. 841-849, Mar. 2009.

Konstantinos Dovelos received the Diploma (M.Eng.) degree in electrical and computer engineering from the Aristotle University of Thessaloniki, Greece, in 2016. He is currently pursuing the Ph.D. degree with the Department of Information and Communication Technologies at Universitat Pompeu Fabra (UPF), Spain. His research interests span massive MIMO, mmWave/THz communications, channel estimation, signal processing, applied electromagnetics, and intelligent reflecting surfaces.

Michail Matthaiou (S'05–M'08–SM'13) was born in Thessaloniki, Greece in 1981. He obtained the Diploma degree (5 years) in Electrical and Computer Engineering from the Aristotle University of Thessaloniki, Greece, in 2004. He then received the M.Sc. (with distinction) in Communication Systems and Signal Processing from the University of Bristol, U.K. and Ph.D. degrees from the University of Edinburgh, U.K. in 2005 and 2008, respectively. From September 2008 through May 2010, he was with the Institute for Circuit Theory and Signal Processing, Munich University of Technology (TUM), Germany working as a Postdoctoral Research Associate. He is currently a Professor of Communications Engineering and Signal Processing and Deputy Director of the Centre for Wireless Innovation (CWI) at Queen's University Belfast, U.K. after holding an Assistant Professor position at Chalmers University of Technology, Sweden. His research interests span signal processing for wireless communications, beyond massive MIMO, intelligent reflecting surfaces, mm-wave/THz systems, and deep learning for communications.

Dr. Matthaiou and his coauthors received the IEEE Communications Society (ComSoc) Leonard G. Abraham Prize in 2017. He currently holds the ERC Consolidator Grant BEATRICE (2021-2026) focused on the interface between information and electromagnetic theories. He was awarded the prestigious 2018/2019 Royal Academy of Engineering/The Leverhulme Trust Senior Research Fellowship and also received the 2019 EURASIP Early Career Award. His team was also the Grand Winner of the 2019 Mobile World Congress Challenge. He was the recipient of the 2011 IEEE ComSoc Best Young Researcher Award for the Europe, Middle East and Africa Region and a co-recipient of the 2006 IEEE Communications Chapter Project Prize for the best M.Sc. dissertation in the area of communications. He has co-authored papers that received best paper awards at the 2018 IEEE WCSP and 2014 IEEE ICC and was an Exemplary Reviewer for IEEE COMMUNICATIONS LETTERS for 2010. In 2014, he received the Research Fund for International Young Scientists from the National Natural Science Foundation of China. He is currently the Editor-in-Chief of Elsevier Physical Communication, a Senior Editor for IEEE WIRELESS COMMUNICATIONS LETTERS and an Associate Editor for the IEEE JSAC SERIES ON MACHINE LEARNING FOR COMMUNICATIONS AND NETWORKS.

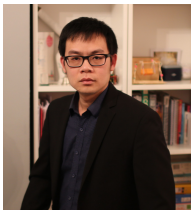

Hien Quoc Ngo received the B.S. degree in electrical engineering from the Ho Chi Minh City University of Technology, Vietnam, in 2007, the M.S. degree in electronics and radio engineering from Kyung Hee University, South Korea, in 2010, and the Ph.D. degree in communication systems from Linköping University (LiU), Sweden, in 2015. In 2014, he visited the Nokia Bell Labs, Murray Hill, New Jersey, USA. From January 2016 to April 2017, Hien Quoc Ngo was a VR researcher at the Department of Electrical Engineering (ISY), LiU. He was also a Visiting Research Fellow at the School of Electronics, Electrical Engineering and Computer Science, Queen's University Belfast, UK, funded by the Swedish Research Council.

Hien Quoc Ngo is currently a Lecturer at Queen's University Belfast, UK. His main research interests include massive (large-scale) MIMO systems, cell-free massive MIMO, physical layer security, and cooperative communications. He has co-authored many research papers in wireless communications and co-authored the Cambridge University Press textbook *Fundamentals of Massive MIMO* (2016).

Dr. Hien Quoc Ngo received the IEEE ComSoc Stephen O. Rice Prize in Communications Theory in 2015, the IEEE ComSoc Leonard G. Abraham Prize in 2017, and the Best PhD Award from EURASIP in 2018. He also received the IEEE Sweden VT-COM-IT Joint Chapter Best Student Journal Paper Award in 2015. He was an *IEEE Communications Letters* exemplary reviewer for 2014, an *IEEE Transactions on Communications* exemplary reviewer for 2015, and an *IEEE Wireless Communications Letters* exemplary reviewer for 2016. He was awarded the UKRI Future Leaders Fellowship in 2019. Dr. Hien Quoc Ngo currently serves as an Editor for the IEEE Transactions on Wireless Communications, IEEE Wireless Communications Letters, Digital Signal Processing, Elsevier Physical Communication (PHYCOM), and IEICE Transactions on Fundamentals of Electronics, Communications and Computer Sciences. He was a Guest Editor of IET Communications, special issue on "Recent Advances on 5G Communications" and a Guest Editor of IEEE Access, special issue on "Modelling, Analysis, and Design of 5G Ultra-Dense Networks", in 2017. He has been a member of Technical Program Committees for several IEEE conferences such as ICC, GLOBECOM, WCNC, and VTC.

Boris Bellalta is an Associate Professor in the Department of Information and Communication Technologies (DTIC) at Universitat Pompeu Fabra (UPF). He obtained his Ph.D. in Information and Communication Technologies from UPF in 2007. His research interests are in the area of wireless networks, with emphasis on the design and performance evaluation of new architectures and protocols.

Paper II

Intelligent Reflecting Surfaces at Terahertz Bands: Channel Modeling and Analysis

Konstantinos Dovelos*, Stylianos D. Assimonis†, Hien Quoc Ngo†, Boris Bellalta*, and Michail Matthaiou†
*Department of Information and Communication Technologies, Universitat Pompeu Fabra (UPF), Barcelona, Spain
†Institute of Electronics, Communications and Information Technology (ECIT), Queen's University Belfast, Belfast, U.K.
Email: {konstantinos.dovelos, boris.bellalta}@upf.edu, {s.assimonis, hien.ngo, m.matthaiou}@qub.ac.uk

***Abstract*—An intelligent reflecting surface (IRS) at terahertz (THz) bands is expected to have a massive number of reflecting elements to compensate for the severe propagation losses. However, as the IRS size grows, the conventional far-field assumption starts becoming invalid and the spherical wavefront of the radiated waves should be taken into account. In this work, we consider a spherical wave channel model and pursue a comprehensive study of IRS-aided multiple-input multiple-output (MIMO) in terms of power gain and energy efficiency (EE). Specifically, we first analyze the power gain under beamfocusing and beamforming, and show that the latter is suboptimal even for multiple meters away from the IRS. To this end, we derive an approximate, yet accurate, closed-form expression for the loss in the power gain under beamforming. Building on the derived model, we next show that an IRS can significantly improve the EE of MIMO when it operates in the radiating near-field and performs beamfocusing. Numerical results corroborate our analysis and provide novel insights into the design and performance of IRS-assisted THz communication.**

I. Introduction

Terahertz (THz) communication is widely deemed a key enabler for future 6G wireless networks due to the abundance of available spectrum at THz bands [1]. However, THz wireless links are subject to severe propagation losses, which require transceivers with a massive number of antennas to compensate for these losses and extend the communication range [2]. On the other hand, unlike sub-6 GHz systems, the power consumption of THz radio-frequency (RF) circuitry is considerably high, which might undermine the deployment of large antenna arrays in an energy efficient manner [3]. To overcome this problem, the novel concept of intelligent reflecting surface (IRS) can be exploited to build transceivers with a relatively small number of antennas, which work along with an IRS to achieve high spectral efficiency with reduced power consumption [4]. Thus, the performance analysis of IRS-aided THz communication is of great research importance.

There is a large body of literature investigating the modeling and performance of IRSs at sub-6 GHz and millimeter wave bands. Most of them, though, treat the IRS element as a typical antenna that re-radiates the impinging wave, and leverage antenna theory to characterize the path loss of the IRS-aided link. Furthermore, they assume far-field, where the spherical wavefront of the emitted waves degenerates to a plane wavefront. Although these approaches are popular due to their simplicity, they might not capture the unique features of IRSs, and especially at THz bands. To this direction, [5] introduced a path loss model for the sub-6 GHz band by invoking *plate scattering theory*, but assuming a specific scattering plane; hence, it is applicable only to special cases. The authors in [6] extended the said path loss model to arbitrary incident angles and polarizations, but considered the far-field zone of the IRS. Recently, a stream of papers (e.g., [7], [8], and references therein) proposed a path loss model that is applicable to near-field, using the "$\cos^q$" radiation pattern [9] for each IRS element, which differs from the plate scattering-based model.

Although there are still many critical questions about the operation of THz IRSs, there is a dearth of related literature. From related work, we distinguish [10], where the authors showed that the far-field beampattern of a holographic IRS can be well approximated by that of an ultra-dense IRS, and then proposed a channel estimation scheme for THz massive multiple-input multiple-output (MIMO) aided by a holographic IRS. However, due to the high propagation losses and the short wavelength, a THz IRS is expected to consist of a massive number of passive reflecting elements, resulting in a radiating near-field, i.e., Fresnel zone, of several meters. Additionally, to effectively overcome the path loss of the transmitter-IRS link, the transmitter will need to operate near the IRS, which is in sharp contrast to sub-6 GHz massive MIMO of macrocell deployments. In conclusion, a THz IRS calls for a carefully tailored design that takes into account the aforementioned particularities.

This paper aims to shed light on these aspects, and study the channel modeling and performance of THz IRS. In particular:

- We provide a near-field channel model for THz frequencies. Our model is physically consistent, and takes into account the size of the IRS elements in the path loss calculation, as well as in the spherical wavefront of the radiated waves.
- We show that a typical THz IRS is likely to operate in the Fresnel zone, where conventional beamforming is suboptimal and hence can reduce the power gain. More importantly, we analytically evaluate that loss by providing an approximate closed-form expression.
- We compare IRS-aided MIMO with MIMO, and demonstrate the energy efficiency (EE) gains of the former architecture. More specifically, we determine the optimal number of IRS elements required to attain the same rate as MIMO with reduced power consumption, and reveal the EE scaling laws.

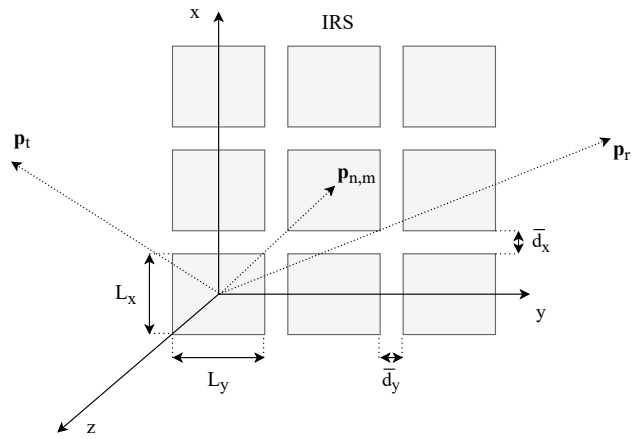

Fig. 1: Illustration of the IRS geometry considered in the channel model.

Notation: $D_N(x) = \frac{\sin(Nx/2)}{N\sin(x/2)}$ is the Dirichlet sinc function; $\mathbf{A}$ is a matrix; $\mathbf{a}$ is a vector; $[\mathbf{A}]_{i,j}$ is the (i,j)th entry of $\mathbf{A}$; $\mathbf{A}^T$ and $\mathbf{A}^H$ are the transpose and conjugate transpose of $\mathbf{A}$, respectively, vec$(\mathbf{A})$ is the column vector formed by stacking the columns of $\mathbf{A}$; and $\mathcal{CN}(\boldsymbol{\mu}, \boldsymbol{\Sigma})$ is a complex Gaussian vector with mean $\boldsymbol{\mu}$ and covariance matrix $\boldsymbol{\Sigma}$.

II. System Model

A. Signal Model

Consider a THz IRS system where the transmitter (Tx) and receiver (Rx) have a single antenna each. The IRS is placed in the xy-plane, and it consists of $N = N_x \times N_y$ passive reflecting elements. Each reflecting element is of size $L_x \times L_y$, and the spacings between adjacent elements are $\bar{d}_x$ and $\bar{d}_y$ along the x and y directions, respectively. The reflection coefficient of the (n,m)th IRS element is $e^{j\varphi_{n,m}}$, where $\varphi_{n,m} \in [-\pi, \pi]$. We next focus on the Tx-IRS-Rx link. The baseband signal at the receiver is then written as

$$y = \mathbf{h}_r^T \boldsymbol{\Phi} \mathbf{h}_t s + \tilde{n}, \tag{1}$$

where $\boldsymbol{\Phi} = \text{diag}(\text{vec}(\tilde{\boldsymbol{\Phi}})) \in \mathbb{C}^{N\times N}$, with $\tilde{\boldsymbol{\Phi}} \in \mathbb{C}^{N_x \times N_y}$ and $[\tilde{\boldsymbol{\Phi}}]_{n,m} = e^{j\varphi_{n,m}}$, is the IRS's reflection matrix, $\mathbf{h}_r \in \mathbb{C}^{N\times 1}$ is the channel from the Rx to the IRS, $\mathbf{h}_t \in \mathbb{C}^{N\times 1}$ is the channel from the Tx to the IRS, $s \sim \mathcal{CN}(0, P_t)$ is the transmitted data symbol, P_t is the average power per data symbol, and $\tilde{n} \sim \mathcal{CN}(0, \sigma^2)$ is the additive noise.

B. Channel Model

1) Spherical Wavefront: Unlike antenna arrays that are typically modeled as a collection of point radiators, an IRS comprises rectangular reflecting elements whose size cannot be neglected. Assume that the center of the $(0,0)$th IRS element is placed at the origin of the coordinate system, as shown in Fig. 1. Across the (n,m)th IRS element, the reflection coefficient $e^{j\varphi_{n,m}}$ remains constant, and the phase difference between adjacent elements is measured from their centers. Thus, the position vector of the (n,m)th IRS element is $\mathbf{p}_{n,m} = (nd_x, md_y, 0)$, where $d_x \triangleq \bar{d}_x + L_x$ and $d_y \triangleq \bar{d}_y + L_y$. Let λ denote the carrier wavelength. Henceforth, we consider $L_x = L_y = \lambda/2$ and $\bar{d}_x = \bar{d}_y = 0$ [8], [11].

The Tx and Rx are located in (D_t, θ_t, ϕ_t) and (D_r, θ_r, ϕ_r), respectively, and hence their position vectors in Cartesian coordinates are

$$\mathbf{p}_t = (D_t \cos\phi_t \sin\theta_t, D_t \sin\phi_t \sin\theta_t, D_t \cos\theta_t), \tag{2}$$

$$\mathbf{p}_r = (D_r \cos\phi_r \sin\theta_r, D_r \sin\phi_r \sin\theta_r, D_r \cos\theta_r), \tag{3}$$

where D_t and D_r are the distances measured from the (0,0)th IRS element, while ϕ and θ denote the azimuth and polar angles, respectively. The baseband channel from the Tx to the IRS is specified as $\mathbf{h}_t = \text{vec}(\mathbf{M}_t)$, where $\mathbf{M}_t \in \mathbb{C}^{N_x \times N_y}$ is the auxiliary matrix with entries [12]

$$[\mathbf{M}_t]_{n,m} = \sqrt{\text{PL}_{n,m}^t} e^{-jkD_{n,m}^t}. \tag{4}$$

In (4), $k = \frac{2\pi}{\lambda}$ is the wavenumber, $\text{PL}_{n,m}^t$ is the path loss between the Tx and the (n,m)th IRS element, and $D_{n,m}^t \triangleq \|\mathbf{p}_t - \mathbf{p}_{n,m}\|$ is the respective distance, with $D_{0,0}^t = D_t$. Similarly, we have $\mathbf{h}_r = \text{vec}(\mathbf{M}_r)$, where $\mathbf{M}_r \in \mathbb{C}^{N_x \times N_y}$ is the auxiliary matrix with entries

$$[\mathbf{M}_r]_{n,m} = \sqrt{\text{PL}_{n,m}^r} e^{-jkD_{n,m}^r}, \tag{5}$$

where $\text{PL}_{n,m}^r$ is the path loss between the Rx and the (n,m)th IRS element, and $D_{n,m}^r \triangleq \|\mathbf{p}_r - \mathbf{p}_{n,m}\|$, with $D_{0,0}^r = D_r$. Using (4) and (5), the received signal in (1) is recast as

$$y = \sum_{n=0}^{N_x-1} \sum_{m=0}^{N_y-1} \sqrt{\text{PL}_{n,m}} e^{-jk(D_{n,m}^t + D_{n,m}^r)} e^{j\varphi_{n,m}} s + \tilde{n}, \tag{6}$$

where $\text{PL}_{n,m} = \text{PL}_{n,m}^t \text{PL}_{n,m}^r$ denotes the overall path loss of the Tx-IRS-Rx link through the (n,m)th reflecting element. Hence, the receive signal-to-noise ratio (SNR) is

$$\text{SNR} = \frac{P_t}{\sigma^2} \left| \sum_{n=0}^{N_x-1} \sum_{m=0}^{N_y-1} \sqrt{\text{PL}_{n,m}} e^{-jk(D_{n,m}^t + D_{n,m}^r)} e^{j\varphi_{n,m}} \right|^2. \tag{7}$$

In the sequel, we detail the path loss model for THz bands, which relies on the plate scattering paradigm [13].

2) Scattered Field by an IRS Element: We focus on an arbitrary IRS element and omit the subscript "n,m" hereafter. The Tx and Rx are in the far-field of the *individual element*, which implies that $D_t, D_r > 2L_{\max}^2/\lambda$, where $2L_{\max}^2/\lambda$ is the Fraunhofer distance and $L_{\max} = \max(L_x, L_y)$ is the maximum dimension of the element. Consequently, a plane wavefront is assumed across the IRS element. For simplicity, we consider a transverse electric incident wave which is linearly polarized along the x-axis. The electric field (E-field) of the incident plane wave is hence given by

$$\mathbf{E}_i = E_i e^{-jk(y\sin\theta_t - z\cos\theta_t)} \mathbf{e}_x, \tag{8}$$

where $\mathbf{e}_x$ denotes the unit vector along the x-axis. Next, the scattered field $\mathbf{E}_s$ at the receiver location (D_r, θ_r, ϕ_r) is determined using physical optics techniques, whereby the IRS element is modeled as a perfectly conducting plate.

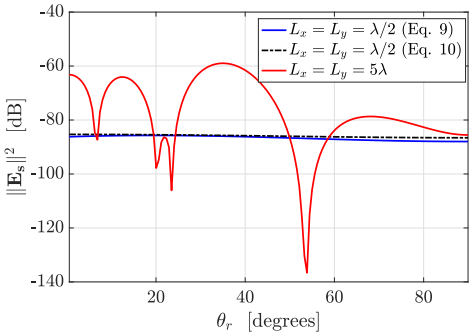

Fig. 2: Squared magnitude of the scattered field versus observation angle θ_r for incident angle $\theta_t = 30°$ and scattering plane $\phi_r = 60°$; $|E_i|^2 = 1$, carrier frequency $f = 300$ GHz, and $D_r = 4$ meters.

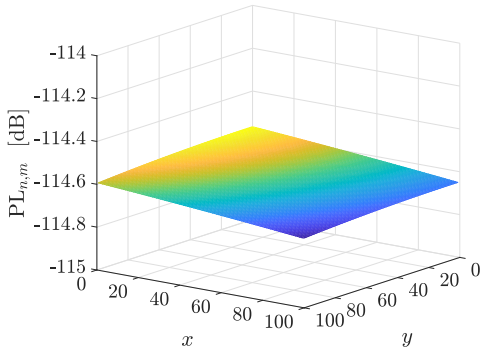

Fig. 3: Path loss across an 100×100-element IRS; $f = 300$ GHz, $\kappa_{\text{abs}}(f) = 0.0033$ m^{-1}, $L_x = L_y = \lambda/2$, $\bar{d}_x = \bar{d}_y = 0$, $G_t = G_r = 20$ dBi, $\mathbf{p}_t = (0, -0.3, 0.6)$, $D_t = 0.67$ m, $\mathbf{p}_r = (0, 1, 1)$, and $D_r = 1.41$ m.

Specifically, the squared magnitude of the scattered E-field[1] is given by [13, Ch. 11]

$$\|\mathbf{E}_s\|^2 = \left(\frac{L_x L_y}{\lambda}\right)^2 \frac{|E_i|^2}{D_r^2} F(\theta_t, \phi_r, \theta_r) \text{sinc}^2(X) \text{sinc}^2(Y) \tag{9}$$

$$\approx \left(\frac{L_x L_y}{\lambda}\right)^2 \frac{|E_i|^2}{D_r^2} F(\theta_t, \phi_r, \theta_r), \tag{10}$$

where $F(\theta_t, \phi_r, \theta_r) \triangleq \cos^2\theta_t(\cos^2\theta_r \cos^2\phi_r + \sin^2\phi_r)$, while $X \triangleq \frac{\pi L_x}{\lambda} \sin\theta_r \cos\phi_r$ and $Y \triangleq \frac{\pi L_y}{\lambda}(\sin\theta_r \sin\phi_r - \sin\theta_t)$. The approximation in (10) follows from $\text{sinc}(X) \approx 1$ and $\text{sinc}(Y) \approx 1$ for $X \approx 0$ and $Y \approx 0$, which holds for $L_x \leq \lambda$ and $L_y \leq \lambda$. This is also verified in Fig. 2. It is worth stressing that each IRS element is expected to be of sub-wavelength size in order to act as an isotropic scatterer [14].

3) Path Loss: Recall that the relation between P_t and E_i is $|E_i|^2/(2\eta) = P_t G_t/(4\pi D_t^2)$, where η is the free-space impedance, and G_t is the transmit antenna gain [15]. Hence, the power density of the scattered field is

$$S_s = \frac{\|\mathbf{E}_s\|^2}{2\eta} = \left(\frac{L_x L_y}{\lambda}\right)^2 \frac{P_t G_t}{4\pi D_t^2 D_r^2} F(\theta_t, \phi_r, \theta_r). \tag{11}$$

Considering the receive aperture $A_r = G_r \lambda^2/(4\pi)$ yields the receive power

$$P_r = S_s A_r = P_t \frac{G_t G_r}{(4\pi D_t D_r)^2} (L_x L_y)^2 F(\theta_t, \phi_r, \theta_r). \tag{12}$$

Finally, taking into account the molecular absorption losses at THz bands gives the path loss of the Tx-IRS-Rx link through the (n, m)th element

$$\text{PL}_{n,m} = \frac{G_t G_r (L_x L_y)^2}{(4\pi D_{n,m}^t D_{n,m}^r)^2} F(\theta_t, \phi_r, \theta_r) e^{-\kappa_{\text{abs}}(f)(D_{n,m}^t + D_{n,m}^r)}, \tag{13}$$

where $\kappa_{\text{abs}}(f)$ is the molecular absorption coefficient at the carrier frequency f. From Fig. 3, we see that $\text{PL}_{n,m}$ marginally changes across the IRS, even for 100×100 elements and a Tx distance $D_t = 0.67$ m. This is because of the small physical size of the IRS at THz bands. Hereafter, we will assume that $\text{PL}_{n,m} \approx \text{PL}$, where PL is calculated using D_t and D_r measured from the $(0, 0)$th IRS element.

[1]The IRS elements can alter the phase of the scattered wave. The reflection coefficient does not appear in the formula of $\|\mathbf{E}_s\|^2$ since $|e^{j\varphi_{n,m}}|^2 = 1$.

TABLE I
IRS WITH $L_x = L_y = \lambda/2$ AND $\bar{d}_x = \bar{d}_y = 0$ AT $f = 300$ GHz.

$N_x \times N_y$ Elements	Physical Size [m^2]	Fresnel Region [m]
80×80	0.039×0.039	$[0.15, 3.2]$
100×100	0.05×0.05	$[0.22, 5]$

III. Power Gain of IRS-Aided THz System

A. Fresnel Region

The near-field of an IRS refers to distances that are smaller than the Fraunhofer distance $D_F \triangleq 2L_{\text{IRS}}^2/\lambda$, where $L_{\text{IRS}} \triangleq \max\left(N_x L_x + (N_x - 1)\bar{d}_x, N_y L_y + (N_y - 1)\bar{d}_y\right)$ is the maximum physical dimension of the IRS. In our work, we focus on the radiating near-field, i.e., Fresnel region, which corresponds to distances $D \gg \lambda$ satisfying [15]

$$0.62\sqrt{L_{\text{IRS}}^3/\lambda} < D \leq 2L_{\text{IRS}}^2/\lambda. \tag{14}$$

From Table I, we verify the small physical size of THz IRS, as well as its large Fresnel region. Consequently, it is very likely that the Tx and Rx are in the near-field of the IRS, where the spherical wavefront of the impinging waves *across the IRS* cannot be neglected.

B. Near-Field Beamfocusing

Let us define the normalized power gain as

$$G \triangleq \frac{\left|\sum_{n=0}^{N_x-1}\sum_{m=0}^{N_y-1} e^{-jk\left(D_{n,m}^t + D_{n,m}^r\right)} e^{j\varphi_{n,m}}\right|^2}{N_x^2 N_y^2}, \tag{15}$$

with $G \in [0, 1]$. The receive SNR in (7) is now written as

$$\text{SNR} \approx \frac{N^2 G P_t \text{PL}}{\sigma^2}. \tag{16}$$

The power gain is maximized by near-field beamfocusing. Hence, the phase induced by the (n, m)th IRS element is

$$\varphi_{n,m} = k\left(D_{n,m}^t + D_{n,m}^r\right), \tag{17}$$

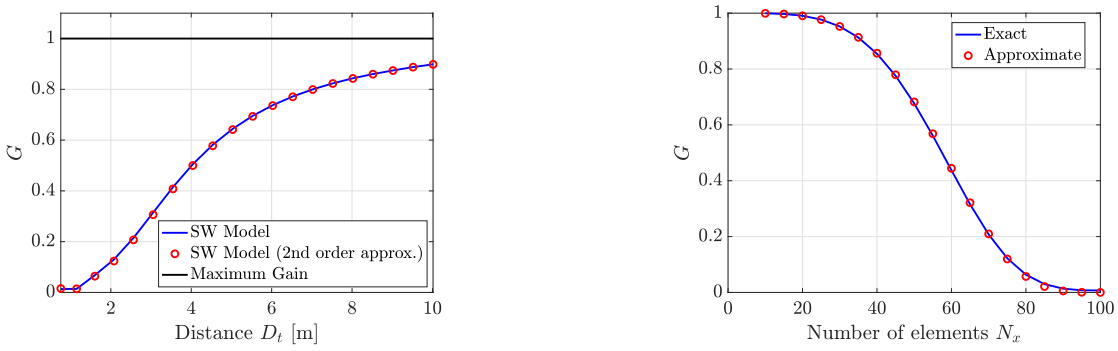

(a) (b)

Fig. 4: Results for far-field beamforming: (a) normalized power gain vs. distance D_t for an 100×100-element IRS, where $\mathbf{p}_t = (0.4, 0.4, z)$, $0.5 \leq z \leq 10$, and $0.755 \leq D_t \leq 10.016$ m; (b) normalized power gain vs. number of elements for an $N_x \times N_y$-element IRS, where $N_x = N_y$, $\mathbf{p}_t = (0.4, 0.4, 1)$, and $D_t = 1.15$ m. The other parameters are $f = 300$ GHz, $L_x = L_y = \lambda/2$, and $\bar{d}_x = \bar{d}_y = 0$.

which yields $G = 1$ and $\text{SNR} = N^2 P_t \text{PL}/\sigma^2$. As expected, the SNR of an IRS-aided system grows quadratically with the number N of IRS elements [16]. Note, though, that the IRS needs to know the exact locations of the Tx and Rx in order to perform beamfocusing.

C. Far-Field Beamforming

In this section, we analyze the power gain under conventional far-field beamforming, which relies on the parallel ray approximation. First, using basic algebra, we have that

$$D^r_{n,m} = D_r \left(1 + \frac{(nd_x)^2}{D_r^2} - \frac{2\cos\phi_r \sin\theta_r n d_x}{D_r} + \frac{(md_y)^2}{D_r^2} - \frac{2\sin\phi_r \sin\theta_r m d_y}{D_r}\right)^{1/2}. \quad (18)$$

In the far-field $D_r \gg D_F$, the first-order Taylor expansion $(1+x)^a \approx 1 + ax$ can be applied to (18), while ignoring the quadratic terms $(nd_x)^2/D_r^2$ and $(md_y)^2/D_r^2$. This yields

$$D^r_{n,m} \approx D_r - nd_x \cos\phi_r \sin\theta_r - md_y \sin\phi_r \sin\theta_r, \quad (19)$$

which corresponds to the plane wavefront model.

Remark 1. *The far-field steering vector is defined as* $\mathbf{a}(\phi,\theta) \triangleq \text{vec}(\mathbf{M})$, *where* $\mathbf{M} \in \mathbb{C}^{N_x \times N_y}$ *is the matrix with elements* $[\mathbf{M}]_{n,m} = e^{jk(nd_x \cos\phi \sin\theta + md_y \sin\phi \sin\theta)}$. *Thus, the channel vector is* $\mathbf{h} = \sqrt{\text{PL}} e^{-jkD} \mathbf{a}(\phi,\theta)$.

Let us now consider that the Rx is in the far-field of the IRS whilst the Tx is close to the IRS; in fact, this deployment yields the maximum SNR, compared to placing the IRS somewhere in between [17]. If the IRS employs beamforming based on the angular information (ϕ_t, θ_t) and (ϕ_r, θ_r), i.e.,

$$\varphi_{n,m} = -k(nd_x \cos\phi_t \sin\theta_t + md_y \sin\phi_t \sin\theta_t + nd_x \cos\phi_r \sin\theta_r + md_y \sin\phi_r \sin\theta_r), \quad (20)$$

the power gain will decrease. To analytically characterize this reduction, we use the second-order Taylor expansion $(1+x)^a \approx 1 + ax + \frac{1}{2}a(a-1)x^2$ and neglect the terms $O(d^q/D^q), q \geq 3$, which yields the (Fresnel) approximation of the Tx distance

$$D^t_{n,m} \approx D_t + \frac{(nd_x)^2(1-\cos^2\phi_t \sin^2\theta_t)}{2D_t} - nd_x \cos\phi_t \sin\theta_t + \frac{(md_y)^2(1-\sin^2\phi_t \sin^2\theta_t)}{2D_t} - md_y \sin\phi_t \sin\theta_t. \quad (21)$$

Using (19), (20) and (21), the normalized power gain in (15) reduces to the expession (22) at the top of the last page. The accuracy of the approximation of the Tx distance is depicted in Fig. 4(a), and the validity of (22) is evaluated in Fig. 4(b). Note that the lower limit of the Fresnel zone of an 100×100-element IRS, with $L_x = L_y = \lambda/2$ and $\bar{d}_x = \bar{d}_y = 0$, is 0.22 meters according to Table I. Thus, the distances in the numerical experiments were chosen so that the Tx does not operate in the reactive near-field. As observed, beamforming can substantially decrease the power gain even for distances of several meters away from the IRS. This is because of the mismatch between (17) and (20). Moreover, from (22), we have the asymptotic result $G \to 0$ as $N \to \infty$. In conclusion, near-field beamfocusing should be used in most cases of interest.

IV. Performance of IRS-Aided THz System

A. Benchmark: MIMO System

Consider a MIMO system, where the Tx and Rx are equipped with N_t and N_r antennas, respectively. For efficient hardware implementation, hybrid array architectures are assumed at both ends. The path loss of the direct channel, i.e., line-of-sight (LoS), is given by

$$\text{PL}_{\text{MIMO}} = \frac{G_t G_r \lambda^2}{(4\pi D_d)^2} e^{-\kappa_{\text{abs}}(f) D_d}, \quad (23)$$

where $D_d = \|\mathbf{p}_r - \mathbf{p}_t\|$. Assuming far-field, the LoS channel is rank-one. Then, analog beamforming and combining yield the receive SNR

$$\text{SNR}_{\text{MIMO}} = \frac{N_r N_t P_t \text{PL}_{\text{MIMO}}}{\sigma^2}. \quad (24)$$

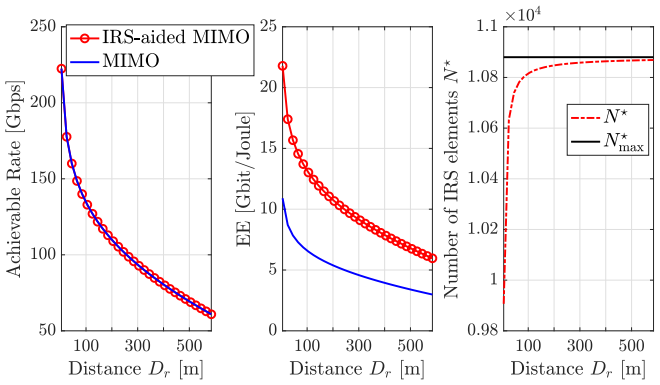

Fig. 5: Achievable rate, EE, and number of IRS elements versus distance D_r for $\alpha = 2$ and a fixed IRS location at (0,0,0). In the MIMO system, $N_t = 100$ and $N_r = 100$. The other parameters are $G_t = G_r = 20$ dBi, $P_t = 10$ dBm, $\sigma^2 = -174$ dBm/Hz, $B = 10$ GHz, $f = 300$ GHz, $L_x = L_y = \lambda/2$, $\mathbf{p}_t = (0, -0.6, 1)$ with $D_t = 1.16$ m, and $\mathbf{p}_r = (0, D_r, 1)$.

Lastly, the respective power consumption is calculated as[2]

$$P_c^{\text{MIMO}} = P_t + N_r(P_{\text{PS}} + P_{\text{PA}}) + N_t(P_{\text{PS}} + P_{\text{PA}}), \quad (25)$$

where $P_{\text{PS}} = 42$ mW and $P_{\text{PA}} = 60$ mW are the power consumption values for a phase shifter and a power amplifier at $f = 300$ GHz, respectively [3].

B. IRS-Assisted MIMO System

The Tx and Rx perform beamforming and combining to communicate a single stream through an IRS of N elements. Due to the directional transmissions, the Tx-Rx link is negligible, and thus is ignored. The received signal through the Tx-IRS-Rx channel is given by

$$y = \mathbf{w}^H(\mathbf{H}_r \mathbf{\Phi} \mathbf{H}_t \mathbf{f} s + \tilde{\mathbf{n}}), \quad (26)$$

where $\mathbf{w} \in \mathbb{C}^{N_r \times 1}$ is the combiner, $\mathbf{f} \in \mathbb{C}^{N_t \times 1}$ is the beamformer, $\mathbf{H}_t \in \mathbb{C}^{N \times N_t}$ is the channel from the Tx to the IRS, $\mathbf{H}_r \in \mathbb{C}^{N_r \times N}$ is the channel from the IRS to the Rx, and $\tilde{\mathbf{n}} \sim \mathcal{CN}(\mathbf{0}, \sigma^2 \mathbf{I}_{N_r})$ is the noise vector. For ease of exposition, we assume far-field for both the Tx and the Rx. Then,

$$\mathbf{H}_r = \sqrt{\text{PL}_r} e^{-jkD_r} \mathbf{a}_r(\phi_{\text{rx}}, \theta_{\text{rx}}) \mathbf{a}_{\text{IRS}}^H(\phi_r, \theta_r), \quad (27)$$

$$\mathbf{H}_t = \sqrt{\text{PL}_t} e^{-jkD_t} \mathbf{a}_{\text{IRS}}(\phi_t, \theta_t) \mathbf{a}_t^H(\phi_{\text{tx}}, \theta_{\text{tx}}), \quad (28)$$

where $\text{PL}_t \approx \text{PL}_{n,m}^t$ and $\text{PL}_r \approx \text{PL}_{n,m}^r$; the far-field response vectors $\mathbf{a}_r(\cdot,\cdot)$, $\mathbf{a}_t(\cdot,\cdot)$, and $\mathbf{a}_{\text{IRS}}(\cdot,\cdot)$ are specified according to Remark 1. For $\mathbf{f} = \mathbf{a}_t(\phi_{\text{tx}}, \theta_{\text{tx}})/\sqrt{N_t}$, $\mathbf{w}^H = \mathbf{a}_r^H(\phi_{\text{rx}}, \theta_{\text{rx}})/\sqrt{N_r}$, and proper $\mathbf{\Phi}$, the receive SNR is

$$\text{SNR}_{\text{IRS}} = \frac{N_t N_r N^2 P_t \text{PL}_{\text{IRS}}}{\sigma^2}, \quad (29)$$

where PL_{IRS} is the path loss (13) of the IRS-aided link. Using varactor diodes, the power expenditure of an IRS element is negligible [8]. Thus, the power consumption is determined as

$$P_c^{\text{IRS}}(N_t, N_r) = P_t + N_r(P_{\text{PS}} + P_{\text{PA}}) + N_t(P_{\text{PS}} + P_{\text{PA}}). \quad (30)$$

[2]The power consumption of signal processing is neglected.

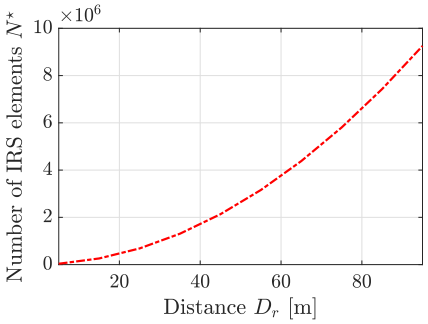

Fig. 6: Number of IRS elements $N^\star$ versus distance D_r for $\alpha = 2$; $\mathbf{p}_t = (0, -0.6, 1)$, $\mathbf{p}_r = (0, D_r, 1)$, IRS at $(0, (D_r - y_t)/2, 1)$ with $y_t = -0.6$, $f = 300$ GHz, $\kappa_{\text{abs}}(f) = 0.0033$ m^{-1}, and $L_x = L_y = \lambda/2$.

Proposition 1. *The IRS-aided system with N_t/α and N_r/α attains a higher SNR than MIMO with N_t and N_r for*

$$N^\star \geq \alpha \frac{\lambda}{L_x L_y} \frac{D_t D_r}{\sqrt{F(\theta_t, \phi_r, \theta_r) D_d}} e^{-\frac{1}{2}\kappa_{\text{abs}}(f)(D_d - D_r - D_t)}. \quad (31)$$

Proof. According to (24) and (29), the IRS-aided system attains a higher SNR for $N^\star \geq \sqrt{\alpha^2 \text{PL}_{\text{MIMO}}/\text{PL}_{\text{IRS}}}$, which gives the desired result after basic algebra. □

Using Proposition 1, we can now decrease the number of Tx and Rx antennas by a factor α to reduce the power consumption as

$$P_c^{\text{IRS}}(N_t/\alpha, N_r/\alpha) = P_t + \frac{N_r}{\alpha}(P_{\text{PS}} + P_{\text{PA}}) + \frac{N_t}{\alpha}(P_{\text{PS}} + P_{\text{PA}}) \approx P_c^{\text{MIMO}}/\alpha, \quad (32)$$

while keeping the achievable rate fixed. Hence, the EE gain with respect to MIMO is approximately equal to α.

V. Numerical Results

In this section, we assess the performance of IRS-aided THz communication through numerical simulations. For this purpose, we calculate the achievable rate as

$$R = B \log_2(1 + \text{SNR}), \quad (33)$$

where B is the signal bandwidth. Moreover, the EE is specified as $\text{EE} \triangleq R/P_c$.

A. Energy Efficiency

We consider a MIMO setup with $N_t = N_r = 100$ antennas, i.e., 10×10-element planar arrays. From Fig. 5, we verify that the IRS-assisted system with $N_t = N_r = 50$ antennas offers a two-fold EE gain. Consequently, an IRS can provide an alternative communication link, in addition to LoS, where the Tx and Rx employ a smaller number of antennas to communicate with each other, hence saving energy. Note, though, that the suggested benefits are valid when: 1) the power expenditure of IRS elements is negligible compared to that of conventional phase shifters; 2) the Tx operates near the IRS in order to have a reasonable number of reflecting elements $N^\star$; and 3) reflection losses are small [18].

$$G = \frac{\left|\sum_{n=0}^{N_x-1} e^{-jk\frac{(nd_x)^2(1-\cos^2\phi_t\sin^2\theta_t)}{2D_t}}\right|^2}{N_x^2}\frac{\left|\sum_{m=0}^{N_y-1} e^{-jk\frac{(md_y)^2(1-\sin^2\phi_t\sin^2\theta_t)}{2D_t}}\right|^2}{N_y^2}$$
$$\approx \frac{\left|\sum_{n=0}^{N_x^2-1} e^{-jk\frac{nd_x^2(1-\cos^2\phi_t\sin^2\theta_t)}{2D_t}}\right|^2}{N_x^4}\frac{\left|\sum_{m=0}^{N_y^2-1} e^{-jk\frac{md_y^2(1-\sin^2\phi_t\sin^2\theta_t)}{2D_t}}\right|^2}{N_y^4}$$
$$= \left|D_{N_x^2}\left(\frac{2\pi}{\lambda}\frac{d_x^2(1-\cos^2\phi_t\sin^2\theta_t)}{2D_t}\right)\right|^2\left|D_{N_y^2}\left(\frac{2\pi}{\lambda}\frac{d_y^2(1-\sin^2\phi_t\sin^2\theta_t)}{2D_t}\right)\right|^2. \quad (22)$$

B. IRS Placement and Near-Field Beamfocusing

We now investigate the impact of the IRS position on the number of IRS elements $N^\star$. For the deployment in Fig. 5, D_t is small, and hence $D_r^2 \approx D_t^2 + D_d^2$. Further, $\phi_r = \pi/2$ which gives $F(\theta_t, \phi_r, \theta_r) = \cos^2\theta_t$. Then, (31) reduces to

$$N^\star = \alpha\frac{\lambda}{L_xL_y}\frac{D_tD_r}{\cos\theta_t\sqrt{D_r^2-D_t^2}}e^{-\frac{1}{2}\kappa_{\text{abs}}(f)(\sqrt{D_r^2-D_t^2}-D_r-D_t)}, \quad (34)$$

which takes the asymptotic value

$$N^\star_{\max} = \alpha\frac{\lambda}{L_xL_y}\frac{D_t}{\cos\theta_t}e^{\frac{1}{2}\kappa_{\text{abs}}(f)D_t} \quad (35)$$

as $D_r \to \infty$; this follows from $\sqrt{D_r^2-D_t^2} \approx D_r$ for $D_r \gg D_t$. Thus, $N^\star$ is bounded for a fixed IRS position near the Tx. Due to symmetry, the same holds when the IRS is near the Rx. For instance, $N^\star_{\max} = 10,880$ in Fig. 5. In contrast, when the IRS is deployed always in the middle of the Tx and Rx, $N^\star$ increases as $O(D_tD_r)$. This scaling law is depicted in Fig. 6. Consequently, the IRS has to be close to the link ends in order to compensate for the severe propagation losses with a practical number of reflecting elements. Note that similar findings were reported in [17]. In this case, the Tx/Rx will be in the Fresnel zone of the IRS where near-field beamfocusing becomes the optimal processing strategy; otherwise, the EE gains previously discussed cannot be attained.

VI. Conclusions and Future Work

We studied the channel modeling and performance of IRS-assisted THz communication. First, we introduced a spherical wave channel model and employed plate scattering theory to derive the path loss. We next showed that the path loss is nearly constant across the IRS thanks to its small physical size. However, due to the large number of reflecting elements with respect to the wavelength, the Fresnel zone of a THz IRS is of several meters. To this end, we analyzed the power gain under near-field beamfocusing and conventional beamforming, and proved the suboptimality of the latter. One implication of this is that the IRS needs to know the exact location of the Tx and/or Rx, rather than their angular information, to perform beamfocusing. Capitalizing on the derived model, we finally investigated the EE scaling law of IRS-aided MIMO, and showed that it can outperform MIMO. Numerical results consolidate the potential of IRSs for THz communication. For future work, it would be interesting to study the reflection matrix design for a multi-antenna Tx/Rx that operates in the Fresnel zone of the IRS, as well as pursue an EE analysis under hardware impairments and channel estimation overheads.

References

[1] T. S. Rappaport *et al*., "Wireless communications and applications above 100 GHz: Opportunities and challenges for 6G and beyond," *IEEE Access*, vol. 7, pp. 78729-78757, 2019.

[2] J. Zhang *et al*., "Prospective multiple antenna technologies for beyond 5G," *IEEE J. Sel. Areas Commun.*, vol. 38, no. 8, pp. 1637–1660, Aug. 2020.

[3] L. Yan, C. Han, and J. Yuan, "A dynamic array-of-subarrays architecture and hybrid precoding algorithms for terahertz wireless communications," *IEEE J. Sel. Areas Commun.*, vol. 38, no. 9, pp. 2041-2056, Sept. 2020.

[4] E. Basar *et al*, "Wireless communications through reconfigurable intelligent surfaces," *IEEE Access*, vol. 7, pp. 116753-116773, 2019.

[5] Ö. Özdogan, E. Björnson, and E. G. Larsson, "Intelligent reflecting surfaces: Physics, propagation, and pathloss modeling," *IEEE Wireless Commun. Lett.*, vol. 9, no. 5, pp. 581-585, May 2020.

[6] M. Najafi, V. Jamali, R. Schober, and H. V. Poor, "Physics-based modeling and scalable optimization of large intelligent reflecting surfaces," *IEEE Trans. Commun.*, Dec. 2020.

[7] S. W. Ellingson, "Path loss in reconfigurable intelligent surface-enabled channels," *arXiv preprint* arXiv:1912.06759, 2019.

[8] W. Tang *et al*., "Wireless communications with reconfigurable intelligent surface: Path loss modeling and experimental measurement," *IEEE Trans. Wireless Commun.*, vol. 20, no. 1, pp. 421-439, Jan. 2021.

[9] A. Z. Elsherbeni, F. Yang, and P. Nayeri, *Reflectarray Antennas: Theory, Designs, and Applications*. John Wiley and Sons, 2018.

[10] Z. Wan, Z. Gao, M. Di Renzo, and M.-S. Alouini, "Terahertz massive MIMO with holographic reconfigurable intelligent surfaces," *IEEE Trans. Commun.*, Mar. 2021.

[11] O. Yurduseven, S. D. Assimonis, and M. Matthaiou, "Intelligent reflecting surfaces with spatial modulation: An electromagnetic perspective," *IEEE Open J. Commun. Society*, vol. 1, pp. 1256-1266, Aug. 2020.

[12] F. Guidi and D. Dardari, "Radio positioning with EM processing of the spherical wavefront," *IEEE Trans. Wireless Commun.*, Jan. 2021.

[13] C. A. Balanis, *Advanced Engineering Electromagnetics*, 2nd ed. John Wiley & Sons, 2012.

[14] M. Di Renzo *et al*., "Smart radio environments empowered by reconfigurable intelligent surfaces: How it works, state of research, and the road ahead," *IEEE J. Sel. Areas Commun.*, vol. 38, no. 11, pp. 2450-2525, Nov. 2020.

[15] C. A. Balanis, *Antenna Theory: Analysis and Design*, John Wiley & Sons, 2012.

[16] Q. Wu and R. Zhang, "Intelligent reflecting surface enhanced wireless network via joint active and passive beamforming," *IEEE Trans. Wireless Commun.*, vol. 18, no. 11, pp. 5394-5409, Nov. 2019.

[17] Q. Wu *et al.*, "Intelligent reflecting surface aided wireless communications: A tutorial," *IEEE Trans. Commun.*, Jan. 2021.

[18] S.-K. Chou, O. Yurduseven, H. Q. Ngo, and M. Matthaiou, "On the aperture efficiency of intelligent reflecting surfaces," *IEEE Wireless Commun. Lett*., vol. 10, no. 3, pp. 599-603, Mar. 2021.

Paper III

Electromagnetic Modeling of Holographic Intelligent Reflecting Surfaces at Terahertz Bands

Konstantinos Dovelos*, Stylianos D. Assimonis†, Hien Quoc Ngo†, Boris Bellalta*, and Michail Matthaiou†
*Department of Information and Communication Technologies, Universitat Pompeu Fabra (UPF), Barcelona, Spain
†Institute of Electronics, Communications and Information Technology (ECIT), Queen's University Belfast, Belfast, U.K.
Email: {konstantinos.dovelos, boris.bellalta}@upf.edu, {s.assimonis, hien.ngo, m.matthaiou}@qub.ac.uk

***Abstract*—Intelligent reflecting surface (IRS)-assisted wireless communication is widely deemed a key enabler of 6G systems. The main challenge in deploying an IRS-aided terahertz (THz) link, though, is the severe propagation losses at high frequency bands. Hence, a THz IRS is expected to consist of a massive number of reflecting elements to compensate for those losses. However, as the IRS size grows, the conventional far-field assumption starts becoming invalid and the spherical wavefront of the radiated waves must be taken into account. In this work, we focus on the near-field and analytically determine the IRS response in the Fresnel zone by leveraging electromagnetic theory. Specifically, we derive a novel expression for the path loss and beampattern of a holographic IRS, which is then used to model its discrete counterpart. Our analysis sheds light on the modeling aspects and beamfocusing capabilities of THz IRSs.**

***Index Terms*—Beamfocusing, electromagnetics, intelligent reflecting surfaces, near-field, THz communications.**

I. Introduction

To deal with the imminent spectrum gridlock, terahertz (THz) communication is favored for 6G wireless networks because of the abundant spectrum available at the THz band (0.1 to 10 THz) [1]. However, THz links suffer from high propagation losses, and thus transceivers with a massive number of antennas are needed to compensate for those losses by means of sharp beamforming [2]. On the other hand, the power consumption of THz radio-frequency (RF) circuits is much higher than their sub-6 GHz counterparts, which might undermine the deployment of large-scale antenna arrays in an energy efficient manner [3]. Consequently, addressing these engineering challenges is of paramount importance for future THz communication systems.

Looking beyond conventional antenna arrays, the advent of metasurfaces, which can customize the behavior (e.g., reflection, absorption, polarization, etc.) of electromagnetic (EM) waves, has paved the way for novel wireless technologies, such as intelligent reflecting surfaces (IRSs) [4]. Specifically, an IRS consists of nearly passive reconfigurable elements that can alter the phase of the impinging waves to reflect them towards a desired direction. Moreover, unlike amplify-and-forward relays, an IRS does not require power-hungry RF chains, thereby extending the radio coverage without increasing power consumption [5].

There is a large body of literature that investigates the modeling and performance of IRS-assisted systems at the sub-6 GHz and millimeter wave bands. Nevertheless, the majority of these works, e.g., [6]–[9] and references therein, focus on the far-field regime, where the spherical wavefront of the radiated EM waves degenerates into a plane wavefront. Although the far-field assumption facilitates mathematical analysis, it might not be valid for IRSs operating at the THz band. In particular, an electrically large IRS must be placed close to the transmitter/receiver in order to effectively compensate for the path loss of the transmitter-IRS-receiver link. As a result, one of the link ends is likely to operate in the radiating near-field of the IRS. Additionally, packing an unprecedented number of sub-wavelength reflecting elements into an aperture yields a so-called *holographic reflecting surface* [10], which can offer ultra-narrow pencil beams and extremely large power gains. A few recent papers [11], [12] proposed a path loss model that is applicable to near-field using the popular "$\cos^q$" radiation pattern for each IRS element, but considering a discrete IRS. In a similar spirit, [13], [14] analyzed the power scaling laws and near-field behavior of discrete IRSs (modeled as planar antenna arrays) under a specific user location; hence, this analysis is applicable only to special cases. From the relevant work, we distinguish [15], where the authors showed that the far-field beampattern of a holographic IRS can be well approximated by that of an ultra-dense discrete IRS.

To the best of our knowledge, holographic IRSs have not yet been studied in the near-field region. This paper aims to fill this gap in the literature and shed light on the fundamentals of IRSs. Specifically:

- We determine the field scattered by a holographic IRS in the radiating near-field, i.e., Fresnel zone. More particularly, we employ physical optics from EM theory to model the IRS as a large conducting plate, and then derive the scattered field in closed-form by exploiting the small physical size of THz IRSs.
- We show that the near-field behavior differs significantly from its far-field counterpart, and hence the derived channel model should be adopted for electrically large IRSs. Moreover, the near-field beampattern of a contiguous IRS can be accurately approximated by that of an ultra-dense discrete IRS, thereby enabling the practical realization of holographic reflecting surfaces.
- We discuss the implications of the EM-based model and highlight the importance of beamfocusing in single-user and multi-user transmissions.

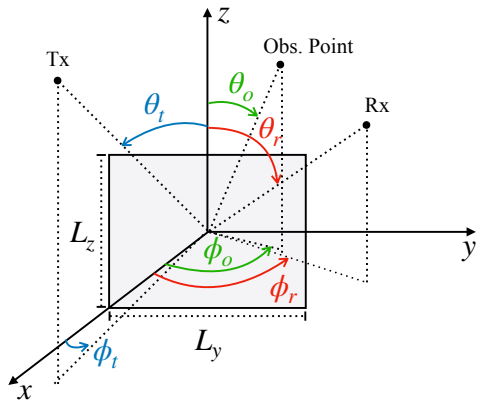

Fig. 1: Illustration of the IRS geometry under consideration.

Notation: $\mathcal{A}$ is a set, $\mathbf{A}$ is a vector field, $\mathbf{a}$ is a vector, $\mathbf{e}_x$, $\mathbf{e}_y$, and $\mathbf{e}_z$ denote the unit vectors along the x, y, and z axes, respectively; $\mathbf{e}_r$, $\mathbf{e}_\theta$, and $\mathbf{e}_\phi$ denote the unit vectors along the radial, polar, and azimuth directions, respectively; $\mathrm{erf}(x) = \frac{2}{\sqrt{\pi}} \int_0^x e^{-t^2} dt$ is the error function; $\mathrm{sinc}(x) = \frac{\sin(x)}{x}$ is the sinc function; and $x \sim \mathcal{CN}(\mu, \sigma^2)$ is a complex Gaussian variable with mean μ and variance σ^2.

II. Electromagnetics-Based Channel Model

Consider a holographic IRS of size $L_y \times L_z$, where L_y and L_z denote the dimensions along the y and z directions, respectively. The coordinate system is placed at the center of the IRS, as shown in Fig. 1. Thus, the IRS is represented by the planar surface $\mathcal{S} = \{(y, z) : |y| \leq L_y/2, |z| \leq L_z/2\}$. In the sequel, we focus on the Fresnel zone of the IRS, which refers to all distances r satisfying [16]

$$0.62\sqrt{L_{\max}^3/\lambda} < r \leq 2L_{\max}^2/\lambda, \tag{1}$$

where $L_{\max} = \max(L_y, L_z)$ denotes the maximum dimension of the IRS, and λ is the wavelength.

A. Spherical Wavefront

Consider an infinitesimal dipole antenna emitting a spherical wave; the dipole is placed parallel to the IRS. The exact position of the transmit antenna is described by the tuple $(x_t, y_t, z_t) = (r_t \cos\phi_t \sin\theta_t, r_t \sin\phi_t \sin\theta_t, r_t \cos\theta_t)$, where r_t is the radial distance, whilst ϕ_t and θ_t are the azimuth and polar angles of arrival, respectively. The electric field (E-field) of the spherical wave impinging on the (y, z)th point of the IRS can be expressed as [16]

$$\mathbf{E}_i = E_\theta \mathbf{e}_\theta = j\sqrt{\frac{\eta P_t G_t}{4\pi}} \frac{e^{-jkr_t(y,z)}}{r_t(y,z)} \mathbf{e}_\theta, \tag{2}$$

where η is the wave impedance, $k = 2\pi/\lambda$ is the wavenumber, P_t is the transmit power, G_t is the gain of the transmit antenna, and

$$\begin{aligned} r_t(y,z) &\triangleq \sqrt{x_t^2 + (y_t - y)^2 + (z_t - z)^2} \\ &= r_t \sqrt{1 + \frac{y^2}{r_t^2} - \frac{2\sin\phi_t \sin\theta_t y}{r_t} + \frac{z^2}{r_t^2} - \frac{2\cos\theta_t z}{r_t}} \end{aligned} \tag{3}$$

is the respective distance. Note that (2) holds for all distances $r_t(y, z) \gg \lambda$, where the radial and azimuthal components E_r and E_ϕ of the E-field are approximately zero. From Maxwell's equations, the magnetic field is specified as

$$\begin{aligned} \mathbf{H}_i &= \frac{j}{\eta k} \nabla \times \mathbf{E}_i = \frac{j}{\eta k} \frac{1}{r} \frac{\partial (r E_\theta)}{\partial r} \mathbf{e}_\phi \\ &= \frac{j}{\eta} \sqrt{\frac{\eta P_t G_t}{4\pi}} \frac{e^{-jkr_t(y,z)}}{r_t(y,z)} \mathbf{e}_\phi = H_\phi \mathbf{e}_\phi, \end{aligned} \tag{4}$$

where $r = r_t(y, z)$ in the partial derivative for notational convenience. Owing to the small physical size of THz IRSs, the amplitude variation $1/r_t(y, z)$ across $\mathcal{S}$ is marginal [13]; for example, an electrically large IRS of size $200\lambda \times 200\lambda$ occupies only 20×20 cm^2 at $f = 300$ GHz. On the contrary, the phase variation $kr_t(y, z)$ is significant and cannot be ignored. In light of these observations, we henceforth consider

$$\frac{e^{-jkr_t(y,z)}}{r_t(y,z)} \approx \frac{e^{-jk(r_t + \tilde{r}_t(y,z))}}{r_t}, \tag{5}$$

where $r_t(y, z) \approx r_t + \tilde{r}_t(y, z)$, with

$$\begin{aligned} \tilde{r}_t(y,z) = &\frac{y^2(1 - \sin^2\phi_t \sin^2\theta_t)}{2r_t} - y \sin\phi_t \sin\theta_t \\ &+ \frac{z^2 \sin^2\theta_t}{2r_t} - z\cos\theta_t, \end{aligned} \tag{6}$$

which follows from the second-order Taylor approximation $(1 + x)^\alpha \approx 1 + \alpha x + \frac{1}{2}\alpha(\alpha - 1)x^2$ of (3).

B. Scattered Field in the Fresnel Zone

According to the surface equivalence principle, the obstacle-free equivalent problem involves an electric current density $\mathbf{J}(y, z)$ (measured in A/m^2) and a magnetic current density $\mathbf{M}(y, z)$ (measured in V/m^2) on $\mathcal{S}$, which satisfy the boundary conditions [17, Ch. 7]

$$\hat{\mathbf{n}} \times \mathbf{H}|_{x=0} = \mathbf{J}(y, z), \tag{7}$$

$$\hat{\mathbf{n}} \times \mathbf{E}|_{x=0} = \mathbf{M}(y, z) = 0, \tag{8}$$

where $\mathbf{E} = \mathbf{E}_i + \mathbf{E}_s$ and $\mathbf{H} = \mathbf{H}_i + \mathbf{H}_s$ are the total electric and magnetic fields, respectively, $\mathbf{E}_s$ and $\mathbf{H}_s$ are the corresponding scattered fields, and $\hat{\mathbf{n}} = \mathbf{e}_x$ is the normal vector of $\mathcal{S}$.[1] Assuming that $\mathcal{S}$ is an infinite PEC, it can be replaced by a virtual source with $\hat{\mathbf{n}} \times \mathbf{H}_s = \hat{\mathbf{n}} \times \mathbf{H}_i$, hence yielding $\mathbf{J}(y, z) = 2\hat{\mathbf{n}} \times \mathbf{H}_i|_{x=0}$.[2] Note that the actual IRS exhibits a surface impedance, which can change the phase of the

[1]The E-field inside S is assumed to be zero, akin to the perfect electric conductor (PEC) paradigm. The PEC model is used for simplicity. Our analysis can readily be applied to the impedance surface model [19].

[2]We assume that image theory holds for a finite plate. Such an assumption can be made in our case because the dimensions of the IRS are very large compared to the wavelength.

surface current density $\mathbf{J}(y,z)$. Thus, we model that property as $\mathbf{J}(y,z) = (2\hat{\mathbf{n}} \times \mathbf{H}_i|_{x=0})e^{j\varphi(y,z)}$ [8], [9]. The phase profile $\varphi(y,z)$ is nonlinear due to the spherical wavefront of the incident wave. To this end, it is decomposed as

$$\varphi(y,z) = k\left(C_1 y^2 + C_2 y + C_3 z^2 + C_4 z\right), \tag{9}$$

where C_1, C_2, C_3, and C_4 are properly selected constants.

Let $(x_r, y_r, z_r) = (r_r \cos\phi_r \sin\theta_r, r_r \sin\phi_r \sin\theta_r, r_r \cos\theta_r)$ be the receiver location, where r_r is the radial distance, while ϕ_t and θ_t denote the azimuth and polar angles of departure, respectively. Next, the scattered E-field at the receiver is analytically determined using the auxiliary vector potential

$$\begin{aligned}\mathbf{A}(x_r,y_r,z_r) &\triangleq \frac{\mu}{4\pi}\iint_{\mathcal{S}} \mathbf{J}(y,z)\frac{e^{-jkr_r(y,z)}}{r_r(y,z)}dydz \\ &\overset{(a)}{\approx} \frac{\mu e^{-jkr_r}}{4\pi r_r}\iint_{\mathcal{S}} \mathbf{J}(y,z)e^{-jk\tilde{r}_r(y,z)}dydz \\ &= \frac{\mu e^{-jkr_r}}{4\pi r_r}(\tilde{A}_r\mathbf{e}_r + \tilde{A}_\theta\mathbf{e}_\theta + \tilde{A}_\phi\mathbf{e}_\phi), \end{aligned} \tag{10}$$

where μ is the magnetic permeability of the propagation medium, (a) follows from the Fresnel approximation of the distance $r_r(y,z) \approx r_r + \tilde{r}_r(y,z)$, and

$$\tilde{A}_r = \iint_{\mathcal{S}} (J_y \sin\theta_r \sin\phi_r + J_z \cos\theta_r)e^{-jk\tilde{r}_r(y,z)}dydz, \tag{11}$$

$$\tilde{A}_\theta = \iint_{\mathcal{S}} (J_y \cos\theta_r \sin\phi_r - J_z \sin\theta_r)e^{-jk\tilde{r}_r(y,z)}dydz, \tag{12}$$

$$\tilde{A}_\phi = \iint_{\mathcal{S}} J_y \cos\phi_r e^{-jk\tilde{r}_r(y,z)}dydz. \tag{13}$$

Using the radiation equations for any receive distance $r_r \gg \lambda$, we finally have [17, Eq. (6.122)]

$$\mathbf{E}_s = -\eta\frac{jke^{-jkr_r}}{4\pi r_r}(\tilde{A}_\theta\mathbf{e}_\theta + \tilde{A}_\phi\mathbf{e}_\phi). \tag{14}$$

Proposition 1. *The scattered E-field at the receive position* $(r_r \cos\phi_r \sin\theta_r, r_r \sin\phi_r \sin\theta_r, r_r \cos\theta_r)$*, when the IRS is illuminated by a spherical wave originated from* $(r_t \cos\phi_t \sin\theta_t, r_t \sin\phi_t \sin\theta_t, r_t \cos\theta_t)$*, is given by*

$$\mathbf{E}_s = -\frac{L_y L_z}{\lambda}\frac{|E_i|e^{-jk(r_t+r_r)}}{r_r}\cos\phi_t \sin\theta_r S_{yz}\mathbf{e}_\theta, \tag{15}$$

where $|E_i| = \sqrt{\frac{\eta P_t G_t}{4\pi r_t^2}}$ *is the magnitude of the incident field, and* $S_{yz} \in [0,1]$ *is the normalized space factor of the IRS specified by* (16) *at the bottom of the next page for*

$$\begin{aligned} a_y &= \frac{(1-\sin^2\phi_t\sin^2\theta_t)}{2r_t} + \frac{(1-\sin^2\phi_r\sin^2\theta_r)}{2r_r} - C_1, \\ b_y &= \sin\phi_t\sin\theta_t + \sin\phi_r\sin\theta_r + C_2, \end{aligned} \tag{17}$$

$$\begin{aligned} a_z &= \frac{\sin^2\theta_t}{2r_t} + \frac{\sin^2\theta_r}{2r_r} - C_3, \\ b_z &= \cos\theta_t + \cos\theta_r + C_4. \end{aligned} \tag{18}$$

Proof. See Appendix. □

Remark 1. *In the far-field, the parallel-ray approximations*

$$\tilde{r}_t(y,z) \approx -y\sin\phi_t\sin\theta_t - z\cos\theta_t, \tag{19}$$

$$\tilde{r}_r(y,z) \approx -y\sin\phi_r\sin\theta_r - z\cos\theta_r \tag{20}$$

are employed. Then, $a_y = a_z = 0$*, and the space factor reduces to [17]*

$$S_{yz} = \frac{\int_{-L_y/2}^{L_y/2}\int_{-L_z/2}^{L_z/2} e^{jk(b_y y + b_z z)}dydz}{L_y L_z} = \text{sinc}(Y)\text{sinc}(Z), \tag{21}$$

where $Y \triangleq kL_y b_y/2$ *and* $Z \triangleq kL_z b_z/2$*.*

From Proposition 1, the squared magnitude of the scattered E-field is calculated as

$$\|\mathbf{E}_s\|^2 = \left(\frac{L_y L_z}{\lambda}\right)^2 \frac{|E_i|^2}{r_r^2}\cos^2\phi_t \sin^2\theta_r |S_{yz}|^2, \tag{22}$$

where $|S_{yz}|^2$ is the normalized beampattern of the IRS.

C. End-to-End Signal Model

We now introduce the signal model of a holographic IRS-assisted THz system, where the transmitter (Tx) and receiver (Rx) are equipped with a single antenna each. First, recall the relation between the magnitude of the incident wave $|E_i|$ and the transmit power P_t, which is $|E_i|^2/\eta = G_t P_t/(4\pi r_t^2)$ [16]. Hence, the power density (W/m^2) of the scattered field is

$$S_s = \frac{\|\mathbf{E}_s\|^2}{\eta} = \left(\frac{L_y L_z}{\lambda}\right)^2 \frac{P_t G_t}{4\pi r_t^2 r_r^2}\cos^2\phi_t \sin^2\theta_r |S_{yz}|^2. \tag{23}$$

Considering the receive aperture $A_r = G_r\lambda^2/(4\pi)$ yields the received power $P_r = S_s A_r$. Lastly, taking into account the molecular absorption loss at THz frequencies results in the path loss of the Tx-IRS-Rx link

$$\begin{aligned}\overline{\text{PL}} &= G_t G_r \left(\frac{L_y L_z}{4\pi}\right)^2 \frac{\cos^2\phi_t \sin^2\theta_r}{r_t^2 r_r^2} e^{-\kappa_{\text{abs}}(f)(r_t+r_r)}|S_{yz}|^2 \\ &= \text{PL}|S_{yz}|^2, \end{aligned} \tag{24}$$

where $\kappa_{\text{abs}}(f)$ denotes the molecular absorption coefficient at the carrier frequency f. From (24), it is evident that the path loss of an IRS-assisted link follows the plate scattering paradigm. Combining (15) and (24), the baseband signal at the Rx is written as

$$y = \left(\sqrt{\text{PL}}e^{-jk(r_r+r_t)}S_{yz} + \sqrt{\text{PL}_d}e^{-jkr_d}\right)s + \tilde{n}, \tag{25}$$

where $s \sim \mathcal{CN}(0, P_t)$ is the transmitted data symbol, P_t is the average power per data symbol, r_d is the distance between the Tx and Rx, $\text{PL}_d = G_t G_r \lambda^2/(4\pi r_d)^2 e^{-\kappa_{\text{abs}}(f) r_d}$ is the path loss of the direct Tx-Rx channel, and $\tilde{n} \sim \mathcal{CN}(0, \sigma^2)$ is the additive noise.

III. Discussion

In this section, we discuss in detail the near-field channel model introduced in Section II.

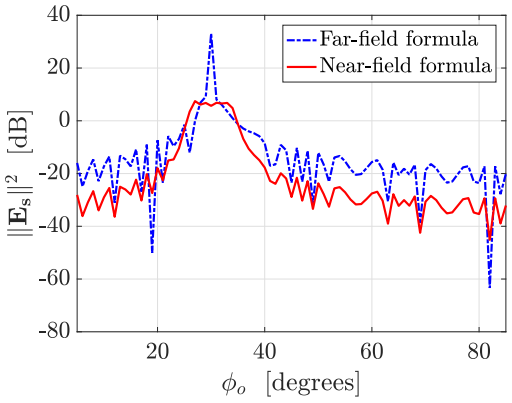

(a) $r_r = 2$ m and $r_o = 8$ m

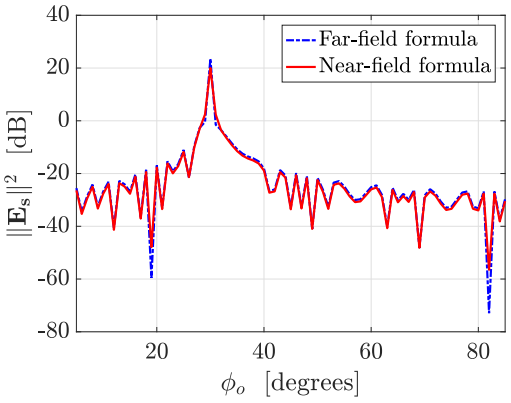

(b) $r_r = 6$ m and $r_o = 8$ m

Fig. 2: Squared magnitude of the scattered E-field versus observation angle ϕ_o; $|E_i| = 1$, $L_y = L_z = 200\lambda$, $f = 300$ GHz, $\phi_t = 36°$, $(\theta_r, \phi_r) = (45°, 30°)$, and $(\theta_o, \phi_o) = (45°, \phi_o)$.

A. Near-Field versus Far-Field Response

Consider the phase profile (9) with

$$C_1 = \frac{1 - \sin^2\phi_t \sin^2\theta_t}{2r_t} + \frac{1 - \sin^2\phi_o \sin^2\theta_o}{2r_o}, \tag{26}$$

$$C_2 = -\sin\phi_t \sin\theta_t - \sin\phi_o \sin\theta_o, \tag{27}$$

$$C_3 = \frac{\sin^2\theta_t}{2r_t} + \frac{\sin^2\theta_o}{2r_o}, \tag{28}$$

$$C_4 = -\cos\theta_t - \cos\theta_o, \tag{29}$$

where $(r_o \cos\phi_o \sin\theta_o, r_o \sin\phi_o \sin\theta_o, r_o \cos\theta_o)$ is an arbitrary observation position, with r_o, ϕ_o, and θ_o denoting the corresponding radial distance, azimuth angle, and polar angle, respectively. Then, the parameters of the beampattern $|S_{yz}|^2$ are

$$a_y = \frac{1 - \sin^2\phi_r \sin^2\theta_r}{2r_r} - \frac{1 - \sin^2\phi_o \sin^2\theta_o}{2r_o}, \tag{30}$$

$$b_y = \sin\phi_r \sin\theta_r - \sin\phi_o \sin\theta_o, \tag{31}$$

$$a_z = \frac{\sin^2\theta_r}{2r_r} - \frac{\sin^2\theta_o}{2r_o}, \tag{32}$$

$$b_z = \cos\theta_r - \cos\theta_o. \tag{33}$$

We now plot the squared magnitude of the scattered E-field for the considered $\varphi(y, z)$. From Fig. 2, we first observe that the peak value is at $\phi_o = \phi_r = 30°$, as expected. From Fig. 2(a), however, we see a mismatch between the near and far scattered fields of a large IRS. This discrepancy is due to the spherical wavefront of the incident wave, which makes the beampattern $|S_{xy}|^2$ depend on the angles of arrival/departure as well as the distances between the IRS, the Rx, and the observation point. This unique feature manifests only in the near-field [18]. It is finally worth stressing that the near-field space factor in (16) coincides with its far-field counterpart (21) for either an electrically small IRS or relatively large distances r_r and r_o, i.e., Fig. 2(b).

B. Discrete IRS

It might be difficult to implement a holographic IRS in practice. Therefore, a contiguous IRS of size $L_y \times L_z$ can be approximated by a planar array of $N_y = L_y/\tilde{L}_y$ and $N_z = L_z/\tilde{L}_z$ reflecting elements, each of size $\tilde{L}_y \times \tilde{L}_z$; the inter-element spacing is negligible, and hence is ignored. Then, (22) is recast as

$$\|\mathbf{E}_s\|^2 = N_y^2 N_z^2 \left(\frac{\tilde{L}_y \tilde{L}_z}{\lambda}\right)^2 \frac{|E_i|^2}{r_o^2} \cos^2\phi_t \sin^2\theta_r |S_{yz}|^2, \tag{34}$$

where

$$S_{yz} = \frac{\sum_{n=-\frac{N_y}{2}}^{\frac{N_y}{2}-1} e^{-jk\left((n\tilde{L}_y)^2 a_y - n\tilde{L}_y b_y\right)}}{N_y} \times \frac{\sum_{m=-\frac{N_z}{2}}^{\frac{N_z}{2}-1} e^{-jk\left((m\tilde{L}_z)^2 a_z - m\tilde{L}_z b_z\right)}}{N_z}, \tag{35}$$

which follows from (41) in the appendix for $y = n\tilde{L}_y$, $z = m\tilde{L}_z$, $L_y = N_y\tilde{L}_y$, $L_z = N_z\tilde{L}_z$, $dy = \tilde{L}_y$, and $dz = \tilde{L}_z$. Likewise, the reflection coefficient of the (n, m)th IRS element is defined as $e^{j\varphi_{n,m}}$, where $\varphi_{n,m} \triangleq \varphi(n\tilde{L}_y, m\tilde{L}_z)$. For a

$$S_{yz} = \frac{\pi}{4jkL_yL_z\sqrt{a_ya_z}} \left[\text{erf}\left(\sqrt{jka_y}\left(\frac{L_y}{2} - \frac{b_y}{2a_y}\right)\right) - \text{erf}\left(\sqrt{jka_y}\left(-\frac{L_y}{2} - \frac{b_y}{2a_y}\right)\right)\right] \times \left[\text{erf}\left(\sqrt{jka_z}\left(\frac{L_z}{2} - \frac{b_z}{2a_z}\right)\right) - \text{erf}\left(\sqrt{jka_z}\left(-\frac{L_z}{2} - \frac{b_z}{2a_z}\right)\right)\right]. \tag{16}$$

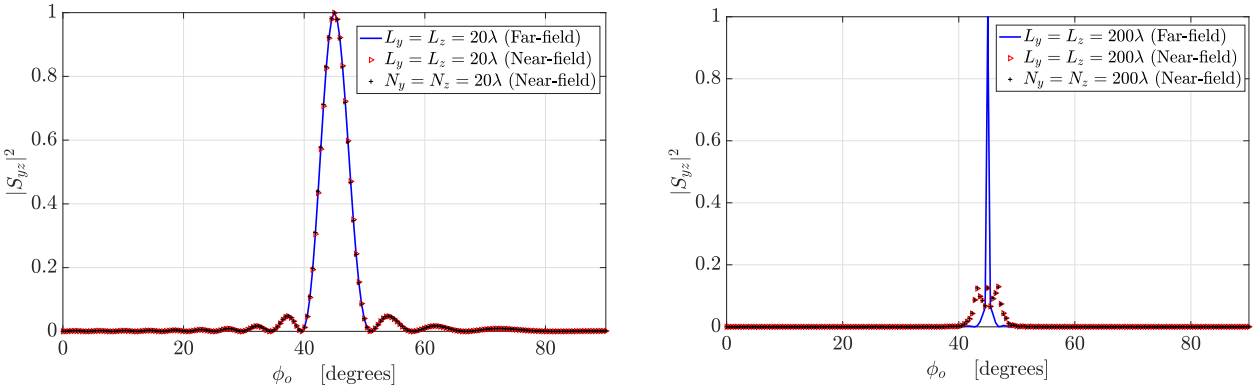

(a) Small IRS

(b) Large IRS

Fig. 3: Normalized beampattern of holographic IRS and discrete IRS versus observation angle ϕ_o; $\tilde{L}_y = \tilde{L}_z = \lambda$, $(r_r, \theta_r, \phi_r) = (2, 45°, 45°)$, $(r_o, \theta_o, \phi_o) = (8, \theta_o, 45°)$, and $f = 300$ GHz.

discrete IRS, when the observation direction coincides with that of the Rx, $a_y = b_y = a_z = b_z = 0$, $S_{yz} = 1$, and a power gain of $(N_y N_z)^2$ is attained over the Tx-IRS-Rx link.

C. Beamfocusing Capabilities

With proper design of the phase profile $\varphi(y, z)$, we can cancel out the incident phase and focus the beam into the Rx point (r_r, θ_r, ϕ_r).[3] As previously shown, the peak value of $|S_{yz}|^2$ occurs at $(r_o, \theta_o, \phi_o) = (r_r, \theta_r, \phi_r)$. From Fig. 3(a) and Fig. 3(b), we first observe the excellent match between a holographic IRS and its discrete counterpart with a negligible inter-element spacing. This implies that we can properly discretize the holographic IRS without sacrificing its extremely high spatial resolution. Consequently, (16) and (35) can be used interchangeably. We further see that the electrically large IRS can discriminate two points with the same angular direction $(\theta_o, \phi_o) = (\theta_r, \phi_r)$ but with different distances $r_o \neq r_r$; asymptotically, we have $|S_{yz}|^2 \to 0$ as $L_y L_z \to \infty$. The beamfocusing capability can be exploited in multi-user transmissions to suppress interference with an unprecedented way. For example, consider an uplink scenario where two users, user 1 and user 2, simultaneously transmit. Their positions from the IRS are (r_1, θ_1, ϕ_1) and (r_2, θ_2, ϕ_2), with $(\theta_1, \phi_1) = (\theta_2, \phi_2)$ and $r_1 \neq r_2$. In the far-field, $|S_{yz}|^2 = 1$, and hence we will have strong inter-user interference at the Rx. Conversely, in the near-field, $|S_{yz}|^2 < 1$ and the inter-user interference becomes small at the Rx.

D. Scattering versus Antenna-Based Path Loss Models

Some works in the literature (e.g., [11]) treat an IRS element as a standard antenna that re-radiates the impinging wave. In this case, the path loss is calculated as

$$\text{PL}' = G_t G_r \left(\frac{\lambda}{4\pi}\right)^4 \frac{G_e(\theta_t) G_e(\theta_r)}{r_t^2 r_r^2} e^{-\kappa_{\text{abs}}(f)(r_t + r_r)}, \quad (36)$$

[3]This is in sharp contrast to traditional beamforming, where the IRS acts as an anomalous reflector that focuses the signal into a desired direction (θ_r, ϕ_r), rather than into a point (r_r, θ_r, ϕ_r) [20].

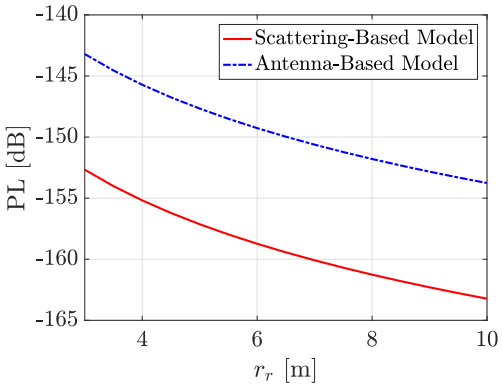

Fig. 4: In the antenna-based model [11], $G_e(\theta) = \gamma \cos^{2q}\theta$, with $\gamma = \pi$ and $q = 0.285$. The other parameters are: $f = 300$ GHz, $L_y = L_z = \lambda/2$, $r_t = 2$ m, $(\theta_t, \phi_t) = (60°, 90°)$, $(\theta_r, \phi_r) = (45°, 90°)$, $G_t = 20$ dBi, $G_r = 0$ dBi, and $\kappa_{\text{abs}}(f) = 0.0033$ m^{-1}.

where $G_e(\cdot)$ is the radiation pattern of each IRS element. For a sub-wavelength reflecting element, it holds $|S_{yz}|^2 \approx 1$, and $\text{PL} = G_t G_r \left(\frac{L_y L_z}{4\pi}\right)^2 \frac{\cos^2\phi_t \sin^2\theta_r}{r_t^2 r_r^2} e^{-\kappa_{\text{abs}}(f)(r_t + r_r)} \neq \text{PL}'$, as shown in Fig. 4. Consequently, conventional antenna-based models may not always capture the unique features of IRS-aided links.

IV. Conclusions

We have studied, for the first time, the near-field response of holographic IRSs operating at the THz frequency band. To have a physics-consistent channel model, we leveraged EM theory and derived a novel closed-form expression for the scattered field. Unlike existing works, our model accounts for arbitrary incident and reflection angles. Capitalizing on our analysis, we then compared the near-field response with its far-field counterpart and revealed a significant discrepancy, which makes the use of the former necessary for electrically large IRSs. We finally discussed the beamfocusing property, which

manifests on the near-field regime, and highlighted its potential in multi-user transmissions and interference suppression. For future work, it would be interesting to study the coupling effects in ultra-dense discrete IRSs and their connection with super-directive antenna arrays. Moreover, it would be interesting to derive a circuit theory-based model for the power consumption of THz IRSs.

ACKNOWLEDGEMENTS

This project has received funding from the European Research Council (ERC) under the European Union's Horizon 2020 research and innovation programme (grant agreement No. 101001331).

APPENDIX

The magnetic field in (4) is written in Cartesian coordinates as

$$\mathbf{H}_i = -H_\phi \sin\phi_t \mathbf{e}_x + H_\phi \cos\phi_t \mathbf{e}_y. \tag{37}$$

The current density induced on the IRS is

$$\begin{aligned}\mathbf{J}(y,z) &= (2\mathbf{e}_x \times \mathbf{H}_i|_{x=0}) e^{j\varphi(y,z)} \\ &= 2H_\phi \cos\phi_t e^{j\varphi(y,z)} \mathbf{e}_z \\ &= \frac{2j}{\eta}\sqrt{\frac{\eta P_t G_t}{4\pi}} \frac{e^{-jkr_t}}{r_t} e^{-jk\tilde{r}_t(y,z)} \cos\phi_t e^{j\varphi(y,z)} \mathbf{e}_z \\ &= \frac{2j}{\eta} E_i e^{-jk\tilde{r}_t(y,z)} \cos\phi_t e^{j\varphi(y,z)} \mathbf{e}_z \\ &= J_z e^{j\varphi(y,z)} \mathbf{e}_z, \end{aligned} \tag{38}$$

where $E_i = \sqrt{\frac{\eta P_t G_t}{4\pi}} \frac{e^{-jkr_t}}{r_t}$. Then, (12) and (13) give

$$\tilde{A}_\theta = -jL_yL_z \frac{2E_i}{\eta} \cos\phi_t \sin\theta_r S_{yz}, \tag{39}$$

$$\tilde{A}_\phi = 0, \tag{40}$$

where

$$\begin{aligned} S_{yz} &= \frac{\iint_{\mathcal{S}} e^{-jk(\tilde{r}_t(y,z)+\tilde{r}_r(y,z)-\varphi(y,z)/k)} ds}{L_yL_z} \\ &= \frac{\int_{-L_y/2}^{L_y/2}\int_{-L_z/2}^{L_z/2} e^{-jk(a_y y^2 - b_y y + a_z z^2 - b_z z)} dydz}{L_yL_z}, \end{aligned} \tag{41}$$

with

$$a_y = \frac{(1-\sin^2\phi_t \sin^2\theta_t)}{2r_t} + \frac{(1-\sin^2\phi_r \sin^2\theta_r)}{2r_r} - C_1,$$

$$b_y = \sin\phi_t \sin\theta_t + \sin\phi_r \sin\theta_r + C_2, \tag{42}$$

$$a_z = \frac{\sin^2\theta_t}{2r_t} + \frac{\sin^2\theta_r}{2r_r} - C_3, \tag{43}$$

$$b_z = \cos\theta_t + \cos\theta_r + C_4. \tag{44}$$

We now use the identity

$$\int e^{-jk(ay^2-by)} dy = \frac{\sqrt{\pi}}{2\sqrt{jka}} \text{erf}\left(\sqrt{jka}\left(y - \frac{b}{2a}\right)\right), \tag{45}$$

which follows from the definition of the error function, some algebrain manipulations, and a change of variables. Using (45), the expression (16) for S_{yz} is derived. The scattered E-field is finally given by

$$\begin{aligned}\mathbf{E}_s &= -\eta \frac{jke^{-kjr_r}}{4\pi r_r}(\tilde{A}_\theta \mathbf{e}_\theta + \tilde{A}_\phi \mathbf{e}_\phi) \\ &= \frac{j^2 L_y L_z k E_i e^{-kj(r_t+r_r)}}{2\pi r_r} \cos\phi_t \sin\theta_r S_{yz} \mathbf{e}_\theta \\ &= -\frac{L_yL_z}{\lambda} \frac{|E_i| e^{-kj(r_t+r_r)}}{r_r} \cos\phi_t \sin\theta_r S_{yz} \mathbf{e}_\theta, \end{aligned} \tag{46}$$

which completes the proof.

REFERENCES

[1] T. S. Rappaport *et al*., "Wireless communications and applications above 100 GHz: Opportunities and challenges for 6G and beyond," *IEEE Access*, vol. 7, pp. 78729-78757, 2019.

[2] J. Zhang *et al*., "Prospective multiple antenna technologies for beyond 5G," *IEEE J. Sel. Areas Commun.*, vol. 38, no. 8, pp. 1637–1660, Aug. 2020.

[3] K. Dovelos, M. Matthaiou, H. Q. Ngo, and B. Bellalta, "Channel estimation and hybrid combining for wideband terahertz massive MIMO systems," *IEEE J. Sel. Areas Commun*., Apr. 2021.

[4] M. D. Renzo *et al*., "Smart radio environments empowered by reconfigurable intelligent surfaces: How it works, state of research, and road ahead," *IEEE J. Sel. Areas Commun*., vol. 38, no. 11, pp. 2450–2525, Nov. 2020.

[5] M. Di Renzo *et al*., "Reconfigurable intelligent surfaces vs. relaying: Differences, similarities, and performance comparison," *IEEE Open J. Commun. Soc*., vol. 1, pp. 798-807, 2020.

[6] K. Ntontin *et al.*, "Reconfigurable intelligent surface optimal placement in millimeter-wave networks," *Open J. Commun. Soc.*, vol. 2, pp. 704-718, Mar. 2021.

[7] A.-A. A. Boulogeorgos and A. Alexiou, "Coverage analysis of reconfigurable intelligent surface assisted THz wireless systems," *IEEE Open J. Veh. Technol.*, vol. 2, pp. 94-110, Jan. 2021.

[8] Ö. Özdogan, E. Björnson, and E. G. Larsson, "Intelligent reflecting surfaces: Physics, propagation, and pathloss modeling," *IEEE Wireless Commun. Lett.*, vol. 9, no. 5, pp. 581-585, May 2020.

[9] M. Najafi, V. Jamali, R. Schober, and H. V. Poor, "Physics-based modeling and scalable optimization of large intelligent reflecting surfaces," *IEEE Trans. Commun.*, vol. 69, no. 4, pp. 2673-2691, Apr. 2021.

[10] C. Huang *et al*., "Holographic MIMO surfaces for 6G wireless networks: Opportunities, challenges, and trends," *IEEE Wireless Commun.*, vol. 27, no. 5, pp. 118-125, Oct. 2020.

[11] S. W. Ellingson, "Path loss in reconfigurable intelligent surface-enabled channels," *arXiv preprint* arXiv:1912.06759, 2019.

[12] W. Tang *et al*., "Wireless communications with reconfigurable intelligent surface: Path loss modeling and experimental measurement," *IEEE Trans. Wireless Commun.*, vol. 20, no. 1, pp. 421-439, Jan. 2021.

[13] K. Dovelos, S. D. Assimonis, H. Q. Ngo, B. Bellalta, and M. Matthaiou, "Intelligent reflecting surfaces at terahertz bands: Channel modeling and analysis," to appear in *Proc. IEEE ICC*, 2021.

[14] E. Björnson and L. Sanguinetti, "Power scaling laws and near-field behaviors of massive MIMO and intelligent reflecting surfaces," *IEEE Open J. Commun. Soc*., vol. 1, pp. 1306–1324, 2020.

[15] Z. Wan, Z. Gao, M. Di Renzo, and M.-S. Alouini, "Terahertz massive MIMO with holographic reconfigurable intelligent surfaces," *IEEE Trans. Commun.*, Mar. 2021.

[16] C. A. Balanis, *Antenna Theory: Analysis and Design*, John Wiley & Sons, 2012.

[17] C. A. Balanis, *Advanced Engineering Electromagnetics*, 2nd ed. John Wiley & Sons, 2012.

[18] O. Yurduseven, S. D. Assimonis, and M. Matthaiou, "Intelligent reflecting surfaces with spatial modulation: An electromagnetic perspective," *IEEE Open J. Commun. Soc*., vol. 1, pp. 1256–1266, Sep. 2020.

[19] A. V. Osipov and S. A. Tretyakov, *Modern Electromagnetic Scattering Theory with Applications*, John Wiley, 2017.

[20] E. Björnson, Ö. Özdogan, and E. G. Larsson, "Reconfigurable intelligent surfaces: Three myths and two critical questions," *IEEE Commun. Mag.*, vol. 58, no. 12, pp. 90-96, Dec. 2020.

Paper IV

Intelligent Reflecting Surface-Aided Wideband THz Communications: Modeling and Analysis

Konstantinos Dovelos*, Stylianos D. Assimonis†, Hien Quoc Ngo†, Boris Bellalta*, and Michail Matthaiou†
*Department of Information and Communication Technologies, Universitat Pompeu Fabra (UPF), Barcelona, Spain
†Institute of Electronics, Communications and Information Technology (ECIT), Queen's University Belfast, Belfast, U.K.
Email: {konstantinos.dovelos, boris.bellalta}@upf.edu, {s.assimonis, hien.ngo, m.matthaiou}@qub.ac.uk

***Abstract*—In this paper, we study the performance of wideband terahertz (THz) communications assisted by an intelligent reflecting surface (IRS). For this purpose, we first introduce a generalized channel model that is suitable for electrically large THz IRSs operating in the near-field. Specifically, our channel model takes into account the spherical wavefront of the radiated waves, as well as the spatial-wideband effect. We next show that conventional frequency-flat beamfocusing is highly suboptimal for wideband transmissions, and thus can significantly reduce the power gain. More importantly, we derive an approximate yet accurate closed-form expression to quantify this reduction. Numerical results corroborate our analysis and provide novel insights into the design of future IRS-aided wideband THz systems.**

***Index Terms*—Beamfocusing, beam squint, intelligent reflecting surfaces, near-field, wideband THz communications.**

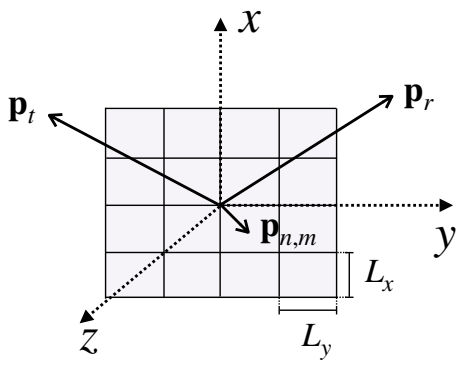

Fig. 1: Illustration of the IRS geometry under consideration.

I. Introduction

Undoubtedly, spectrum scarcity constitutes the main bottleneck of current wireless communication systems. To alleviate this problem, communication over the terahertz (THz) band, spanning from 0.1 to 10 THz, is favored for 6G-and-beyond networks due to the abundant spectrum available at high frequencies [1]. Despite the potential for terabit-per-second wireless links, THz signals suffer from severe propagation losses because of their short wavelength. As a result, the deployment of transceivers with a massive number of antennas is necessary to compensate for these propagation losses by means of sharp beamforming [2]. On the other hand, the power consumption of THz radio-frequency circuits is much higher than their sub-6 GHz counterparts, which might undermine the deployment of large-scale antenna arrays in an energy efficient manner [3]. To this end, the novel technology of intelligent reflecting surfaces (IRSs) can be exploited to achieve high spectral efficiency with reduced power consumption [4]. Thus, the performance analysis of IRS-aided THz communications is of great research importance.

The ultra-wide bandwidths, e.g., tens of gigahertz, of future THz systems in conjunction with the large number of IRS elements can yield a *spatially wideband* channel [5], where the power gain varies across the signal bandwidth. Moreover, an electrically large THz IRS is likely to operate in the radiating near-field, i.e., Fresnel zone, where the spherical wavefront of the emitted electromagnetic waves cannot be ignored [6]. Under these circumstances, frequency-flat beamfocusing can substantially decrease the power gain due to beam squint. To the best of our knowledge, though, existing studies on IRSs (e.g., [6]–[12], and references therein) ignore the spatial-wideband effect and its impact on system performance. This paper aims to fill this gap in the literature, and shed light on the channel modeling and performance of IRS-assisted wideband THz communications. To this end, we first introduce a spherical wave channel model for IRS-aided THz links, which takes into account the spatial-wideband effect. Hence, our model is applicable to the near-field region, which includes far-field as a special case. We next analyze the power gain under conventional narrowband beamfocusing, and show that it is highly suboptimal. Most importantly, we analytically evaluate the reduction in the power gain by providing an approximate closed-form expression. Moreover, by availing of the derived expression, we prove that the achievable rate does not always grow without bound as the number of IRS elements increases due to the spatial-wideband effect. Our performance analysis reveals that beam squint mitigation through a frequency-selective surface design is essential for reaping the full potential of IRS-aided wideband THz systems.

Notation: $\mathbf{X}$ is a matrix; $\mathbf{x}$ is a vector; x and X are scalars; $(\cdot)^*$, $(\cdot)^T$, and $(\cdot)^H$ are the conjugate, transpose and conjugate transpose, respectively; $[\mathbf{X}]_{i,j}$ is the (i,j)th entry of $\mathbf{X}$; $\mathrm{vec}(\mathbf{X})$ is the column vector formed by stacking the columns of $\mathbf{X}$; $\mathcal{F}\{\cdot\}$ is the continuous-time Fourier transform; $\mathbf{x} \sim \mathcal{CN}(\boldsymbol{\mu}, \boldsymbol{\Sigma})$ is a complex Gaussian vector with mean $\boldsymbol{\mu}$ and covariance matrix $\boldsymbol{\Sigma}$; and $\mathrm{erf}(x) = \frac{2}{\sqrt{\pi}} \int_0^x e^{-t^2} dt$ is the error function.

II. Channel Model with Spatial-Wideband Effects

A. System Setup

Consider an IRS-aided THz system, where the transmitter (Tx) and receiver (Rx) have a single antenna each. The IRS is placed in the xy-plane, and it consists of $N = N_x \times N_y$ passive reflecting elements of size $L_x \times L_y$ each, as depicted in Fig. 1; the inter-element spacing is negligible, and hence is ignored [12]. The origin of the coordinate system is placed at the center of the IRS. The position of each IRS element is measured from its center. Then, the position vector of the (n,m)th IRS element is $\mathbf{p}_{n,m} = ((n-1/2)L_x, (m-1/2)L_y, 0)$, for $n = -\frac{N_x}{2}, \ldots, \frac{N_x}{2}-1$, and $m = -\frac{N_y}{2}, \ldots, \frac{N_y}{2}-1$. Likewise, $\mathbf{p}_t = (r_t, \theta_t, \phi_t)$ and $\mathbf{p}_r = (r_r, \theta_r, \phi_r)$ are the position vectors of the Tx and Rx, respectively, where r is the radial distance, θ is the polar angle, and ϕ is the azimuth angle. In Cartesian coordinates, the distance between the Tx and the (n,m)th IRS element is hence given by

$$\begin{aligned} r_t(n,m) &\triangleq \|\mathbf{p}_t - \mathbf{p}_{n,m}\| \\ &= r_t \left(1 + \frac{\left((n-\frac{1}{2})L_x\right)^2}{r_t^2} - \frac{2\cos\phi_t \sin\theta_t (n-\frac{1}{2})L_x}{r_t} \right. \\ &\left. + \frac{\left((m-\frac{1}{2})L_y\right)^2}{r_t^2} - \frac{2\sin\phi_t \sin\theta_t (m-\frac{1}{2})L_y}{r_t}\right)^{1/2}. \end{aligned} \quad (1)$$

The distance between the Rx and the (n,m)th IRS element, $r_r(n,m) \triangleq \|\mathbf{p}_r - \mathbf{p}_{n,m}\|$, is specified in a similar manner.

B. Channel Model

We focus on the Tx-IRS-Rx link. The received baseband signal propagated through the IRS is expressed as

$$r(t) = \sum_{n=-\frac{N_x}{2}}^{\frac{N_x}{2}-1} \sum_{m=-\frac{N_y}{2}}^{\frac{N_y}{2}-1} h_{n,m} e^{j\varphi_{n,m}} x(t - \tau_{n,m}) + \tilde{n}(t), \quad (2)$$

where $e^{j\varphi_{n,m}}, \varphi_{n,m} \in [-\pi, \pi]$, is the reflection coefficient of the (n,m)th IRS element, $\tilde{n}(t) \sim \mathcal{CN}(0, \sigma^2)$ is the additive noise at the receive end, $x(t)$ is the transmitted baseband signal, and $\tau_{n,m}$ is the associated propagation delay given by

$$\tau_{n,m} = \frac{r_r(n,m) + r_t(n,m)}{c}, \quad (3)$$

where c denotes the speed of light. Moreover,

$$h_{n,m} = \sqrt{\mathrm{PL}_{n,m}(f)} e^{-j2\pi f_c \tau_{n,m}} \quad (4)$$

is the cascaded channel through the (n,m)th IRS element, $\mathrm{PL}_{n,m}(f)$ is the corresponding frequency-dependent path loss, and f_c is the carrier frequency. The path loss of the cascaded channel through the (n,m)th IRS element is calculated as [6]

$$\mathrm{PL}_{n,m}(f) = G_t G_r \left(\frac{L_x L_y}{4\pi}\right)^2 \frac{F(\theta_t, \phi_r, \theta_r)}{r_t^2(n,m) r_r^2(n,m)} e^{-\kappa_{\text{abs}}(f)(r_t(n,m) + r_r(n,m))}, \quad (5)$$

where $F(\theta_t, \phi_r, \theta_r) \triangleq \cos^2\theta_t (\cos^2\theta_r \cos^2\phi_r + \sin^2\phi_r)$, G_t and G_r are the Tx and Rx antenna gains, respectively, while $\kappa_{\text{abs}}(f)$ denotes the molecular absorption coefficient at frequency f. Taking the Fourier transform of (2) gives

$$R(f) \approx \sqrt{\mathrm{PL}(f)} \underbrace{\sum_{n=-\frac{N_x}{2}}^{\frac{N_x}{2}-1} \sum_{m=-\frac{N_y}{2}}^{\frac{N_y}{2}-1} e^{-j2\pi(f_c+f)\tau_{n,m}} e^{j\varphi_{n,m}}}_{H_{\text{eff}}(f)} X(f) + \tilde{N}(f), \quad (6)$$

where the approximation follows from $\mathrm{PL}_{n,m}(f) \approx \mathrm{PL}(f)$ owing to the small physical size of THz IRSs [6], $\mathrm{PL}(f)$ denotes the path loss calculated using the radial distances r_t and r_r, $\mathcal{F}\{r(t)\} = R(f)$, $\mathcal{F}\{x(t)\} = X(f)$, $\mathcal{F}\{\tilde{n}(t)\} = \tilde{N}(f)$, and $H_{\text{eff}}(f)$ is the effective channel accounting for the phase shifts. Note that $H_{\text{eff}}(f)$ is frequency-dependent because of the spatial-wideband effect. Next, consider orthogonal frequency division multiplexing (OFDM) modulation with S subcarriers for a signal bandwidth B. The subcarrier spacing is $\Delta\mathrm{B} = B/S$, and the baseband frequency of the sth subcarrier is specified as $f_s = \left(s - \frac{S-1}{2}\right)\Delta\mathrm{B}$, for $s = 0, \ldots, S-1$. Hence, the received signal at the sth subcarrier is given by

$$R(f_s) = \sqrt{\mathrm{PL}(f_s)} H_{\text{eff}}(f_s) X(f_s) + \tilde{N}(f_s), \quad (7)$$

where $X(f_s) \sim \mathcal{CN}(0, P_t/S)$ is the transmitted data symbol with average power P_t/S, and $\tilde{N}(f_s) \sim \mathcal{CN}(0, \sigma^2\Delta\mathrm{B})$ is the additive noise at each subcarrier.

Remark 1 (Fresnel Approximation)**.** *In the near-field, the Tx distance can be approximated by* $r_t(n,m) \approx r_t + \tilde{r}_t(n,m)$*, where*

$$\begin{aligned} \tilde{r}_t(n,m) &= \frac{\left((n-\frac{1}{2})L_x\right)^2 (1 - \cos^2\phi_t \sin^2\theta_t)}{2r_t} \\ &- \left(n - \frac{1}{2}\right) L_x \cos\phi_t \sin\theta_t \\ &+ \frac{\left((m-\frac{1}{2})L_y\right)^2 (1 - \sin^2\phi_t \sin^2\theta_t)}{2r_t} \\ &- \left(m - \frac{1}{2}\right) L_y \sin\phi_t \sin\theta_t \end{aligned} \quad (8)$$

follows from the second-order Taylor polynomial $(1+x)^\alpha \approx 1 + \alpha x + \frac{1}{2}\alpha(\alpha-1)x^2$ *of* (1)*. Similarly, it holds* $r_r(n,m) \approx r_r + \tilde{r}_r(n,m)$*, where* $\tilde{r}_r(n,m)$ *is given by* (8)*, but* θ_t*,* ϕ_t*, and* r_t *are replaced by* θ_r*,* ϕ_r*, and* r_r*, respectively.*

III. Performance Analysis of IRS-aided Wideband THz Communications

A. Power Gain

From (6), the signal-to-noise ratio (SNR) at the sth OFDM subcarrier can be written as

$$\mathrm{SNR}_s = \frac{N^2 G_s P_t \mathrm{PL}(f_s)}{B\sigma^2}, \quad (9)$$

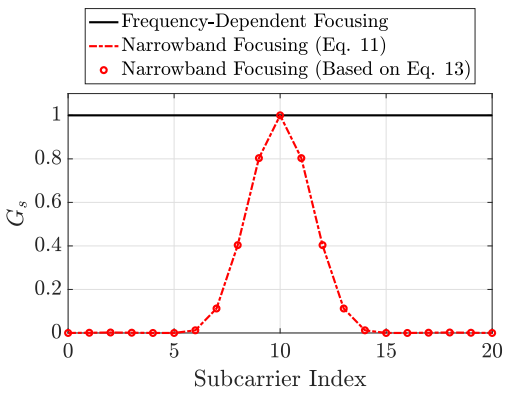

(a)

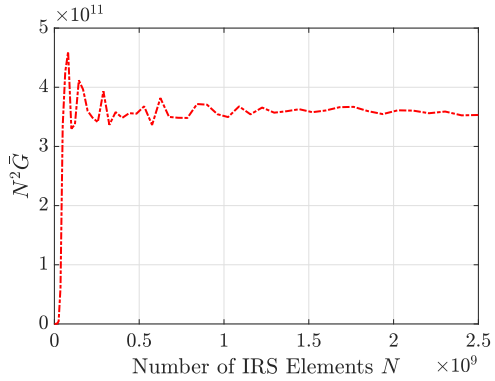

(b)

Fig. 2: Results for $B = 20$ GHz, $f_c = 300$ GHz, $(r_t, \theta_t, \phi_t) = (1, \pi/3, \pi/5)$, and $(r_r, \theta_r, \phi_r) = (5, \pi/4, \pi/3)$: (a) normalized power gain for an 80×80-element IRS; and (b) average power gain versus the number of IRS elements.

where $G_s \in [0, 1]$ is the normalized power gain defined as

$$G_s \triangleq \frac{|H_{\text{eff}}(f_s)|^2}{N^2}. \tag{10}$$

With frequency-dependent beamfocusing, the phase induced by the (n, m)th IRS element is $\varphi_{n,m}(f_s) = 2\pi(f_c + f_s)\tau_{n,m}$, which yields $G_s = 1$ for each OFDM subcarrier. Therefore, SNR_s grows quadratically with the number N of IRS elements. Conversely, with conventional narrowband beamfocusing, we have $\varphi_{n,m} = 2\pi f_c \tau_{n,m}$ for all subcarriers, and

$$G_s = \frac{1}{N_x^2 N_y^2} \left| \sum_{n=-\frac{N_x}{2}}^{\frac{N_x}{2}-1} \sum_{m=-\frac{N_y}{2}}^{\frac{N_y}{2}-1} e^{-j2\pi f_s \tau_{n,m}} \right|^2, \tag{11}$$

which results in $G_s < 1$ for $f_s > 0$. To evaluate that loss in the power gain, we leverage the Fresnel approximations of $r_t(n, m)$ and $r_r(n, m)$ introduced in Remark 1. Then, (11) is recast as

$$G_s \approx \frac{1}{N_x^2 N_y^2} \left| \sum_{n=-\frac{N_x}{2}}^{\frac{N_x}{2}-1} \sum_{m=-\frac{N_y}{2}}^{\frac{N_y}{2}-1} e^{-j2\pi f_s \frac{\tilde{r}_t(n,m)+\tilde{r}_r(n,m)}{c}} \right|^2. \tag{12}$$

Proposition 1. *The normalized power gain at the sth OFDM subcarrier is specified in closed-form as $G_s = |\xi_s|^2$, where ξ_s is given by* (13) *at the top of the next page for $k_s = 2\pi f_s/c$, $\tilde{L}_x = N_x L_x$, $\tilde{L}_y = N_y L_y$, and*

$$a_x = \frac{(1 - \cos^2\phi_t \sin^2\theta_t)}{2r_t} + \frac{(1 - \cos^2\phi_r \sin^2\theta_r)}{2r_r}, \tag{14}$$

$$b_x = \cos\phi_t \sin\theta_t + \cos\phi_r \sin\theta_r, \tag{15}$$

$$a_y = \frac{(1 - \sin^2\phi_t \sin^2\theta_t)}{2r_t} + \frac{(1 - \sin^2\phi_r \sin^2\theta_r)}{2r_r}, \tag{16}$$

$$b_y = \sin\phi_t \sin\theta_t + \sin\phi_r \sin\theta_r. \tag{17}$$

Proof. See Appendix. □

From Fig. 2(a), we observe the detrimental effect of beam squint for different transmission bandwidths. We next verify the excellent match between the exact expression of G_s and the closed-form formula in Proposition 1. By availing of (13), we have the asymptotic behavior $G_s \to 0$ as $N \to \infty$, which follows from the boundness of the error function. Moreover, using the closed-form formula, we plot the average power gain $N^2\bar{G}$ versus N, where $\bar{G} \triangleq \sum_{s=0}^{S-1} G_s/S$. From Fig. 2(b), it is evident that the average power gain can be bounded as $N^2\bar{G} \le G_{\max}$, for some $G_{\max} > 0$. Then,

$$\begin{aligned} R &= \sum_{s=0}^{S-1} \frac{B}{S} \log_2\left(1 + \frac{N^2 G_s P_t \text{PL}(f_s)}{B\sigma^2}\right) \\ &\overset{(a)}{\le} B \log_2\left(1 + \frac{1}{S}\sum_{s=0}^{S-1} \frac{N^2 G_s P_t \text{PL}(f_s)}{B\sigma^2}\right) \\ &\le B \log_2\left(1 + \frac{1}{S}\sum_{s=0}^{S-1} \frac{N^2 G_s P_t \max_s\{\text{PL}(f_s)\}}{B\sigma^2}\right) \\ &= B \log_2\left(1 + \frac{N^2 \bar{G} P_t \max_s\{\text{PL}(f_s)\}}{B\sigma^2}\right), \end{aligned} \tag{18}$$

where (a) follows from the inequality of arithmetic and geometric means. From (18), it is straightforward to see that $R \le B \log_2\left(1 + \frac{G_{\max} P_t \max_s\{\text{PL}(f_s)\}}{B\sigma^2}\right)$. Consequently, the achievable rate does not grow without bound as the number N of IRS elements increases. This result comes in sharp contrast to the spatially narrowband case, where increasing N would bring huge spectral and energy efficiency (EE) gains [6].

B. Achievable Rate via Beamfocusing Optimization

To improve the system performance, we can resort to a more advanced IRS design than narrowband beamfocusing. To this end, we introduce the auxiliary matrices $\mathbf{A}_s \in \mathbb{C}^{N_x \times N_y}$, with $[\mathbf{A}_s]_{n,m} = e^{-j2\pi f_s \tau_{n,m}}$, and $\mathbf{B} \in \mathbb{C}^{N_x \times N_y}$, with $[\mathbf{B}]_{n,m} = e^{j\varphi_{n,m}}$. Then, we have $|H_{\text{eff}}(f_s)|^2 = |\mathbf{h}_s^T \mathbf{b}|^2$, where $\mathbf{h}_s = \text{vec}(\mathbf{A}_s) \in \mathbb{C}^{N \times 1}$ and $\mathbf{b} = \text{vec}(\mathbf{B}) \in \mathbb{C}^{N \times 1}$. We seek to

$$\xi_s = \frac{\pi}{4jk_s\tilde{L}_x\tilde{L}_y\sqrt{a_xa_y}}\left[\text{erf}\left(\sqrt{jk_sa_x}\left(\frac{\tilde{L}_x}{2}-\frac{b_x}{2a_x}\right)\right)-\text{erf}\left(\sqrt{jk_sa_x}\left(-\frac{\tilde{L}_x}{2}-\frac{b_x}{2a_x}\right)\right)\right]$$
$$\times\left[\text{erf}\left(\sqrt{jk_sa_y}\left(\frac{\tilde{L}_y}{2}-\frac{b_y}{2a_y}\right)\right)-\text{erf}\left(\sqrt{jk_sa_y}\left(-\frac{\tilde{L}_y}{2}-\frac{b_y}{2a_y}\right)\right)\right]. \tag{13}$$

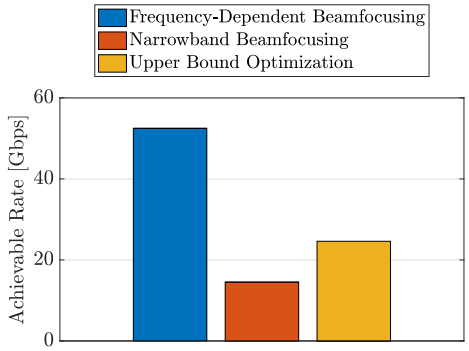

Fig. 3: Achievable rate for $N_x = N_y = 80$, $B = 20$ GHz, $f_c = 300$ GHz, $S = 20$, $(r_t, \theta_t, \phi_t) = (1, \pi/3, \pi/5)$, and $(r_r, \theta_r, \phi_r) = (5, \pi/4, \pi/3)$.

find the reflection coefficient vector $\mathbf{b}$ that maximimizes the achievable rate, i.e.,

$$\begin{aligned}\max_{\mathbf{b}} \quad & R(\mathbf{b}) = \textstyle\sum_{s=0}^{S-1}\frac{B}{S}\log_2\left(1+\frac{P_t\text{PL}(f_s)|\mathbf{h}_s^T\mathbf{b}|^2}{B\sigma^2}\right)\\ \text{s.t.} \quad & |[\mathbf{b}]_n| = 1, \forall n = 1,\ldots,N.\end{aligned} \tag{19}$$

The beamfocusing optimization problem (19) resembles the wideband design problem in IRS-aided OFDM systems, which is non-convex and difficult to solve [13]. In the spirit of [13], we turn to maximize the upper bound[1] of $R(\mathbf{b})$:

$$R(\mathbf{b}) \le B\log_2\left(1+\frac{P_t\text{PL}(f_s)}{B\sigma^2}\frac{\sum_{s=0}^{S-1}|\mathbf{h}_s^T\mathbf{b}|^2}{S}\right). \tag{20}$$

We therefore formulate the optimization problem

$$\max_{\mathbf{b}} \quad \sum_{s=0}^{S-1}|\mathbf{h}_s^T\mathbf{b}|^2 = \|\mathbf{H}^T\mathbf{b}\|^2 = \mathbf{b}^H\mathbf{H}^*\mathbf{H}^T\mathbf{b}, \tag{21}$$

where $\mathbf{H} = [\mathbf{h}_0,\ldots,\mathbf{h}_{S-1}] \in \mathbb{C}^{N\times S}$. The above quadratic form has the solution $\mathbf{b}^\star = \sqrt{N}\mathbf{u}$, where $\mathbf{u}$ is the unit-norm eigenvector corresponding to the maximum eigenvalue of the Hermitian matrix $\mathbf{H}^*\mathbf{H}^T$. Since the elements of $\mathbf{b}^\star$ do not satisfy the unit-modulus constraint, this solution is referred to as *upper bound optimization*; recall that $\mathbf{b}^\star$ would be implemented by controlling the amplitude and phase of each reflection coefficient, which is not feasible in the passive IRS architecture under consideration. As a result, the upper bound optimization serves as a benchmark to assess the impact of the spatial-wideband effect on the achievable rate. In Fig. 3, the achievable rates of the frequency-dependent beamfocusing, narrowband beamfocusing, and upper bound optimization approach are 52.48 Gbps, 14.52 Gbps, and 24.61 Gbps, respectively. Narrowband beamfocusing performs very poor, and results in a 72.3% rate loss. Moreover, the upper bound optimization approach performs better, yet yields a much smaller rate than frequency-dependent beamfocusing. This numerical experiment showcases the need of a frequency-dependent IRS design [15].

[1]This optimization approach is well-established in the related literature; see [14] and references therein.

C. Energy Efficiency

1) MIMO System: Consider a multiple-input multiple-output (MIMO) system, where the Tx and Rx have N_t and N_r antennans, respectively. For efficient hardware implementation, hybrid analog-digital array architectures are assumed at both ends. The frequency-dependent path loss of the direct channel, i.e., line-of-sight (LoS), is given by [5]

$$\text{PL}_{\text{MIMO}}(f) = \frac{G_tG_rc^2}{(4\pi r_d(f_c+f))^2}e^{-\kappa_{\text{abs}}(f)r_d}, \tag{22}$$

where $r_d = \|\mathbf{p}_t - \mathbf{p}_r\|$. Next, we assume that N_t and N_r are adequately small so that the spatial-wideband effect is negligible; this can be attained by a uniform planar array (UPA), such as an 10×10-element UPA [5]. In the far-field, the LoS channel matrix is rank-one [16, Ch. 7]. Then, frequency-flat beamforming and combining yield the received SNR

$$\text{SNR}_s^{\text{MIMO}} = \frac{N_tN_rP_t\text{PL}_{\text{MIMO}}(f_s)}{B\sigma^2}. \tag{23}$$

The respective power consumption is calculated as[2]

$$P_{\text{MIMO}} = P_t + N_r(P_{\text{PS}}+P_{\text{PA}}) + N_t(P_{\text{PS}}+P_{\text{PA}}), \tag{24}$$

where P_{PS} and P_{PA} are the power consumption values for a phase shifter and a power amplifier, which are 42 mW and 60 mW at $f_c = 300$ GHz, respectively [3].

2) IRS-Aided MIMO System: The Tx and Rx perform beamforming and combining to communicate a single stream via the IRS of N elements. Due to the directional transmissions, the Tx-Rx link is very weak, and thus is neglected. In this case, the receive SNR at the sth subcarrier is

$$\text{SNR}_s = \frac{N_tN_rN^2G_sP_t\text{PL}(f_s)}{B\sigma^2}. \tag{25}$$

Using varactor diodes, the power expenditure of an IRS element is nearly negligible [12]. For the sake of exposition, we assume that the power consumption of the IRS-aided system is also given by (24). Thus, the EE is given

[2]The power consumption of signal processing is neglected.

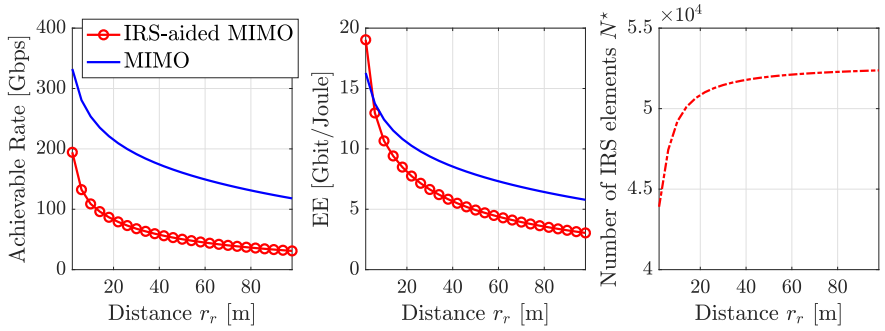

Fig. 4: Results for $\alpha = 2$, narrowband beamfocusing, and a fixed IRS location at (0,0,0). In the MIMO system, $N_t = 100$ and $N_r = 100$. The other parameters are $G_t = G_r = 20$ dBi, $P_t = 10$ dBm, $\sigma^2 = -174$ dBm/Hz, $B = 20$ GHz, $S = 20$, $f_c = 300$ GHz, $L_x = L_y = \lambda/2$, $\mathbf{p}_t = (x_t, y_t, z_t) = (0.8, -0.8, 0.2)$, and $\mathbf{p}_r = (x_r, y_r, z_r) = (0.8, r_r, 0.2)$.

by $\sum_{s=0}^{S-1} \frac{B}{S} \log_2(1 + \text{SNR}_s)/P_{\text{MIMO}}$. As in [6], we can now decrease the number of antennas as N_t/α and N_r/α, whilst increasing the number of IRS elements as $N^\star = \alpha \frac{\lambda}{L_x L_y} \frac{r_t r_r}{\sqrt{F(\theta_t,\phi_r,\theta_r) r_d}} e^{-\frac{1}{2}\kappa_{\text{abs}}(f)(r_d - r_r - r_t)}$, to attain an EE gain α compared to the pure MIMO system. The achievable rate, EE, and $N^\star$ are plotted versus r_r in Fig. 4. In contrast to the spatially narrowband case, IRS-aided MIMO cannot outperform MIMO due to the spatial-wideband effect present in the former architecture.

ACKNOWLEDGEMENTS

This project has received funding from the European Research Council (ERC) under the European Union's Horizon 2020 research and innovation programme (grant agreement No. 101001331).

IV. CONCLUSIONS

We have studied, for the first time, the spatial-wideband effect in IRS-aided THz communications. Specifically, we introduced a near-field channel model that captures the peculiarities of wideband transmissions. Capitalizing on the proposed channel model, we next analyzed the power gain and asymptotic achievable rate under narrowband beamfocusing. Our analysis shows that frequency-dependent beamfocusing is vital for the successful deployment of future IRS-assisted wideband THz systems.

APPENDIX

We have that

$$\frac{\sum_{n=-\frac{N_x}{2}}^{\frac{N_x}{2}-1} \sum_{m=-\frac{N_y}{2}}^{\frac{N_y}{2}-1} e^{-j2\pi f_s \frac{\tilde{r}_t(n,m)+\tilde{r}_r(n,m)}{c}} L_x L_y}{(N_x L_x)(N_y L_y)} \approx \frac{\int_{-\frac{\tilde{L}_x}{2}}^{\frac{\tilde{L}_x}{2}} \int_{-\frac{\tilde{L}_y}{2}}^{\frac{\tilde{L}_y}{2}} e^{-j2\pi f_s \frac{\tilde{r}_t(n,m)+\tilde{r}_r(n,m)}{c}} dx dy}{\tilde{L}_x \tilde{L}_y}, \quad (26)$$

where $\tilde{L}_x = N_x L_x$, $\tilde{L}_y = N_y L_y$, $dx = L_x$, and $dy = L_y$. Now setting $(n - 1/2)L_x = x$ and $(m - 1/2)L_y = y$ in $\tilde{r}_t(n,m)$ and $\tilde{r}_t(n,m)$, and leveraging the identity

$$\int e^{-jk(ax^2 - bx)} dx = \frac{\sqrt{\pi}}{2\sqrt{jka}} \text{erf}\left(\sqrt{jka}\left(x - \frac{b}{2a}\right)\right) \quad (27)$$

gives the desired result after basic algebra.

REFERENCES

[1] T. S. Rappaport *et al.*, "Wireless communications and applications above 100 GHz: Opportunities and challenges for 6G and beyond," *IEEE Access*, vol. 7, pp. 78729-78757, 2019.

[2] J. Zhang *et al.*, "Prospective multiple antenna technologies for beyond 5G," *IEEE J. Sel. Areas Commun.*, vol. 38, no. 8, pp. 1637–1660, Aug. 2020.

[3] L. Yan, C. Han, and J. Yuan, "A dynamic array-of-subarrays architecture and hybrid precoding algorithms for terahertz wireless communications," *IEEE J. Sel. Areas Commun.*, vol. 38, no. 9, pp. 2041-2056, Sept. 2020.

[4] M. A. Elmossallamy *et al.*, "Reconfigurable intelligent surfaces for wireless communications: Principles, challenges, and opportunities," *IEEE Trans. Cognitive Commun. Netw.*, vol. 6, no. 3, pp. 990-1002, Sep. 2020.

[5] K. Dovelos, M. Matthaiou, H. Q. Ngo, and B. Bellalta, "Channel estimation and hybrid combining for wideband terahertz massive MIMO systems," *IEEE J. Sel. Areas Commun.*, Apr. 2021.

[6] K. Dovelos, S. D. Assimonis, H. Q. Ngo, B. Bellalta, and M. Matthaiou, "Intelligent reflecting surfaces at terahertz bands: Channel modeling and analysis," to appear in *Proc. IEEE ICC*, 2021.

[7] Z. Wan, Z. Gao, M. Di Renzo, and M.-S. Alouini, "Terahertz massive MIMO with holographic reconfigurable intelligent surfaces," *IEEE Trans. Commun.*, Mar. 2021.

[8] B. Ning *et al*, "Terahertz multi-user massive MIMO with intelligent reflecting surface: Beam training and hybrid beamforming," *IEEE Trans. Veh. Technol.*, vol. 70, no. 2, pp. 1376-1393, Feb. 2021.

[9] A.-A. A. Boulogeorgos and A. Alexiou, "Coverage analysis of reconfigurable intelligent surface assisted THz wireless systems," *IEEE Open J. Veh. Technol.*, vol. 2, pp. 94-110, Jan. 2021.

[10] Ö. Özdogan, E. Björnson, and E. G. Larsson, "Intelligent reflecting surfaces: Physics, propagation, and pathloss modeling," *IEEE Wireless Commun. Lett.*, vol. 9, no. 5, pp. 581-585, May 2020.

[11] M. Najafi, V. Jamali, R. Schober, and H. V. Poor, "Physics-based modeling and scalable optimization of large intelligent reflecting surfaces," *IEEE Trans. Commun.*, vol. 69, no. 4, pp. 2673-2691, Apr. 2021.

[12] W. Tang *et al.*, "Wireless communications with reconfigurable intelligent surface: Path loss modeling and experimental measurement," *IEEE Trans. Wireless Commun.*, vol. 20, no. 1, pp. 421-439, Jan. 2021.

[13] S. Lin *et al.*, "Adaptive transmission for reconfigurable intelligent surface-assisted OFDM wireless communications," *IEEE J. Sel. Areas Commun.*, vol. 38, no. 11, pp. 2653-2665, Nov. 2020.

[14] Y. Chen *et al.*, "Hybrid precoding for wideband millimeter wave MIMO systems in the face of beam squint," *IEEE Trans. Wireless Commun.*, vol. 20, no. 3, pp. 1847-1860, Mar. 2021.

[15] S. M. A. Momeni Hasan Abadi *et al.*, "Ultra-wideband, true-time-delay reflectarray antennas using ground-plane-backed, miniaturized-element frequency selective surfaces," *IEEE Trans. Antennas Propag.*, vol. 63, no. 2, pp. 534-542, Feb. 2015.

[16] D. Tse and P. Viswanath, *Fundamentals of Wireless Communication*. New York, NY, USA: Cambridge Univ. Press, 2005.

Appendix

Proposed Wideband Combiner in the Near-Field

Under a spherical wavefront, the array response vector (2.2) is recast as

$$\mathbf{a}(\phi,\theta,D,f)=\mathrm{vec}(\mathbf{A}(\phi,\theta,D,f)), \tag{4.1}$$

where D is the distance between the user and the BS, whilst $\mathbf{A}(\phi,\theta,D,f)\in\mathbb{C}^{M\times N}$ is the so-called array response matrix of the BS. The (m,n)th element of $\mathbf{A}$ is calculated as [78]

$$[\mathbf{A}(\phi,\theta,D,f)]_{m,n}=e^{-j2\pi(f_c+f)\frac{D_{mn}}{c}}, \tag{4.2}$$

where

$$D_{mn}\triangleq\Big((D\cos\phi\sin\theta-nd)^2+(D\sin\phi\sin\theta-md)^2+(D\cos\theta)^2\Big)^{1/2} \tag{4.3}$$

is the distance between the user located at $(D\cos\phi\sin\theta, D\sin\phi\sin\theta, D\cos\theta)$ and the (m,n)th BS antenna. Availing of the Fresnel approximation

$$\begin{aligned}D_{mn}\approx D&+\frac{(nd)^2(1-\cos^2\phi\sin^2\theta)}{2D}-nd\cos\phi\sin\theta\\&+\frac{(md)^2(1-\sin^2\phi\sin^2\theta)}{2D}-md\sin\phi\sin\theta,\end{aligned} \tag{4.4}$$

the proposed combiner in Proposition 1 from **paper I** is extended to the spherical wavefront case as

$$\mathbf{f}_{\mathrm{RF}}[s]=\frac{1}{\sqrt{N_B}}\mathrm{vec}\left(\mathbf{A}(\phi,\theta,D,0)\odot\mathbf{T}[s]\right), \tag{4.5}$$

where $\mathbf{T}[s]=\left[e^{-j2\pi f_s\frac{\Delta_{mn}(\phi,\theta,D)}{c}}\right]_{m=0,n=-0}^{M_{\mathrm{sb}}-1,N_{\mathrm{sb}}-1}\otimes\mathbf{1}_{\tilde{M}\times\tilde{N}}$ and

$$\begin{aligned}\Delta_{mn}(\phi,\theta,D)=&\frac{(n\tilde{N}d)^2(1-\cos^2\phi\sin^2\theta)}{2D}+\frac{(m\tilde{M}d)^2(1-\sin^2\phi\sin^2\theta)}{2D}\\&-n\tilde{N}d\cos\phi\sin\theta-m\tilde{M}d\sin\phi\sin\theta.\end{aligned} \tag{4.6}$$

Note that $\Delta_{mn}(\phi,\theta,D)/c$ is the delay to be mitigated between consecutive virtual subarrays, M_{sb} and N_{sb} are the number of subarrays in the vertical and horizontal directions, respectively, whereas $\tilde{M}=M/M_{\mathrm{sb}}$ and $\tilde{N}=N/N_{\mathrm{sb}}$ are the number of antennas per virtual subarray.

Bibliography

[1] M. Agiwal, A. Roy, and N. Saxena, "Next generation 5G wireless networks: A comprehensive survey," *IEEE Communications Surveys & Tutorials*, vol. 18, no. 3, pp. 1617-1655, third quarter 2016.

[2] A. N. Uwaechia and N. M. Mahyuddin, "A comprehensive survey on millimeter wave communications for fifth-generation wireless networks: Feasibility and challenges," *IEEE Access*, vol. 8, pp. 62367-62414, 2020.

[3] T. S. Rappaport *et al.*, "Wireless communications and applications above 100 GHz: Opportunities and challenges for 6G and beyond," *IEEE Access*, vol. 7, pp. 78729-78757, 2019.

[4] I. F. Akyildiz, J. M. Jornet, and C. Han, "TeraNets: Ultra-broadband communication networks in the terahertz band," *IEEE Wireless Communications*, vol. 21, no. 4, pp. 130-135, August 2014.

[5] Z. Chen *et al.*, "A survey on terahertz communications," *China Communications*, vol. 16, no. 2, pp. 1-35, February 2019.

[6] J. Zhang *et al.*, "Prospective multiple antenna technologies for beyond 5G," *IEEE Journal on Selected Areas in Communications*, vol. 38, no. 8, pp. 1637-1660, August 2020.

[7] M. Matthaiou, O. Yurduseven, H. Q. Ngo, D. Morales-Jimenez, S. L. Cotton, and V. F. Fusco, "The road to 6G: Ten physical layer challenges for communications engineers," *IEEE Communications Magazine*, vol. 59, no. 1, pp. 64-69, January 2021.

[8] E. G. Larsson, O. Edfors, F. Tufvesson, and T. L. Marzetta, "Massive MIMO for next generation wireless systems," *IEEE Communications Magazine*, vol. 52, no. 2, pp. 186-195, February 2014.

[9] T. L. Marzetta, "Massive MIMO: An introduction," *Bell Labs Technical Journal*, vol. 20, pp. 11-22, March 2015.

[10] I. F. Akyildiz, C. Han, and S. Nie, "Combating the distance problem in the millimeter wave and terahertz frequency bands," *IEEE Communications Magazine*, vol. 56, no. 6, pp. 102-108, June 2018.

[11] J. A. Zhang, X. Huang, V. Dyadyuk, and Y. J. Guo, "Massive hybrid antenna array for millimeter-wave cellular communications," *IEEE Wireless Communications*, vol. 22, no. 1, pp. 79-87, February 2015.

[12] B. Wang *et al.*, "Spatial-wideband effect in massive MIMO with application in mmWave systems," *IEEE Communications Magazine*, vol. 56, no. 12, pp. 134-141, December 2018.

[13] C. Lin and G. Y. L. Li, "Terahertz communications: An array-of-subarrays solution," *IEEE Communications Magazine*, vol. 54, no. 12, pp. 124-131, December 2016.

[14] E. Basar, M. Di Renzo, J. De Rosny, M. Debbah, M.-S. Alouini, and R. Zhang, "Wireless communications through reconfigurable intelligent surfaces," *IEEE Access*, vol. 7, pp. 116753-116773, 2019.

[15] M. Di Renzo *et al.*, "Smart radio environments empowered by reconfigurable intelligent surfaces: How it works, state of research, and the road ahead," *IEEE Journal on Selected Areas in Communications*, vol. 38, no. 11, pp. 2450-2525, November 2020.

[16] C. Huang, A. Zappone, G. C. Alexandropoulos, M. Debbah, and C. Yuen, "Reconfigurable intelligent surfaces for energy efficiency in wireless communication," *IEEE Transactions on Wireless Communications*, vol. 18, no. 8, pp. 4157-4170, August 2019.

[17] A. Khaleel and E. Basar, "Reconfigurable intelligent surface-empowered MIMO systems," *IEEE Systems Journal*, August 2020.

[18] S. Zhang and R. Zhang, "Capacity characterization for intelligent reflecting surface aided MIMO communication," *IEEE Journal on Selected Areas in Communications*, vol. 38, no. 8, pp. 1823-1838, August 2020.

[19] C. Han and Y. Chen, "Propagation modeling for wireless communications in the terahertz band," *IEEE Communications Magazine*, vol. 56, no. 6, pp. 96-101, June 2018.

[20] A. Faisal, H. Sarieddeen, H. Dahrouj, T. Y. Al-Naffouri, and M.-S. Alouini, "Ultramassive MIMO systems at terahertz bands: Prospects and challenges," *IEEE Vehicular Technology Magazine*, vol. 15, no. 4, pp. 33-42, December 2020.

[21] R. W. Heath, N. González-Prelcic, S. Rangan, W. Roh, and A. M. Sayeed, "An overview of signal processing techniques for millimeter wave MIMO systems," *IEEE Journal of Selected Topics in Signal Processing*, vol. 10, no. 3, pp. 436-453, April 2016.

[22] B. Wang, F. Gao, S. Jin, H. Lin, and G. Y. Li, "Spatial- and frequency-wideband effects in millimeter-wave massive MIMO systems," *IEEE Transactions on Signal Processing*, vol. 66, no. 13, pp. 3393-3406, July, 2018.

[23] C. Lin and G. Y. Li, "Indoor terahertz communications: How many antenna arrays are needed?," *IEEE Transactions on Wireless Communications*, vol. 14, no. 6, pp. 3097-3107, June 2015.

[24] H. Sarieddeen, M.-S. Alouini, and T. Y. Al-Naffouri, "Terahertz-band ultra-massive spatial modulation MIMO," *IEEE Journal on Selected Areas in Communications*, vol. 37, no. 9, pp. 2040-2052, September 2019.

[25] Q. Sultan, M. S. Khan, and Y. S. Cho, "Fast 3D beamforming technique for millimeter-wave cellular systems with uniform planar arrays," *IEEE Access*, vol. 8, pp. 123469-123482, 2020.

[26] C. Lin, G. Y. Li, and L. Wang, "Subarray-based coordinated beamforming training for mmWave and sub-THz communications," *IEEE Journal on Selected Areas in Communications*, vol. 35, no. 9, pp. 2115-2126, September 2017.

[27] B. Wang, X. Li, F. Gao, and G. Y. Li, "Power leakage elimination for wideband mmWave massive MIMO-OFDM systems: An energy-focusing window approach," *IEEE Transactions on Signal Processing*, vol. 67, no. 21, pp. 5479-5494, November 2019.

[28] I. F. Akyildiz and J. M. Jornet, "Realizing ultra-massive MIMO (1024×1024) communication in the (0.06-10) terahertz band," *Nano Communication Networks*, vol. 8, pp. 46–54, June 2016.

[29] H. Hashemi, T. Chu, and J. Roderick, "Integrated true-time-delay-based ultra-wideband array processing," *IEEE Communications Magazine*, vol. 46, no. 9, pp. 162-172, September 2008.

[30] J. P. González-Coma, W. Utschick, and L. Castedo, "Hybrid LISA for wideband multiuser millimeter-wave communication systems under beam squint," *IEEE Transactions on Wireless Communications*, vol. 18, no. 2, pp. 1277-1288, February 2019.

[31] S. Park, A. Alkhateeb, and R. W. Heath, "Dynamic subarrays for hybrid precoding in wideband mmWave MIMO systems," *IEEE Transactions on Wireless Communications*, vol. 16, no. 5, pp. 2907-2920, May 2017.

[32] L. Kong, S. Han, and C. Yang, "Hybrid precoding with rate and coverage constraints for wideband massive MIMO systems," *IEEE Transactions on Wireless Communications*, vol. 17, no. 7, pp. 4634-4647, July 2018.

[33] X. Liu and D. Qiao, "Space-time block coding-based beamforming for beam squint compensation," *IEEE Wireless Communications Letters*, vol. 8, no. 1, pp. 241-244, February 2019.

[34] J. Tan and L. Dai, "Delay-phase precoding for THz massive MIMO with beam split," in *Proc. IEEE Global Communications Conference*, 2019, pp. 1-6.

[35] W. U. Bajwa, J. Haupt, A. M. Sayeed, and R. Nowak, "Compressed channel sensing: A new approach to estimating sparse multipath channels," *Proceedings of the IEEE*, vol. 98, no. 6, pp. 1058-1076, June 2010.

[36] R. Méndez-Rial, C. Rusu, N. González-Prelcic, A. Alkhateeb, and R. W. Heath, "Hybrid MIMO architectures for millimeter wave communications: Phase shifters or switches?," *IEEE Access*, vol. 4, pp. 247-267, 2016.

[37] T. T. Cai and L. Wang, "Orthogonal matching pursuit for sparse signal recovery with noise," *IEEE Transactions on Information Theory*, vol. 57, no. 7, pp. 4680-4688, July 2011.

[38] L. Harry and V. Trees, *Optimum Array Processing: Detection, Estimation, and Modulation Theory*. Hoboken, NJ, USA: Wiley, 2002.

[39] Z. Gao, L. Dai, Z. Wang, and S. Chen, "Spatially common sparsity based adaptive channel estimation and feedback for FDD massive MIMO," *IEEE Transactions on Signal Processing*, vol. 63, no. 23, pp. 6169-6183, December 2015.

[40] J. A. Tropp, A. C. Gilbert, and M. J. Strauss, "Algorithms for simultaneous sparse approximation—part I: Greedy pursuit," *Signal Processing*, vol. 86, no. 3, pp. 572–588, 2006.

[41] J. Lee, G. Gil, and Y. H. Lee, "Exploiting spatial sparsity for estimating channels of hybrid MIMO systems in millimeter wave communications," in *Proc. IEEE Global Communications Conference*, 2014, pp. 3326-3331.

[42] Y. You, L. Zhang, and M. Liu, "IP aided OMP based channel estimation for millimeter wave massive MIMO communication," in *Proc. IEEE Wireless Communications and Networking Conference*, 2019, pp. 1-6.

[43] C. A. Balanis, *Antenna Theory: Analysis and Design*. John Wiley & Sons, 2012.

[44] S. W. Ellingson, "Path loss in reconfigurable intelligent surface-enabled channels," *arXiv preprint* arXiv:1912.06759, 2019.

[45] W. Tang *et al.*, "Wireless communications with reconfigurable intelligent surface: Path loss modeling and experimental measurement," *IEEE Transactions on Wireless Communications*, vol. 20, no. 1, pp. 421-439, January 2021.

[46] W. Tang *et al.*, "Path loss modeling and measurements for reconfigurable intelligent surfaces in the millimeter-wave frequency band," *arXiv preprint* arXiv:2101.08607, 2021.

[47] A. Z. Elsherbeni, F. Yang, and P. Nayeri, *Reflectarray Antennas:Theory, Designs, and Applications*. John Wiley & Sons, 2018.

[48] M. Di Renzo *et al.*, "Reconfigurable intelligent surfaces vs. relaying: Differences, similarities, and performance comparison," *IEEE Open Journal of the Communications Society*, vol. 1, pp. 798-807, June 2020.

[49] C. Han, A. O. Bicen, and I. F. Akyildiz, "Multi-ray channel modeling and wideband characterization for wireless communications in the terahertz nand," *IEEE Transactions on Wireless Communications*, vol. 14, no. 5, pp. 2402-2412, May 2015.

[50] C. Han and I. F. Akyildiz, "Three-dimensional end-to-end modeling and analysis for graphene-enabled terahertz band communications," *IEEE Transactions on Vehicular Technology*, vol. 66, no. 7, pp. 5626-5634, July 2017.

[51] Q. Wu and R. Zhang, "Intelligent reflecting surface enhanced wireless network via joint active and passive beamforming," *IEEE Transactions on Wireless Communications*, vol. 18, no. 11, pp. 5394-5409, November 2019.

[52] O. Yurduseven, S. D. Assimonis, and M. Matthaiou, "Intelligent reflecting surfaces with spatial modulation: An electromagnetic perspective," *IEEE Open Journal of the Communications Society*, vol. 1, pp. 1256-1266, August 2020.

[53] Q. Wu, S. Zhang, B. Zheng, C. You, and R. Zhang, "Intelligent reflecting surface-aided wireless communications: A tutorial," *IEEE Transactions on Communications*, vol. 69, no. 5, pp. 3313-3351, May 2021.

[54] P. Nepa and A. Buffi, "Near-field-focused microwave antennas: Near-field shaping and implementation," *IEEE Antennas and Propagation Magazine*, vol. 59, no. 3, pp. 42-53, June 2017.

[55] D. Tse and P. Viswanath, *Fundamentals of Wireless Communication*. New York, NY, USA: Cambridge Univ. Press, 2005.

[56] L. Yan, C. Han, and J. Yuan, "A dynamic array-of-subarrays architecture and hybrid precoding algorithms for terahertz wireless communications," *IEEE Journal on Selected Areas in Communications*, vol. 38, no. 9, pp. 2041-2056, September 2020.

[57] S.-K. Chou, O. Yurduseven, H. Q. Ngo, and M. Matthaiou, "On the aperture efficiency of intelligent reflecting surfaces," *IEEE Wireless Communications Letters*, vol. 10, no. 3, pp. 599-603, March 2021.

[58] C. Huang *et al.*, "Holographic MIMO surfaces for 6G wireless networks: Opportunities, challenges, and trends," *IEEE Wireless Communications*, vol. 27, no. 5, pp. 118-125, October 2020.

[59] A. Pizzo, T. L. Marzetta, and L. Sanguinetti, "Spatially-stationary model for holographic MIMO small-scale fading," *IEEE Journal on Selected Areas in Communications*, vol. 38, no. 9, pp. 1964-1979, September 2020.

[60] E. Björnson, L. Sanguinetti, H. Wymeersch, J. Hoydis, and T. L. Marzetta, "Massive MIMO is a reality − What is next? Five promising research directions for antenna arrays," *Digital Signal Processing*, vol. 94, no. 3, pp. 3–20, November 2019.

[61] C. A. Balanis, *Advanced Engineering Electromagnetics (2nd ed.)*. John Wiley & Sons, 2012.

[62] W. C. Gibson, *The Method of Moments in Electromagnetics (2nd ed.)*. Chapman & Hall/CRC, 2014.

[63] J. Xu and Y. Lin, "A novel channel model for reconfigurable intelligent surface-assisted wireless networks," in *Proc. IEEE Global Communications Conference*, 2020, pp. 01-06.

[64] Ö. Özdogan, E. Björnson, and E. G. Larsson, "Intelligent reflecting surfaces: Physics, propagation, and pathloss modeling," *IEEE Wireless Communications Letters*, vol. 9, no. 5, pp. 581-585, May 2020.

[65] M. Najafi, V. Jamali, R. Schober, and H. V. Poor, "Physics-based modeling and scalable optimization of large intelligent reflecting surfaces," *IEEE Transactions on Communications*, vol. 69, no. 4, pp. 2673-2691, April 2021.

[66] M. A. ElMossallamy, H. Zhang, L. Song, K. G. Seddik, Z. Han, and G. Y. Li, "Reconfigurable intelligent surfaces for wireless communications: Principles, challenges, and opportunities," *IEEE Transactions on Cognitive Communications and Networking*, vol. 6, no. 3, pp. 990-1002, September 2020.

[67] M. Di Renzo, F. Habibi Danufane, X. Xi, J. de Rosny, and S. Tretyakov, "Analytical modeling of the path-loss for reconfigurable intelligent surfaces – Anomalous mirror or scatterer ?" in *Proc.* IEEE 21st International Workshop on Signal Processing Advances in Wireless Communications, 2020, pp. 1-5.

[68] J. C. B. Garcia, A. Sibille, and M. Kamoun, "Reconfigurable intelligent surfaces: Bridging the gap between scattering and reflection," *IEEE Journal on Selected Areas in Communications*, vol. 38, no. 11, pp. 2538-2547, November 2020.

[69] E. Björnson and L. Sanguinetti, "Power scaling laws and near-field behaviors of massive MIMO and intelligent reflecting surfaces," *IEEE Open Journal of the Communications Society*, vol. 1, pp. 1306-1324, 2020.

[70] R. J. Williams, E. de Carvalho, and T. L. Marzetta, "A communication model for large intelligent surfaces," in *Proc. IEEE International Conference on Communications*, 2020, pp. 1-6.

[71] Z. Wan, Z. Gao, F. Gao, M. Di Renzo, and M.-S. Alouini, "Terahertz massive MIMO with holographic reconfigurable intelligent surfaces," *IEEE Transactions on Communications*, March, 2021 (Early Access).

[72] B. Ning, Z. Chen, W. Chen, Y. Du, and J. Fang, "Terahertz multi-user massive MIMO with intelligent reflecting surface: Beam training and hybrid beamforming," *IEEE Transactions on Vehicular Technology*, vol. 70, no. 2, pp. 1376-1393, February 2021.

[73] A.-A. A. Boulogeorgos and A. Alexiou, "Coverage analysis of reconfigurable intelligent surface assisted THz wireless systems," *IEEE Open Journal of Vehicular Technology*, vol. 2, pp. 94-110, 2021.

[74] S. Abeywickrama *el al.*, "Intelligent reflecting surface: Practical phase shift model and beamforming optimization," *IEEE Transactions on Communications*, vol. 68, no. 9, pp. 5849-5863, September2020.

[75] S. Lin, B. Zheng, G. C. Alexandropoulos, M. Wen, F. Chen, and S. Mumtaz, "Adaptive transmission for reconfigurable intelligent surface-assisted OFDM wireless communications," *IEEE Journal on Selected Areas in Communications*, vol. 38, no. 11, pp. 2653-2665, November 2020.

[76] Y. Chen, Y. Xiong, D. Chen, T. Jiang, S. X. Ng, and L. Hanzo, "Hybrid precoding for wideBand millimeter wave MIMO systems in the face of beam squint," *IEEE Transactions on Wireless Communications*, vol. 20, no. 3, pp. 1847-1860, March 2021.

[77] S. M. A. Momeni Hasan Abadi, K. Ghaemi, and N. Behdad, "Ultrawideband, true-time-delay reflectarray antennas using ground-plane-backed, miniaturized-element frequency selective surfaces," *IEEE Transactions on Antennas and Propagation*, vol. 63, no. 2, pp. 534-542, February 2015.

[78] F. Guidi and D. Dardari, "Radio positioning with EM processing of the spherical wavefront," *IEEE Transactions on Wireless Communications*, vol. 20, no. 6, pp. 3571-3586, June 2021.